Multifunctional Metasurfaces for Angular-Robust Operation and Electrochemistry

Luca Maria Berger

München 2023

i

Multifunctional Metasurfaces for Angular-Robust Operation and Electrochemistry

Dissertation

to obtain the doctoral degree of natural sciences (Dr. rer. nat.)

at the Faculty of Physics

of the Ludwig-Maximilians-Universität München

submitted by

Luca Maria Berger

from Milan

München, 04/10/2023

First referee: Prof. Dr. Stefan A. Maier

Second referee: Prof. Dr. Joachim Rädler

Date of the oral examination: 13/12/2023

Multifunctional Metasurfaces for Angular-Robust Operation and Electrochemistry

Dissertation

zur Erlangung des Doktorgrades der Naturwissenschaften (Dr. rer. nat.)

an der Fakultät für Physik

der Ludwig-Maximilians-Universität München

vorgelegt von

Luca Maria Berger

aus Mailand

München, 04/10/2023

Erstgutachter: Prof. Dr. Stefan A. Maier

Zweitgutachter: Prof. Dr. Joachim Rädler

Datum der mündlichen Prüfung: 13/12/2023

Publications that Form Part of this Dissertation

- Berger, L. M., Barkey, M., Maier, S. A., Tittl, A., Metallic and All-Dielectric Metasurfaces Sustaining Displacement-Mediated Bound States in the Continuum. *Adv. Optical Mater.* 2023, 2301269.

- Berger, L. M., Duportal, M., Menezes, L. de S., Cortés, E., Maier, S. A., Tittl, A., Krischer, K., Improved In Situ Characterization of Electrochemical Interfaces Using Metasurface-Driven Surface-Enhanced IR Absorption Spectroscopy. *Adv. Funct. Mater.* 2023, 33, 2300411.

- Duportal, M., Berger, L. M., Maier, S. A., Tittl, A., & Krischer, K., Multi-band metasurface-driven surface-enhanced infrared absorption spectroscopy for improved characterization of in-situ electrochemical reactions. *arXiv preprint arXiv:2307.10951*, 2023. (currently under peer-review)

Contents

List of Figures

List of Tables

List of Abbreviations

EM	Electromagnetic
SEM	Scanning electron microscopy
Vis	Visible
RF	Radiofrequency
IR	Infrared
NIR	Near-infrared
Mid-IR	Mid-infrared
SEIRAS	Surface-enhanced IR absorption spectroscopy
ATR	Attenuated total internal reflection
FTIR	Fourier-transform IR
FEM	Finite element method
BIC	Bound state in the continuum
q-BIC	Quasi-bound state in the continuum
FOM	Figure of merit
TCMT	Temporal coupled-mode theory
HER	Hydrogen evolution reaction
CO_2RR	Carbon dioxide reduction reaction
CO_{linear}	CO adsorbed in top site configurations
CO_{bridge}	CO adsorbed in bridge site configurations
Q	Quality
RA	Rayleigh-Wood anomaly mode
Redox	Reduction-oxidation
TE	Transverse electric
TM	Transverse magnetic
PMMA	Poly(methyl methacrylate)
e-beam	Electron beam
PECVD	Plasma-enhanced chemical vapor deposition
ICP-RIE	Inductively-coupled plasma reactive ion etching
QCL	Quantum cascade laser
QCL-IR	Mid-IR quantum cascade laser
CV	Cyclic voltammetry
OCP	Open circuit potential
a-Si	Amorphous silicon
Ar^{sat}	Argon-saturated
CO^{sat}	CO-saturated
NA	Numerical aperture

Zusammenfassung

Die Nanophotonik hat sich als treibende Kraft von Technologie und Innovation durchgesetzt. Indem sie disziplinäre Lücken überbrückt und sich nahtlos in andere wissenschaftliche Bereiche integriert, hat die Nanophotonik signifikante Durchbrüche in der Informationstechnologie, Medizin und Gesundheitswesen, Elektronik, Lebenswissenschaften, Energie, Umweltwissenschaften und Sicherheit, sowie in anderen Bereichen, vorangetrieben. Bahnbrechende Entdeckungen werden auch in Zukunft an der Schnittstelle zwischen der Nanophotonik und anderen wissenschaftlichen Gebieten oder Anwedungen entstehen. In dieser Arbeit werden Licht-Materie-Wechselwirkungen an der Schnittstelle zur Elektrochemie und in Richtung fortgeschrittener Sensorsysteme untersucht.

Im ersten Teil dieser Arbeit untersuchen wir nanophotonische Metaoberflächen auf der Grundlage gebundener Zustände im Kontinuum (BICs, *englisch: Bound states in the continuum*). BICs sind lokalisierte elektromagnetische Moden innerhalb des kontinuierlichen Spektrums. Aufgrund ihrer unendlichen Lebensdauer ohne Strahlungsverluste treiben BICs Forschungsrichtungen bei Lasern, nichtlinearen optischen Prozessen und Sensoren voran. Konventionelle Methoden zur Umwandlung von BICs in quasi-BICs, also Resonanzen mit hohen aber begrentzten Gütefaktoren (Q Faktoren, *englisch: quality factor*), basieren in der Regel auf der Brechnung der Inversionsymmetrie von Metaoberflächen. Diese führen allerdings oft zu Resonanzen, die stark vom Einfallswinkel des Lichts abhängen, was sie für viele praktische Anwendungen ungeeignet macht. In dieser Arbeit wird eine aufstrebende Klasse von BIC-getriebenen Metaoberflächen numerisch analysiert und experimentell demonstriert, bei denen die Kopplung zum Fernfeld durch die Verschiebung einzelner Resonatoren gesteuert wird. Insbesondere werden sowohl dielektrische als auch metallische, sowie positive und inverse Verschiebungs-gesteuerte Metaoberflächen untersucht, die winkelunabhängige quasi-BICs im mittelinfraroten Spektralbereich aufrechterhalten. Ihr optisches Verhalten in Bezug auf Änderungen des Einfallswinkels wird analysiert und zeigt experimentell ihre überlegene Winkelstabilität im Vergleich zu zwei konventionellen Alternativen: siliziumbasierte gekippte Ellipsen und zylindrische Nanolöcher in einem kontinuierlichen Goldfilm. Wir gehen davon aus, dass sich aus unseren Einsichten spannende Perspektiven für die Biosensorik, konforme optische Geräte und photonische Geräte mit fokussiertem Licht eröffnen.

Im zweiten Teil dieser Arbeit beginnen wir damit, die Nanophotonik an der Schnittstelle zur Elektrochemie zu untersuchen. Die Elektrokatalyse spielt eine entscheidende Rolle bei der Verwirklichung einer kohlenstofffreien Zukunft über Anwendungen wie die Herstellung grünen Wasserstoffs bis hin zur Reduktion von Kohlenstoffdioxid. Die oberflächenverstärkte Infrarotabsorptionsspektroskopie (SEIRAS) ist eine geeignete Methode zur Untersuchung elektrokatalytischer Prozesse, da sie die Mechanismen der

Reaktionen mit chemischer Spezifität ermitteln kann. Es bleibt jedoch schwierig, viele relevante Aspekte elektrochemischer Reaktionen, wie z.B. kurzlebige Zwischenprodukte, zu erfassen. In dieser Arbeit wird eine integrierte nanophotonisch-elektrochemische SEIRAS-Plattform entwickelt und experimentell umgesetzt, um die molekularen Vibrationssignale in situ während Cyclovoltammetrie zu untersuchen. Eine Platin-Nano-Schlitz-Metaoberfläche wird spektral auf die schwache Schwingungsmode des adsorbierten Kohlenstoffmonoxids bei ≈2033 cm^{-1} angesetzt. Die stark verstärkten elektromagnetischen Nahfeldern erhöhen dann die Intensität der Vibrationssignale. Im Vergleich zu konventionell-ungeordneten Platinfilmen zeigen wir, dass unsere nanophotonisch-elektrochemische Plattform eine 27-fache Verbesserung der experimentell detektierten charakteristischen Absorptionssignale liefert und somit die Erkennung anderer Moleküle mit schwachen Signalen, schnellen Umwandlungen oder niedrigen Oberflächenkonzentrationen ermöglicht.

Im letzten Teil dieser Arbeit erweitern wir unsere nanophotonisch-elektrochemischen Plattform, die eine vielversprechende schmalbandige Technologie zur Untersuchung einzelner Schwingungsmoden elektrochemischer Grenzflächen darstellt, die wir während der CO-Oxidation demonstriert haben. Allerdings beinhalten die meisten Reaktionen mehrere Moleküle oder Adsorptionskonfigurationen. Idealerweise, sollten diese gleichzeitig überwacht werden können, um ein klares Verständnis der zugrundeliegenden elektrochemischen Prozesse zu ermöglichen. Dies erfordert reproduzierbare und breitbandige Sensorsysteme. In dieser Arbeit realisieren wir experimentell mehrbandige Metaoberflächen-basierte SEIRAS zur in-situ Untersuchung der elektrochemischen CO_2-Reduktion auf einer Pt-Oberfläche. Durch die Nutzung unserer reproduzierbaren und spektral abstimmbaren Platin-Nano-Schlitz-Metaoberfläche werden zwei CO-Adsorptionskonfigurationen bei 2030 cm^{-1} und 1840 cm^{-1} lokal verstärkt und detektiert. Unsere Platform kann auf weitere Schwingungsmoden erweitert werden und bietet eine 41-fache Verbesserung bei der Detektion charakteristischer Absorptionssignale im Vergleich zu konventionell-unstrukturierten Platinfilmen. Dank der Signalverstärkung durch unsere Plattform zeigen wir, dass die CO-Brückenkonfiguration auf Platin während der CO_2-Reduktion in einer alkalischen Lösung keine signifikante Rolle spielt.

Durch das nun leichter zu gewinnende Verständnis katalytischer Reaktionen durch unsere nanophotonisch-elektrochemische Plattform, erwarten wir aufregende Perspektiven für elektrochemische SEIRAS, oberflächenverstärkte Raman-Spektroskopie und andere Bereiche der Chemie wie Fotoelektrokatalyse.

Summary

Nanophotonics has firmly established itself as a pivotal force in the transformation and shaping of diverse sectors globally, with a pronounced impact on interdisciplinary scientific research. By effectively bridging disciplinary gaps and seamlessly integrating with other scientific fields, nanophotonics has spearheaded significant breakthroughs in information technology, medicine and healthcare, electronics, life sciences, energy, environmental science, and security, among others. As this interdisciplinary trend is expected to persist, the frontier of future research beckons at the interface between nanophotonics and emerging scientific domains or applications, holding the promise of groundbreaking discoveries yet to be unveiled. In this work, we explore light-matter interactions at the interface to electrochemistry and towards advanced sensing applications.

The first part of this work investigates nanophotonic metasurfaces based on bound states in the continuum (BICs), which are localized electromagnetic modes within the continuous spectrum of radiating waves. Due to their infinite lifetimes without radiation losses, BICs are driving research directions in lasing, non-linear optical processes, and sensing. However, conventional methods for converting BICs into leaky resonances, or quasi-BICs, with high-quality factors typically rely on breaking the in-plane inversion symmetry of metasurfaces. This results in resonances that are strongly dependent on the angle of incidence, making them unsuitable for many practical applications. Here, an emerging class of BIC-driven metasurfaces is numerically analyzed and experimentally demonstrated, where the coupling to the far field is controlled by the displacement of individual resonators. In particular, both all-dielectric and metallic as well as positive and inverse displacement-mediated metasurfaces sustaining angular-robust quasi-BICs are investigated in the mid-infrared spectral region. Their optical behavior with regard to changes in the angle of incidence is investigated and experimentally shows their superior performance compared to two conventional alternatives: silicon-based tilted ellipses and cylindrical nanoholes in gold. These findings are anticipated to open exciting perspectives for bio-sensing, conformal optical devices, and photonic devices using focused light.

In the second part of this work, we explore nanophotonics at the interface of electrochemistry. Electrocatalysis plays a crucial role in realizing the transition toward a zero-carbon future, driving research directions from green hydrogen generation to carbon dioxide reduction. Surface-enhanced infrared absorption spectroscopy (SEIRAS) is a suitable method for investigating electrocatalytic processes because it can monitor with chemical specificity the mechanisms of the reactions. However, it remains difficult to detect many relevant aspects of electrochemical reactions such as short-lived intermediates. Herein, an integrated nanophotonic-electrochemical SEIRAS platform is developed and experimentally realized for the in-situ investigation of molecular signal traces emerging during electrochemical experiments. A platinum nano-slot metasurface

featuring strongly enhanced electromagnetic near fields is implemented and spectrally targets the weak vibrational mode of adsorbed carbon monoxide at ≈2033 cm^{-1}. Compared to conventional unstructured platinum films, we show that our nanophotonic-electrochemical platform delivers a 27-fold improvement of the experimentally detected characteristic absorption signals, enabling the detection of new species with weak signals, fast conversions, or low surface concentrations.

In the final part of this work, we continue to build on our nanophotonic-electrochemical platform that pioneered a promising narrowband technology to study single vibrational modes of electrochemical interfaces during CO oxidation. However, many reactions involve several species or configurations of adsorption. These have to be monitored, ideally simultaneously, to provide a clear understanding of the underlying electrochemical processes. This requires reproducible and broadband sensing platforms. Here, we experimentally realize multi-band metasurface-driven SEIRAS for the in-situ study of electrochemical CO_2 reduction on a Pt surface. By leveraging our reproducible and spectrally tunable platinum nano-slot metasurface, two CO adsorption configurations at 2030 cm^{-1} and 1840 cm^{-1} are locally enhanced as a proof of concept that can be extended to more vibrational bands. Our platform provides a 41-fold enhancement in the detection of characteristic absorption signals compared to conventional broadband electrochemically roughened platinum films. Thanks to the signal enhancement provided by our platform, we show that the CO bridge configuration on platinum does not play a significant role during CO_2 reduction in an alkaline environment.

By providing a deeper understanding of catalytic reactions, the nanophotonic-electrochemical platform is anticipated to open exciting perspectives for electrochemical SEIRAS, surface-enhanced Raman spectroscopy, and other fields of chemistry such as photoelectrocatalysis.

1. Introduction

On a daily basis, we experience and interact with light. We look in the mirror and see our reflection. We stand on the beach and, looking into the water, realize how light is partially reflected and refracted. We understand many of these macro-scale interactions between light and matter intuitively. However, by taking a closer look peculiarities can be noticed. Why is the sky blue at noon? Why does the color of the sky change to red as the sun sets? The answer is small-particle effects, specifically an effect called Rayleigh scattering.[1]

By studying light-matter interactions at different length scales, different physical models apply, each describing a plethora of exotic light-matter or photonic effects. For example, by parameterizing the size of a particle by the ratio

$$x = \frac{2\pi r}{\lambda},$$

(1.1)

where r is the radius of the particle and λ is the wavelength of light, four primary light-matter physics regimes can be discerned. When $x > 1$, the particle scatters light according to its geometric area. When $x \sim 1$, Mie scattering dominates,[2] which will be introduced in Chapter 2. When $x \ll 1$ (but larger than just a few atoms), then Rayleigh scattering dominates based on the formation of a resonance between a particle's dipole moment and an oscillating electromagnetic field. As atomic scales are reached, quantum effects have to be considered. As Richard Feynman famously said, "There is plenty of room at the bottom",[3] meaning that the world is rich in exotic small-scale effects that can be discovered.

Understanding and controlling the properties of light is crucial in modern optics and technology. The generation, guiding, manipulation, amplification, and detection of light has found many applications ranging from optical data communications[4] to imaging,[5] displays,[6] life sciences,[7] health care,[8] and security[9] to name a few. Light as a replacement for conventional technologies promises to improve their speed, capacity, and accuracy.

In particular, light is instrumental in sensor technology. The mid-infrared (mid-IR, spanning from approximately 4000-400 cm^{-1} or 2.5-25 μm)[10] spectrum plays a crucial role in sensing due to its ability to capture molecular absorption patterns linked to chemical bond vibrations. Mid-IR spectroscopy is renowned for its ability to directly analyze molecular structures, such as CO or CO_2, with unparalleled chemical specificity, making it the preferred method for chemical analysis.[11] It is a nondestructive and label-free technique. Nonetheless, the sensitivity of mid-IR spectroscopy is restricted when

dealing with nanoscale samples,[12] biological membranes,[13] or low quantities of surface-bound molecules due to the disparity between mid-IR wavelengths and molecular dimensions.[14] Mid-IR wavelengths are diffraction limited to several microns whereas molecules are typically on the order of magnitude of several nanometers (Figure 1.1).

To overcome this limitation, nanophotonics leverages subwavelength resonators' strong near-field enhancement. By aligning the resonance with absorption fingerprints, enhanced coupling between molecules and resonators can alter either the resonance frequency or strength, facilitating the extraction of molecular information. This concept is known as surface-enhanced infrared absorption spectroscopy (SEIRAS), which has been realized via plasmonic[15] and dielectric[7] platforms.

While metallic systems offer better light confinement, they suffer from Ohmic losses in conduction electrons, making them less efficient in storing energy and providing broader resonances with smaller quality factors (Q factors, defined as the quotient of resonance frequency and linewidth[16]). In contrast, all-dielectric materials experience fewer material-intrinsic losses and primarily face radiative losses, allowing them to achieve higher Q factors.

One effective approach to concentrate and confine light at the nanometer scale is by using nanoparticles with sub-wavelength sizes. Metallic and dielectric nanoparticles are commonly employed, each relying on different physical mechanisms. Metal-based nanoparticles use plasmons, which are collective oscillations of conduction electrons, to enhance and localize light fields.[17] On the other hand, dielectric nanoparticles rely on light coupling resonantly to nonradiative current configurations to achieve similar effects.[18] Both mechanisms result in highly localized near fields, significantly enhancing the interaction between light and nanoscale objects near these resonators.

The subwavelength resonators can also be arranged periodically on a surface forming a metasurface. Metasurfaces are made of artificial subwavelength elements[19] with which light-matter interactions can be tailored at the nanoscale.[20] The development of optical metasurfaces to tailor light-matter interactions on the nanoscale has led to breakthroughs from negative refraction,[21] energy conversion,[22] and ultrathin optical elements[23] to photonic computation.[24]

In the quest for improved and diversified metasurface functionality, features like high-Q factors, long resonance lifetimes, and high electric field confinement have been explored in the literature.[19] To reach these goals, bound states in the continuum (BICs), first described in quantum physics[25,26] and later found to be a phenomenon applying to waves in general, have emerged as a pioneering technology. BICs are discrete and spatially bounded yet exist within the energy range of continuous states. Mathematically, they are vortex centers in the polarization directions of far-field radiation.[27]
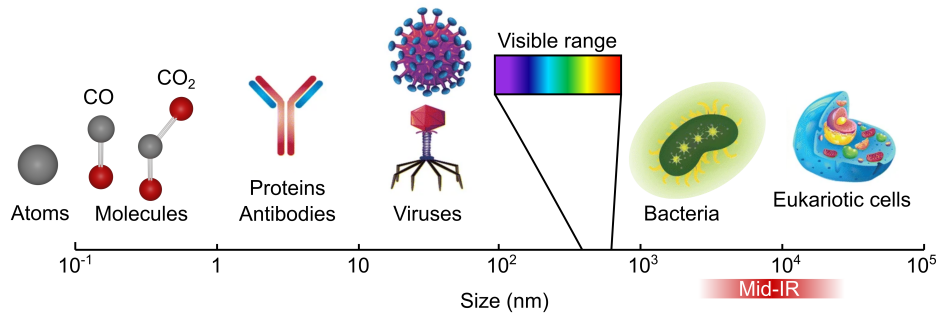
Figure 1.1. Relative size comparison of various microbiological entities. Adapted from Ref.[28] under the terms of the under the terms of the Creative Commons Attribution 4.0 International License (http://creativecommons.org/licenses/by/4.0/).

True BICs have been theoretically predicted in infinite periodic arrays, by appropriately tuning the parameters in the wave equation, either exploiting its separability due to symmetry, tuning its system parameters to find accidental BICs, or reverse engineering them from an artificial potential.[29] Moreover, BICs can exist in single isolated structures as supercavity modes.[30,31] In general, by detuning the system parameters from the BIC condition, a leaky channel is created and the resonance can couple to the continuum with a finite Q factor, called quasi-BIC (q-BIC).[29] Various configurations of nanostructures have been explored to yield high-Q factors in the literature, such as one[32,33] and two-dimensional[34] periodic arrays or radial arrangements.[35]

Typically, metasurfaces featuring BICs are based on dielectric resonators arranged into a periodic array that break the in-plane inversion symmetry to offer both high-Q factors and strong near-field enhancement, enabling state-of-the-art technologies for sensing[7,34] and enhanced light-matter interactions.[36] A similar effect emerges for symmetric metasurfaces sustaining BICs at normal incidence when the angle of incidence is tuned.[37] A few studies[38–41] have been conducted introducing an emerging class of BIC-based metasurfaces that can unlock a finite-Q factor q-BIC resonance by relative displacement tuning while preserving the in-plane inversion symmetry. Another desired aspect of metasurfaces is control over the ratio of their radiative to intrinsic loss rates $\gamma_{ext}/\gamma_{int}$[1] that allows, for instance, for transitions between electromagnetically induced transparency and absorption.[42] Quasi-BICs allow easy control over the radiative[1] Q factor by tailoring the radiative loss rate by changing the asymmetry parameter α.

Apart from a few exceptions,[43,44] studies on nanophotonic or plasmonic metasurfaces yielding high-Q resonances have exclusively focused on (near) normal incidence or angle-multiplexed illumination with experiments focusing on refractive microscope objectives.[45] Unsurprisingly, most conventional metasurfaces based on q-BICs or other nanophotonic or plasmonic principles feature resonances that shift strongly with the

---

[1] See Chapter 2.

angle.[45] While this feature has been exploited for angle-multiplexed sensing,[45] these metasurfaces cannot be used for applications requiring angular robustness (i.e., an optical response that does not vary with incidence angle), such as conformal optical devices, flexible substrate technology, displays, and photonic devices using focused light.[43] To date, there are only very few mentions of angular-robust metasurfaces in the literature[43,46,47] with a further paucity of works aimed at a theoretical understanding of angular robustness.[48,49] For example, one study proposed a gold-based metasurface featuring a resonance that was excited at a small range of incidence angles wherein it showed angular robustness.[37] However, the proposed metasurface required femtosecond laser writing in photoresist to make structures with different heights, which is difficult with electron beam lithography. Until now, a fundamental and systematic study on angular-robust BIC-driven metasurfaces was missing.

While we have so far introduced a nanophotonic application, it can generally be said that the undiscovered lies at the interface between different established scientific fields, which promises the potential for rich scientific discoveries and breakthrough technologies. For example, at the interface between photonics and medicine diagnostic imaging devices (such as magnetic resonance imaging or positron emission tomography), new cures (such as the treatment of cancer by subwavelength metal particles irradiated by high-intensity achromatic light that causes local heating and burning of the cancer cells),[8] biosensors (such as the lateral flow pregnancy or rapid COVID-19 antigen test), and more. Light-based sensors are used in biomedicine, environmental monitoring, telecommunications, spectroscopy, quantum technology, and more. At the interface to energy science, light can even be converted to other forms of energy. For example, it can be used to drive photoelectrochemical reactions for energy storage or be used to convert light into electric signals and vice versa for optoelectronic circuits.

In particular, the interface between nanophotonics and electrochemistry is a relatively unexplored field. Understanding electrochemical reactions is crucial to improve their efficiency and to bridge the gap towards a sustainable zero-carbon future. However, it remains difficult to detect many relevant aspects of electrochemical reactions, such as short-lived intermediates.

The carbon dioxide reduction reaction (CO_2RR) is a vital component in addressing global warming as a consequence of the world's disrupted carbon cycle. The CO_2RR can lead to many products and intermediates depending on the choices of catalyst design, reactor architecture, and process conditions.[50] Although high-carbon products might seem preferable, they require significantly higher energy costs and suffer from lower selectivities and efficiencies. As the number of proton-electron exchanges increases, as it does in high-carbon products, the reaction becomes less efficient.[51] Therefore, the current priority relies on reducing CO_2 to simple and small building block molecules that can be upconverted to C_{2+} products.[50] Carbon monoxide production is the most promising, low-cost, scalable CO_2RR product[50] requiring only a simple two-electron transfer

$$CO_2 + 2H^+ + 2e^- \rightarrow CO + H_2O. \qquad (1.2)$$
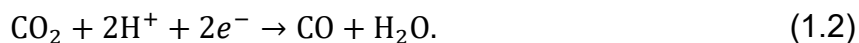
Carbon monoxide, when combined with hydrogen, generates syngas, which serves as a vital precursor for the production of various transportation fuels like jet fuel, diesel, and gasoline via further processing. The production of liquid fuels through renewable electrosynthesis has the potential to prevent the emission of 10,700 megatons of CO_2 by 2030.[50] However, a number of macroscale issues remain in the CO_2RR to CO, such as up-scaling, losses of CO_2 in the electrolyte as carbonate, or increasing the CO concentration gas product.[50] To solve these macroscale problems, a better understanding of the underlying microscale chemical processes needs first to be gained. In particular, the adsorption mechanisms of CO on different materials during the CO_2RR under different experimental conditions are still not fully understood as the signals are weak and difficult to resolve.

SEIRAS is often performed to investigate these processes since it allows to monitor with chemical specificity the mechanisms of the reactions. Until now, the use of SEIRAS in electrochemistry has faced significant difficulties due to the challenges associated with reproducibly preparing SEIRAS active electrodes. Previous approaches for electrode fabrication involved specific film preparation methods that required (often electrochemical) film roughening, leading to limited reproducibility. The corners, tight spots, and edges of the roughened metallic film lead to uncontrolled, randomized, and localized electromagnetic field enhancement, which is harnessed to increase the characteristic molecular signal traces. Until now, a reproducible approach for creating SEIRAS-active electrodes, featuring controlled and targeted signal enhancement of the in-situ generated characteristic molecular signal traces during an electrochemical experiment, was missing.

2. Theory

In the following section, we will introduce the theoretical frameworks that underpin the fundamental physical and chemical principles presented in this work. Our theoretical descriptions follow Ref.[17,42,48,49,52–57]

2.1 Understanding Light-Matter Interactions

A comprehensive analytic theory describing all light-matter interactions does not yet exist. For different dimension ranges, material classes, wavelength ranges, and object shapes there exist a plethora of detached analytical or phenomenological physical theories. Where theories become elusive, numerical models can generally still be useful.

The interaction between light and matter can be numerically modeled by subdividing a simulation space into units that are smaller than 1/8 the wavelength of light, choosing appropriate boundary conditions between the subunits, and calculating the propagation of light through them by solving Maxwell's equations in an iterative manner. This method of systematically converting functions in an infinite dimensional function space to a discrete set of linked functions or vectors is called the finite element method. After each iteration, an error is calculated and minimized. The materials can be modeled by their refractive index.

In principle, this approach promises to work for any light-matter interaction. In practice, however, this approach becomes very time-consuming and cumbersome when large objects are modeled, meaning where at least one dimension of the object is much larger than the wavelength. In that regime, the interaction between the objects and light is better understood by representing light as rays and studying their diffraction through objects. On the other hand, if objects become too small, on scales of just a few atoms, quantum mechanical effects need to be considered and a treatment from a purely classical point of view will no longer predict accurate results.

Therefore, to gain a deeper understanding of light-matter interactions numerical models alone are limited in their ability to explain physical phenomena. They need to be supplemented with the necessary theoretical frameworks to understand the underlying physics, extrapolate results, or help achieve certain phenomena that would be hard to find via conjectures. In the following, we will introduce the theory necessary to understand the results shown in this work.

2.1.1 Maxwell's Equations

The macroscopic Maxwell's equations predict the electromagnetic response of materials down to a few nanometers in size at room temperature. In a real material the constituent charged particles interact with incident electromagnetic fields causing rapidly varying microscopic fields. In a phenomenological approach, these can be ignored and their averaged effect can be described over distances much larger than the underlying microstructure.

Maxwell's equations link four macroscopic fields together, namely the dielectric displacement field **D**, the magnetic induction or magnetic flux density **B**, the electric field **E**, and the magnetic field **H**, with the external charge and current densities ρ_{ext} and $\mathbf{J}_{\text{ext}}$. The macroscopic Maxwell's equations read:

$$\nabla \cdot \mathbf{D} = \rho_{\text{ext}} \tag{2.1}$$

$$\nabla \cdot \mathbf{B} = 0 \tag{2.2}$$

$$\nabla \times \mathbf{E} = -\frac{\partial \mathbf{B}}{\partial t} \tag{2.3}$$

$$\nabla \cdot \mathbf{H} = \mathbf{J}_{\text{ext}} + \frac{\partial \mathbf{D}}{\partial t}. \tag{2.4}$$

The total charge and current densities $\rho_{\text{tot}} = \rho_{\text{ext}} + \rho$ and $\mathbf{J}_{\text{tot}} = \mathbf{J}_{\text{ext}} + \mathbf{J}$, respectively, can be separated into their external (ρ_{ext}, $\mathbf{J}_{\text{ext}}$) and internal (ρ, $\mathbf{J}$) components. The external components drive the system while the internal ones respond.

The polarization **P** and magnetization **M** link the four macroscopic fields as

$$\mathbf{D} = \varepsilon_0 \mathbf{E} + \mathbf{P}, \tag{2.5}$$

$$\mathbf{H} = \frac{1}{\mu_0} \mathbf{B} - \mathbf{M}, \tag{2.6}$$

where ε_0 and μ_0 are the electric permittivity and magnetic permeability of vacuum, respectively. If we consider nonmagnetic media only we can neglect **M**. **P** is the macroscopic density of permanent and induced electric dipole moments in the material. As shown in equation (2.5), an electric displacement field emerges due to an incident electric field **E** and the response of a material's free and bound charges to that electric field in terms of how well their permanent and induced dipoles align with it. The polarization is related to the internal charge and current densities via

$$\nabla \cdot \mathbf{P} = -\rho, \tag{2.7}$$

$$\mathbf{J} = \frac{\partial \mathbf{P}}{\partial t}, \tag{2.8}$$

Due to charge conservation, the internal charge and current densities are linked to each other by

$$\nabla \cdot \mathbf{J} = -\frac{\partial \rho}{\partial t}. \tag{2.9}$$

By inserting equation (2.5) into equation (2.1) we obtain

$$\nabla \cdot \mathbf{E} = \frac{\rho_{\text{tot}}}{\varepsilon_0}, \tag{2.10}$$

which shows that both the external and induced fields are absorbed into it.

For linear isotropic media equation (2.5) and (2.6) become

$$\mathbf{D} = \varepsilon_0 \varepsilon \mathbf{E}, \tag{2.11}$$

$$\mathbf{B} = \mu_0 \mu \mathbf{H}, \tag{2.12}$$

where ε and μ are called the relative permittivity and permeability, respectively.

2.1.2 The Relative Permittivity

Following Maier[17] (above) and under the assumptions of linear, isotropic and nonmagnetic media, a fundamental relationship between the relative permittivity and the conductivity σ can be derived as

$$\varepsilon(\mathbf{K}, \omega) = 1 + \frac{i\sigma(\mathbf{K}, \omega)}{\varepsilon_0, \omega}, \tag{2.13}$$

where $\mathbf{K}$ is the wave vector and ω is the angular frequency. As long as the wavelength of incident light is longer than the characteristic dimensions of the material, such as the unit cell of an electron's mean free path, the relative permittivity can be simplified to a spatially local response $\varepsilon(\mathbf{K} = 0, \omega) = \varepsilon(\omega)$. In that case, ε mainly describes the response of bound charges to an incident electromagnetic field, while σ predicts the current flow due to the free charges. This separation becomes blurred at optical frequencies.

Due to the arguments made in section 2.1.1, the response of a material to light can be modeled via its relative permittivity. According to equation (2.13) the conductivity can be used as well. The relative permittivity and conductivity are in general complex functions $\varepsilon(\omega) = \varepsilon_1(\omega) + i\varepsilon_2(\omega)$ and $\sigma(\omega) = \sigma_1(\omega) + i\sigma_2(\omega)$, respectively. A straightforward approach to obtaining the complex and frequency dependent relative permittivity and

conductivity is via the experimental retrieval of a material's complex refractive index $\tilde{n}(\omega) = n(\omega) + i\kappa(\omega)$ and linking $\tilde{n} = \sqrt{\varepsilon}$. The real part of $\tilde{n}$ quantifies the decrease of the light's phase velocity. This should not be confused with the group velocity of light in a material which is given by $v_g = \frac{c}{\sqrt{\varepsilon\mu}}$, where $c = \frac{1}{\sqrt{\varepsilon_0\mu_0}}$ is the speed of light in vacuum. κ determines the absorption of light passing through a medium and is linked to the absorption coefficient of Beer's law as

$$A(\omega) = \frac{2\kappa(\omega)\omega}{c}. \tag{2.14}$$

Beer's law predicts the exponential attenuation of the intensity of light passing through a medium occurs via $I(x) = I_0 e^{-Ax}$.

2.1.2.1 *The Relative Permittivity of Dielectric Materials*

Dielectric and semiconductor materials are characterized by having low optical losses. The refractive index consists of a small imaginary part and is often not significantly dispersive. Therefore, the optical response of dielectric or semiconductor materials in the vis-to-IR range can often be modeled by considering a real dielectric constant $\varepsilon = \sqrt{n^2}$.

2.1.2.2 *The Relative Permittivity of Metals: The Free Electron Model*

Metals are lossy materials characterized by a complex and dispersive refractive index. In the vis-to-IR range, their refractive index should not be considered purely real due to their strong optical losses. Their refractive index should also not be approximated as a constant due to a metal's strong dispersion. To model metals, their relative permittivity can either be experimentally determined, e.g. via ellipsometry,[58] or approximated by taking into account the findings provided by the free electron model.

The free electron model was conceptualized in 1927 by Arnold Sommerfeld[59] as a combination of the classical Drude model developed in 1900[60] and quantum mechanical Fermi-Dirac statistics to describe metals. The free electron model describes the permittivity and therefore the optical properties of metals in the intraband transition regime, below the spectral region attributed to interband transitions, which varies across different metals. The free electron model assumes a fixed background of positive ions with an overlaid free electron gas with number density *n*. It does not take into account

details in the lattice structure of the underlying metals nor any electron-electron interactions. The relative permittivity of the free electron gas can be written as

$$\varepsilon(\omega) = 1 - \frac{\omega_p^2}{\omega^2 + i\gamma\omega},$$ (2.15)

which is also called the Drude model.

Due to the limitations of the model, it only performs reasonably well up to the onset of the interband transitions. In terms of making the Drude model more accurate in describing the optical response of noble metals, such as gold, a few approaches have been outlined in the literature.[61] A straightforward approach is the introduction of a dielectric constant ε_∞ (typically $1 \leq \infty \leq 10$) to mitigate polarization effects at high frequencies ($\omega > \omega_p$) where s electrons are excited to higher states. Since the noble metals have filled d orbitals close to the Fermi surface the s electrons are free causing a strongly polarized material. The permittivity correction for noble metals then reads

$$\varepsilon(\omega) = \varepsilon_\infty - \frac{\omega_p^2}{\omega^2 + i\gamma\omega}.$$ (2.16)

2.1.3   Defining Features of Nanophotonic Systems

Photonic systems can be described by a system of oscillators with the ability to store energy for certain resonant conditions. Specifically for photonic systems, resonances can store electromagnetic energy by confining light in tight spots. The efficiency of light confinement is related to the Q factor of a resonance, defined as the quotient of the energy stored in an optical system on resonance $h\nu_0$ and its energy loss $h\Delta\nu$, where ν_0 and $\Delta\nu$ is the resonance frequency and linewidth and h is Planck's constant. The Q factor can be written as

$$Q = \frac{\nu_0}{\Delta\nu}.$$ (2.17)

To maximize the Q factor and therefore the ability of the system to store energy, two channels of loss have to be considered. First, nonradiative damping occurs due to intrinsic losses of the resonator or surrounding material, which are described by the complex refractive index. To minimize nonradiative losses, materials with high n and low κ need to be employed. Metals typically suffer strongly from material losses in the vis-to-IR range. Semiconductors, such as Si and Ge, are good choices for the spectral region on the red side of interband transitions. Nonradiative damping coming from lossy environments can be minimized by considering special geometries, such as mode excitation in attenuated

total internal reflection (ATR). Secondly, radiative damping due to light scattering can remove energy from the system.

Nonradiative and radiative losses can be quantified in terms of the intrinsic γ_{int} and radiative γ_{rad} damping rates, respectively. With these, the radiative and nonradiative Q factors can be calculated as

$$Q_{\text{rad}} = \frac{\nu_0}{2\gamma_{\text{rad}}}, \tag{2.18}$$

$$Q_{\text{int}} = \frac{\nu_0}{2\gamma_{\text{int}}}, \tag{2.19}$$

respectively. The total Q factor, provided in equation (2.17), can then also be written as

$$Q = \frac{\nu_0}{2(\gamma_{\text{rad}} + \gamma_{\text{int}})}. \tag{2.20}$$

Nonradiative and radiative losses are related to the absorption σ_{abs} and scattering σ_{sca} cross-sections

$$\sigma_{\text{abs}} = \kappa \Im[\alpha], \tag{2.21}$$

$$\sigma_{\text{sca}} = \frac{\kappa^4}{2\pi}|\alpha|^2, \tag{2.22}$$

respectively. The extinction cross-section is the sum of absorption and scattering cross-sections

$$\sigma_{\text{sca}} + \sigma_{\text{abs}} = \sigma_{\text{ext}}. \tag{2.23}$$

Both are related to the polarizability α, which relates an electric dipole **p** to an electric field **E** as

$$\mathbf{p} = \alpha\mathbf{E}, \tag{2.24}$$

The polarizability and therefore scattering cross-section can be decreased by minimizing the dipole moment(s) associated with the resonance(s) in a nanostructure. The dipole moments in resonators can be minimized by destructive interference of different resonant modes, for example in anapole states and bound states in the continuum.

The underlying concept of Fano resonances, initially introduced by Ugo Fano in 1961,[62] is the interference between a discrete state and a continuum. They can be generalized to resonances of different linewidths and associated damping constants coupling with each other. Fano resonances are inherently asymmetric with the degree of asymmetry being governed by the Fano parameter q, with the Fano resonance line profile given by

$$F(\epsilon) = \frac{(\epsilon + q)^2}{\epsilon^2 + 1}, \tag{2.25}$$

where

$$\epsilon = 2(E - E_0)/\gamma \tag{2.26}$$

is the reduced energy with $E = h\nu$ and $E_0 = h\nu_0$.

The anapole can be realized by carefully engineering nanostructures for the destructive interference of their electric and toroidal dipoles.[63] Bound states in the continuum will be explained in section 2.1.1.

2.1.4 Metallic Nanostructures: From Plasmonics to the Mid-IR

2.1.4.1 Surface Plasmon Polaritons at a Single Interface

Surface plasmon polaritons are coupled light-surface electron waves that propagate across a dielectric-metal interface. A simple geometry to describe surface plasmon polaritons is composed of two half-spaces separated in *z* and considering *p* polarized light. No surface plasmon polaritons can be excited at the interface for *s* polarized light. One half space is filled with media having a positive real dielectric constant ε_2 and an adjacent conducting half space is described via a complex dielectric function $\varepsilon_1(\omega)$, where $\Re[\varepsilon_1] < 1$. Negative real permittivity materials are metals at higher frequencies than the bulk plasmon frequency ω_p, so we will continue to use the term metal interchangeably with negative real permittivity material. It can be shown[17] that the electric near fields in *z* decay evanescently away from the interface. In general, the confinement of an electromagnetic field is given by

$$\hat{z} = \frac{1}{|k_z|}, \tag{2.27}$$

where k_z is the component of the wavevector extending in the *z*-direction. Furthermore, it can be shown that

$$\frac{k_{z_2}}{k_{z_1}} = -\frac{\varepsilon_2}{\varepsilon_1} \tag{2.28}$$

and

$$k_{z_1}^2 = \beta^2 - k_0^2 \varepsilon_1, \tag{2.29}$$

12

$$k_{z_2}^2 = \beta^2 - k_0^2 \varepsilon_2^2, \tag{2.30}$$

where β is the wavevector of the surface plasmon polartion and k_{z1} and k_{z2} describe the conducting and dielectric half-space, respectively. By combining equations (2.28), (2.29), and (2.30) we find the dispersion relation of the surface plasmon polariton propagating between the interface as

$$\beta = k_0 \sqrt{\frac{\varepsilon_1 \varepsilon_2}{\varepsilon_1 + \varepsilon_2}}. \tag{2.31}$$

2.1.4.2   *The Quasi-Static Approximation for Sub-Wavelength Metal Particles*

For metallic sub-wavelength particles surrounded by a dielectric environment a phenomenon called the localized surface plasmon resonance can occur, in the visible range for gold nanoparticles. Incident electromagnetic waves can couple with conduction electrons to produce a non-propagating resonance driven by the oscillating electric field of the incident light wave and dampened by the curved surface of the particle. Field amplification occurs both inside the particle and in its near-field vicinity. Due to the curved surface, no phase-matching techniques need to be employed, unlike for the excitation of surface plasmon polaritons and the resonance can be excited by direct light illumination. The principal or reddest resonance is the main localized surface plasmon resonance. It describes particles less than 100 nm in size.

We can calculate these modes by considering a particle of size d much smaller than the wavelength $d \ll \lambda$. Then, across the particle, the phase of the electromagnetic wave will only minimally change. We can assume an electrostatic field surrounding a metallic sphere of radius a neglecting the phase change. After the field distributions are known, a harmonic time dependence can be included. Starting from the Laplace equation of the potential and following Jackson[64] it can be shown that a solution exists in the electrostatic approximation. As it turns out, the applied electric field induces a dipole moment $\mathbf{p}$ inside the sphere as

$$\mathbf{p} = 4\pi\varepsilon_0\varepsilon_m a^3 \frac{\varepsilon - \varepsilon_m}{\varepsilon + 2\varepsilon_m}\mathbf{E}_0, \tag{2.32}$$

where ε_m is the real dielectric constant of the surrounding dielectric and $\varepsilon = \varepsilon(\omega)$ is the dielectric function of the metal. Since the dipole moment is related to the electric field $\mathbf{E} = \varepsilon\varepsilon_m\mathbf{E}_0$ via equation (2.24) the polarizability α is

13

$$\alpha = 4\pi a^3 \frac{\varepsilon - \varepsilon_m}{\varepsilon + 2\varepsilon_m}. \tag{2.33}$$

To maximize α, the term $|\varepsilon + 2\varepsilon_m|$ needs to be minimized, which for slowly varying $\Im[\varepsilon]$ occurs at the condition

$$\Re[\varepsilon(\omega)] = -2\varepsilon_m. \tag{2.34}$$

Equation (2.34) is the Fröhlich condition. It describes the dipole surface plasmon mode of a sub-wavelength metal nanoparticle in an oscillating electric field.

By using the Optical Theorem it can be demonstrated[54,65] that the extinction cross-section for small spherical particles can be written as

$$\sigma_{\text{ext}} = \sqrt{\varepsilon_m} k_0 \Im[\alpha], \tag{2.35}$$

Where $k_0 = 2\pi/\lambda_0$ is the free space wavenumber and $\sigma_{\text{ext}} = \sigma_{\text{sca}} + \sigma_{\text{abs}}$ is the combined absorbed and scattered cross-section. Equation (2.35) implies that the extinction cross-section can be much larger than the physical size of the particle.

2.1.4.3   *Beyond the Quasi-Static Approximation*

There are two cases for metal particles in dielectric media for which the quasi-electrostatic approximation breaks down. First, for larger particles retardation effects due to phase differences within the particle need to be considered. Secondly, for very small metal particles with $d < 10$ nm the quasi-static approximation breaks down due to the mean free path of the conduction electrons being significantly smaller than the wavelength of light. We will limit our discussion to larger particles.

Keeping our nomenclature presented in section 2.1.4.2, the polarizability of a sphere of volume V with retardation effects can be shown[66,67] to be

$$\alpha_{\text{Mie}} = \frac{1 - \left(\frac{1}{10}\right)(\varepsilon + \varepsilon_m)x^2 + O(x^4)}{\left(\frac{1}{3} + \frac{\varepsilon_m}{\varepsilon - \varepsilon_m}\right) - \frac{1}{30}(\varepsilon + 10\varepsilon_m)x^2 - i\frac{4\pi^2\varepsilon_m^{3/2}}{3}\frac{V}{\lambda_0^3} + O(x^4)} V, \tag{2.36}$$

where $x = \frac{\pi a}{\lambda_0}$. Equation (2.36) is the result of an expansion of the first p polarized mode of Mie theory.[2] As can be seen, more terms appear in both the numerator and denominator making a maximization of the polarizability less straightforward. The consequence for noble metals is a redshift in the resonance as the radius of the particle

---

[2] Mie theory will be discussed in Chapter 2.1.3.1.

is increased. As the size of the particle increases, so does the distance between the charges on opposing sides of the surface of the particle leading to a smaller restoring force and resonance redshift. Due to the redshift, the resonance is moved further away from the regime of interband transitions lessening their effects. This effect is captured by the term quadratic in *x* in the numerator, whereas the same term in the denominator implies a competing effect between radiative and nonradiative decay. For larger particles, the radiative decay into phonons dominates, whereas for smaller particles the prevailing decay mechanism is nonradiative into electron-hole pairs.

2.1.4.4   Single Metallic Nanorods

Nanorods or nanoantennas are hyperrectangles with height *h*, width *w,* and length *l*. They can couple to incident light whether they are isolated particles or appear in various arrangements of similar particles. The localized surface plasmon resonance of single nanorods can be described phenomenologically as a Fabry-Perot cavity with a resonance condition that must fulfill $\sin(k_{\mathrm{eff}}l) = 0$,[54] where $k_{\mathrm{eff}} = 2\pi/\lambda_{\mathrm{eff}}$ is the mode wavevector along the direction of polarization. This gives

$$\lambda_{\mathrm{eff}} = \frac{2l}{n}, \tag{2.37}$$

where *n* is any integer number. The mode wavelength λ_{eff} varies from the incoming wavelength λ depending on the frequency range, geometry, and environment. For example, at long wavelengths such as at the radio and microwave spectral ranges, the high permittivity of metals means external electromagnetic fields cannot penetrate deeply into them. Consequently, no resonance of conduction electrons can emerge and the relationship between λ and λ_{eff} is completely governed by the particles geometry. At higher frequencies, plasmonic effects become more important.

2.1.4.5   Nanoparticle Arrays and Coupling Effects

A two-dimensional array of particles will scatter light in multiple ways. First, due to the order in the system coherent scattering effects emerge. According to Bloch's theorem[68,69] a relationship between the in-plane wavevector for the diffraction orders {*m,n*} and the geometry of the structure can be written as

$$\mathbf{k}_{mn} = \mathbf{k}_{inc} + m\frac{2\pi}{d_1}\mathbf{u}_1 + n\frac{2\pi}{d_2}\mathbf{u}_2, \tag{2.38}$$

where $\mathbf{k}_{inc}$ is the in-plane wavevector and d_1 and d_2 are the pitch along the unit cell vector $\mathbf{u}_1$ and $\mathbf{u}_2$, respectively. The unit cell is the smallest repetitive unit volume that makes up a metasurface. Equation (2.38) describes a phenomenon closely related to the Rayleigh[70] and Wood's[71] anomalies. These describe an effect that occurs when light is diffracted by metallic gratings. Therefore, we will call the effect described by equation (2.38) the Rayleigh-Wood anomaly mode (RA). The collective electromagnetic resonances are spectrally narrow and spatially extended.

Under an arbitrary angle of incidence the RA shifts according to

$$|\mathbf{k}_{mn}| = k_0 \qquad (2.39)$$

implying only a non-zero component of the scattered radiation parallel to the plane of the array. The incident electromagnetic fields are scattered into grazing waves, which can travel across multiple resonators without radiating into the far field. Hybridization effects between metasurface-driven resonances and the RA have been predicted[72] and reported.[73]

As the frequency is increased across the first or lowest frequency RA mode, the photonic system transitions from being dominated by evanescent to radiative losses.[74] Therefore, to extend the lifetime of resonances and the electromagnetic near-field enhancement, the resonance should be on the evanescent side of the first RA. Since high-Q factors and high-electromagnetic near-field enhancements are required for strong sensing performance, the RA should be tuned to the high-frequency side of the resonance.

To understand how a single-particle resonance will shift when the particle is placed in a periodic array we can use the coupled dipole approximation.[75] For spherical particles in an array an effective polarizability can be calculated as

$$\alpha' = \frac{\alpha}{1 - \alpha S}, \qquad (2.40)$$

where α is the polarizability of the particle, given for small particles ($d \ll \lambda$) by equation (2.33). For infinite periodic arrays

$$S = \sum_{i \neq j} \left[\frac{(1 - i\sqrt{\varepsilon_m}k_0 r_{ij} - 1)(3\cos^2\theta_{ij} - 1)}{r_{ij}^3} + \frac{\varepsilon_m k_0^2 \sin^2\theta_{ij}}{r_{ij}} \right] e^{i\sqrt{\varepsilon_m}k_0 r_{ij}}, \qquad (2.41)$$

where r_{ij} is the interparticle distance and θ_{ij} is the angle between $\mathbf{r}_{ij}$ and the direction of polarization.

In general, we will refer to artificial two-dimensional materials composed of periodically arranged subwavelength building blocks as metasurfaces.[19]

2.1.4.6   Towards the Mid-IR: The Lightning Rod Effect

As the resonance of metallic particles is shifted to longer wavelengths towards the mid-IR the quasi-static approximation and the Froehlich condition, given in equation (2.34), no longer hold. It can be readily verified that both the real and imaginary parts of ε_m diverge strongly from zero for metals. This prevents electromagnetic fields from penetrating deeply into metals in the mid-IR as the bulk and surface electrons oppose them. Then, it becomes more accurate to describe nanoparticles by the lightning rod effect, which describes ideal conductors and their expulsion of the electric field.[76] The wavelength of mid-IR light and longer wavelengths are longer than the wavelength associated with the surface electron modes. Therefore, no more coupling between the surface electron waves and incident light takes place, and the particles are no longer polarized by light.

The lightning-rod effect can be described semi-analytically for arrays of metallic nanoparticles with arbitrary shapes using an electrostatic model.[76] Since the lightning rod effect describes protruding particle arrays but not their inverse, such as holes in a continuous metallic film, we will describe mid-IR resonances as metasurface-driven. As we show below, the resonances in the mid-IR exhibit qualitative similarities to plasmonic resonances.

Specifically, if we look at how surface plasmon polaritons transform as the wavelength is increased, we need to look at equation (2.32). As can be seen, for long wavelengths (mid-IR or longer) β converges to k_0 as both the real and imaginary part of $\varepsilon_1(\omega)$ diverge from zero towards infinity. From equations (2.29) and (2.30) it becomes apparent that the surface waves are no longer well confined close to the conductor-dielectric interface. They can spatially extend multiple wavelengths into the dielectric. The surface plasmon polaritons therefore become Sommerfeld-Zenneck waves,[77] acquiring the character of a grazing-incidence light field.
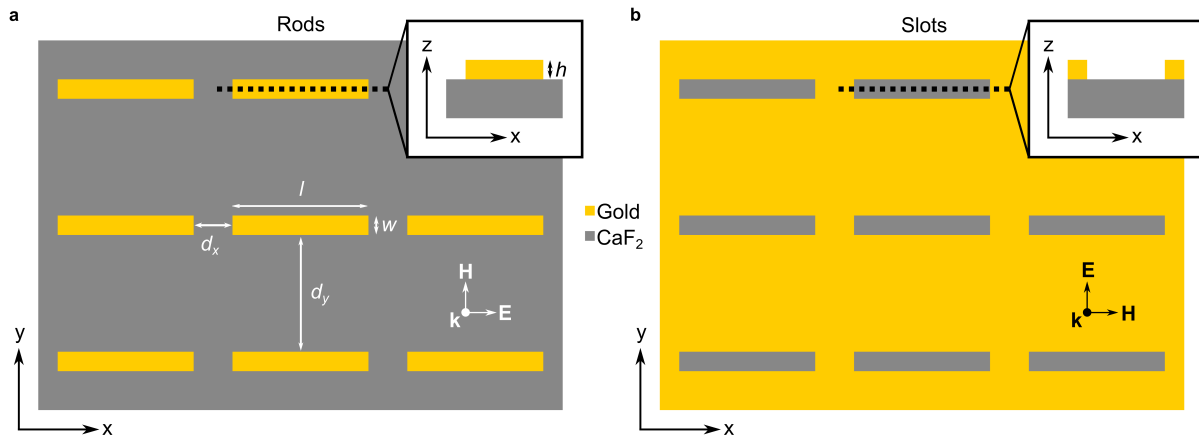
Figure 2.1. Schematic of (a) rods and (b) slots in a periodic array along with relevant geometrical parameters. The polarization of incident light able to excite (a) the electric dipole of the rods and (b) magnetic dipole of the slots is indicated, where **E** and **H** are the incident electric and magnetic field vectors, and **k** is the Poynting vector.

2.1.4.7   *Nanorod, Nanoslot Arrays, and Babinet's Principle*

There are a multitude of shapes and arrangements of metal particles that feature a localized surface plasmon resonance in the visible to NIR range. Once these particles are arranged into a periodic two-dimensional array, coupling effects between the unit cells become apparent. The unit cell is the smallest repetitive unit volume that makes up a metasurface. As the resonance is shifted to longer wavelengths towards the mid-IR, the quasi-static approximation no longer holds and we call the resonance metasurface-driven. In that spectral range, metals, such as gold or platinum, can be treated as perfect conductors due to their high conductivity and their real and imaginary permittivity diverging from zero.

Babinet's principle relates two complementary metasurfaces made of perfectly conducting elements. Two complementary metasurfaces form a continuous perfectly conducting film when superimposed on each other. For metasurfaces composed of highly conducting elements, Babinet's principle predicts that the optical response of two complementary metasurfaces will be qualitatively similar under a 90-degree change in polarization under a change in light collection from reflection to transmission or vice versa. Babinet's principle is a powerful tool in understanding metasurfaces. If a metasurface composed of thin and highly conducting elements is understood in reflection (transmission) the physical behavior in transmission (reflection) of its inverse complement can be predicted via Babinet's principle. The resonance position will be similar for two complementary metasurfaces.
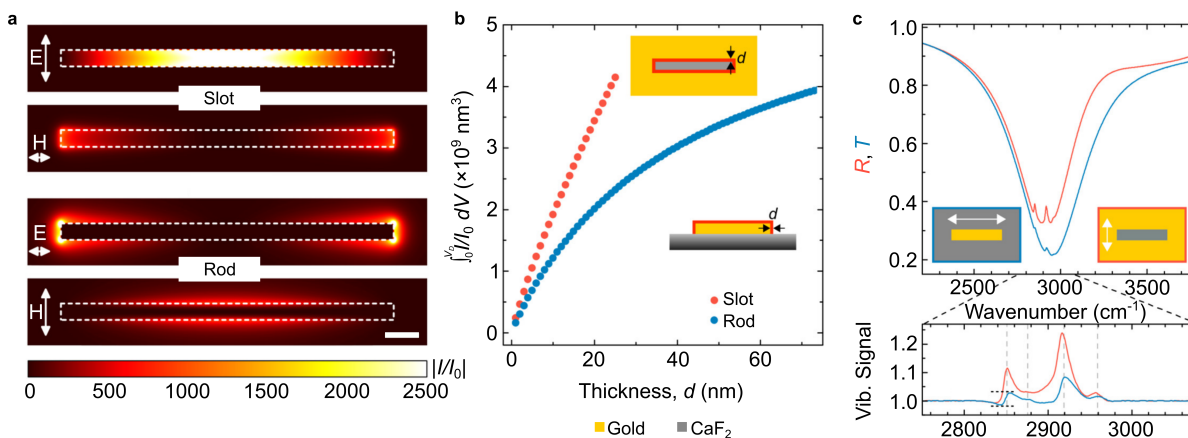
Figure 2.2. Comparing nanorods with nanoslots. (a) Electric near-field intensity distributions of resonantly excited nanoslot and nanorod arrays on the surface plane at half the depth (height) of the slots (slots). The local electric near-field intensity I is divided by the intensity of incident light I_0. (b) Integrated electric near-field intensity (plotted on y axis) surrounding the nanostructure (inset) as the volume of integration is increased by a thickness parameter d. (c) The IR reflectance (transmittance) of a nanoslot (nanorod) array, covered with a monolayer of octadecanethiol. Both arrays have the same dimensions. The lower panel displays the vibrational signal of octadecanethiol after baseline correction. The peaks correspond to the symmetric and asymmetric stretching vibrations of the CH_2 and CH_3 groups of octadecanethiol, indicated by dashed vertical lines. Reprinted (adapted) with permission from Ref.[52] Copyright 2015 American Chemical Society.

Nanorods, whether singular or in an array (Figure 2.1a), can exhibit a resonant electric dipole for p polarized light at a characteristic resonant frequency, qualitatively similar to plasmonic rods in the vis-to-NIR (Figure 2.2a). The electric near-field enhancement will be at the tips of the rods. In contrast, their inverse complement, slots (Figure 2.2), feature a magnetic dipole resonance under a 90-degree change of polarization for s polarized light with the electric near field confined to the center of the slot (Figure 2.2a). Interestingly, the electric near-field intensity decays exponentially from the outer surfaces of rods and linearly from the inner surfaces of the slots (Figure 2.2b). In the context of sensing, the externalized and linearly decaying near fields provide higher signal-to-noise ratios for slot compared to rod metasurfaces (Figure 2.2c).

In the NIR, coupling effects have been found to be stronger for slots than for rods, which makes their parametric optimization necessary. Whereas rods have been found to couple via photons inside a transparent substrate, slots have been found to couple via surface plasmon polaritons at the conductor-dielectric interface. A rigorous study on the exact coupling mechanisms of rods or slots in the mid-IR is still missing. For this reason, we will summarize the findings of Huck et al.[52] for rods and slots in the NIR. The Q factor,

extinction, and signal enhancement are maximized for slots for $d_x = d_y = \lambda_{res}/2$ (see Figure 2.1 for the parameter definition), where λ_{res} is the resonance wavelength. Interestingly, the optimum condition was found to be independent of the refractive index of the substrate n_s. The optimum for rods was found when $d_y = \lambda_{res}/n_s$. These conditions change with the angle of incidence and spectral frequency.

2.1.5 Mie Theory: Connecting Metallic and Dielectric Nanoparticles

In a seminal paper in 1908, Gustav Mie derived analytical equations describing the interaction of a spherical particle with light of a similar wavelength to the size of the particle to explain the red colors of colloidal gold.[2] He discovered that a set of normal electric and magnetic eigenmodes exist inside a spherical particle that govern its characteristic electromagnetic response in terms of light scattering and absorption. Mie's approach to expanding the scattered and internal electric and magnetic fields into a set of normal modes using vector harmonics has culminated in what is now called Mie's theory and unifies light-matter interactions from Rayleigh scattering (very small particles) to geometrical optics (large particles). The size of particles is stated relative to the wavelength of light or the mean free path of conduction electrons in the case of metals. For subwavelength particles, the quasi-static approximation given in section 2.1.4.2 can be recovered via a power series expansion of the scattering and absorption coefficients and retention of only the first term. Although Mie theory is limited to spherical particles, it provides a first-order description of the light-matter interactions of non-spherical particles and is therefore useful in capturing the optical effects of small particles.

A physically realizable time-harmonic electromagnetic field in a linear, isotropic, homogenous medium must satisfy Helmholtz equations for **E** and **H**

$$\nabla^2 \psi + k^2 \mathbf{E} = 0, \tag{2.42}$$

$$\nabla^2 \psi + k^2 \mathbf{H} = 0, \tag{2.43}$$

where $k^2 = \omega^2 \varepsilon \mu$. The electric and magnetic fields must satisfy Maxwell's equations (2.1), (2.2), (2.3), and (2.4). For a sphere of radius R with $\varepsilon \mu$ surrounded by a dielectric medium with n=1, Helmholtz equations can be solved to construct even ψ_{emn} *and* odd ψ_{omn} generating functions in spherical polar coordinates (r, θ, ϕ) that satisfy equations (2.42) and (2.43) written as the scalar wave equation[53]

$$\psi_{emn} = \cos(m\varphi) P_n^m(\cos(\theta)) z_n(kr), \tag{2.44}$$

$$\psi_{omn} = \sin(m\varphi) P_n^m(\cos(\theta)) z_n(kr), \tag{2.45}$$

where P_n^m are the Legendre polynomials of the first kind of degree n and order m, and z_n is any of the four spherical Bessel functions. The separation constants m and n are determined by subsidiary conditions that ψ must satisfy. Following Bohren and Huffmann,[53] it can then be shown that the extinction and scattering cross sections can be written as

$$\sigma_{\text{sca}} = \frac{2\pi}{k^2} \sum_{n=1}^{\infty} (2n+1)(|a_n|^2 + |b_n|^2), \tag{2.46}$$

$$\sigma_{\text{ext}} = \frac{2\pi}{k^2} \sum_{n=1}^{\infty} (2n+1)\Re[a_n + b_n], \tag{2.47}$$

where the extinction, scattering, and absorption cross-sections are related via equation (2.23). The scattering and extinction can be normalized to the geometrical cross section σ_{geo} of a particle. In the case of a sphere $\sigma_{\text{geo}} = \pi R^2$. a_n and b_n are scattering coefficients. For a nonmagnetic spherical particle

$$a_n = \frac{\tilde{m}\psi_n(\tilde{m}x)\psi_n'(x) - \psi_n(x)\psi_n'(\tilde{m}x)}{\tilde{m}\psi_n(\tilde{m}x)\xi_n'(x) - \xi_n(x)\psi_n'(\tilde{m}x)}, \tag{2.48}$$

$$b_n = \frac{\psi_n(\tilde{m}x)\psi_n'(x) - \tilde{m}\psi_n(x)\psi_n'(\tilde{m}x)}{\psi_n(\tilde{m}x)\xi_n'(x) - \tilde{m}\xi_n(x)\psi_n'(\tilde{m}x)}, \tag{2.49}$$

where $\tilde{m} = \frac{n_1}{n_2}$ is the ratio of the refractive indices of the sphere n_1 and medium n_2, and $x = kR$ is the size parameter. $\xi_n(kr) = kr \cdot h_n^{(1)}(kr)$ and $\psi_n(kr) = kr \cdot j_n^{(1)}(kr)$ are the Riccati-Bessel functions, where $j_n^{(1)}$ and $h_n^{(1)}$ are the spherical Bessel functions of the first and third kind.

As is shown in equation (2.46) and (2.47), the scattering and extinction cross-sections are a superposition of contributions coming from all m, n for which ψ is a solution. The contributions are the eigenmodes of the system, where a_n and b_n are the electric and magnetic eigenmodes, respectively.[29] For example, for a dielectric (lossless) sphere with $n = 4$ and $R = 110$ nm three electric and three magnetic eigenmodes contribute to the scattering cross-section (Figure 2.4). At the eigenfrequencies of the sphere, the normalized scattering cross-section exceeds unity, demonstrating that the subwavelength sphere can interfere with incident light across a greater cross-section than it spatially represents. This highlights the high efficiency with which subwavelength particles can manipulate light.
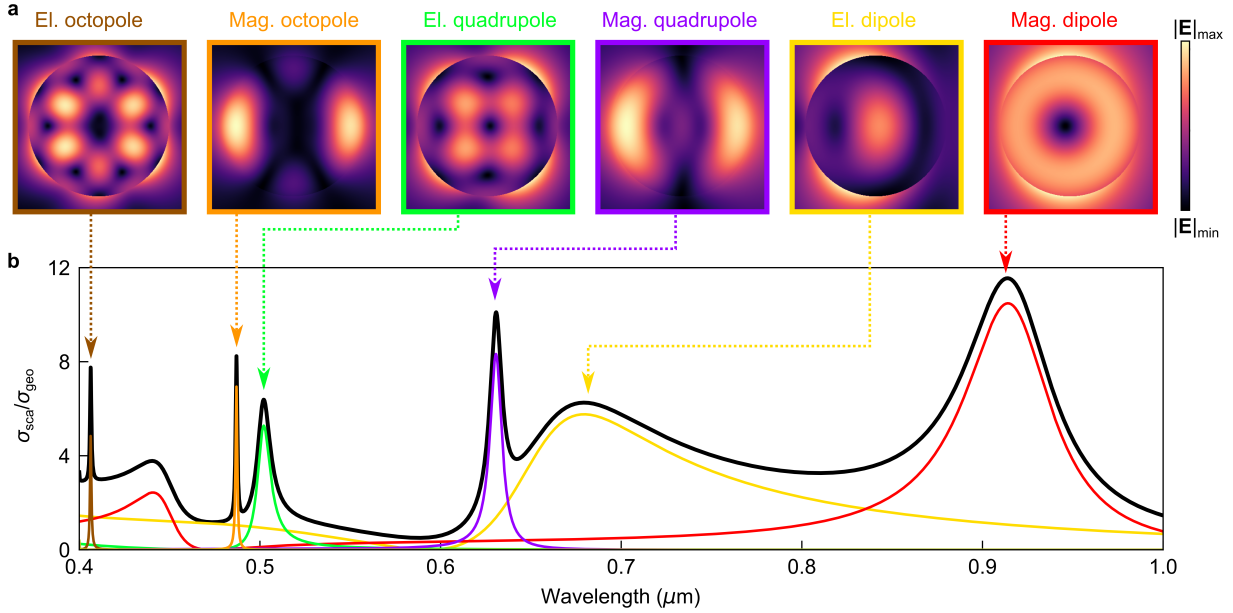
Figure 2.3. Contribution of Mie modes to the scattering cross-section of a dielectric sphere with $n = 4$ and $R = 110$ nm. (a) The electric near field patterns of the underlying electric and magnetic Mie modes up to the octopole. (b) Each of the modes (colored lines) individually contributes to the normalized scattering cross section (black line). The results were generated with the help of Ref.[78]

2.1.1   Bound States in the Continuum

The concept of bound states in the continuum was first described in the context of quantum mechanics by Wigner and von Neumann.[79] They showed that for some potentials bound states can exist as embedded eigenmodes within the continuum of propagating modes. If a quantum well is considered, states that are spatially localized within a potential well are bound and characterized by having a discrete energy. States that are outside the quantum well are delocalized and can have a continuous range of energies. BICs are spatially localized states with energies within the continuum and are a phenomenon associated with acoustics,[80] microwave physics,[81] and optics.[82,83]

In the context of optics, traditional resonances, such as Mie or plasmonic resonances, are lossy and called leaky modes. They can couple to the continuum, which means they can couple to incoming radiation and radiate into the far field (Figure 2.4). In contrast, a photonic BIC is a dark state that cannot couple to freely propagating modes. Therefore, photonic BICs cannot be excited by nor radiate into the far field (Figure 2.4). They are a mathematical concept characterized by perfect confinement in time ($\Delta v = 0$) and an infinite radiative Q factor.

22
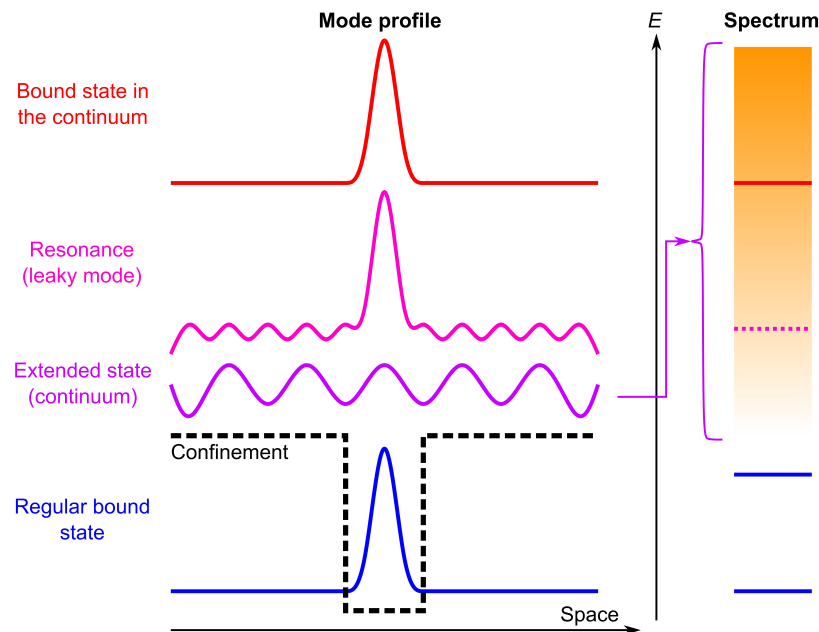
Figure 2.4. Concept of bound states in the continuum and other families of states in open photonic systems along with their position in the spectrum. Bound states are spatially localized due to a confining potential or structure (blue). Leaky modes (pink) are states with energies exceeding that of any confining potential that are spatially delocalized and can couple with extended waves. The coupling with extended waves such as incoming and outgoing radiation leads to energy being lost or leaked to the far field. BICs are spatially localized states within the continuous spectrum. They cannot couple with extended waves and therefore cannot radiate. Adapted from Ref.[84] Reproduced with permission from Springer Nature.

Radiation losses are completely suppressed by the mode's charge-current configurations that interfere destructively with incoming and outgoing propagating waves.[84] BICs can only be excited by local sources, for example via the near field by electrons. True BICs have been imaged and excited via combined cathodoluminescence and monochromated electron energy loss spectroscopy in a scanning transmission electron microscope.[85]

The analogy between photonic and quantum BICs is informative but incomplete.[86] Photonic systems have more degrees of freedom due to additional features of the system such as polarization. Four key approaches to realizing photonic BICs can be differentiated. First, symmetry-protected BICs can be realized in infinite periodic structures where coupling with normally incident or outgoing plane waves is fully suppressed.[87] A second technique for infinite periodic structures consists of accidental BICs. For certain system parameters, radiative coupling with the far field can be fully suppressed for certain non-zero angles of incidence.[88] Therefore, for infinite periodic structures, both symmetry-protected and accidental BICs are possible (Figure 2.5a-b).

Thirdly, BICs can be realized in single particles (Figure 2.5c).[89,90] The structural parameters of a subwavelength resonator can be tuned to suppress coupling to the far field via the destructive interference of the resonators' underlying photonic modes. For example, a subwavelength cylindrical resonator can be parametrically tuned to have two eigenmodes with different polarizations strongly interact with each other near the avoided crossing regime where radiative losses will be suppressed. The two eigenmodes can be a Mie and a Fabry-Perot resonance[89] or several Mie modes.[90]

Finally, BICs can be reverse engineered from an artificial potential.[29] This idea stems from the original formulation of Wigner and von Neumann.[79] A potential can be designed to support desired BICs, shown for example with the aim of generating BICs that are confined to the lattice periphery.[91,92] However, since inverse construction can yield non-physical systems the practical implementation of such systems in experimental settings is limited.

As a general principle, photonic BICs can be described by the destructive interference between multiple interacting leaky modes. For example, one class of BICs called accidental BICs can be understood by applying temporal coupled mode theory[93,94] to an open system with only two leaky modes $|\psi_s\rangle$, where $s = \{1,2\}$, with close or even equal eigenfrequencies $\Omega_s = \omega_s + i\gamma_s$ and a non-zero interaction potential $\hat{V}$ that can couple the two modes. The coupled modes then have the form $|\psi\rangle = C_1|\psi_1\rangle + C_2|\psi_2\rangle$. For certain $\hat{V}$ true photonic BICs can emerge via the complete suppression of radiative losses. In the framework of coupled mode theory, the complex amplitudes $\mathbf{a} = [a_1(t), a_2(t)]^T$ of the two states (or leaky modes) evolve in time according to

$$\frac{d\mathbf{a}}{dt} = \hat{H}\mathbf{a}, \tag{2.50}$$

$$\hat{H} = \underbrace{\begin{pmatrix} \omega_1 & \kappa \\ \kappa & \omega_2 \end{pmatrix}}_{\hat{H}_0} - i \underbrace{\begin{pmatrix} \gamma_1 & \sqrt{\gamma_1\gamma_2}e^{i\phi} \\ \sqrt{\gamma_1\gamma_2}e^{i\phi} & \gamma_2 \end{pmatrix}}_{\hat{V}}, \tag{2.51}$$

where κ accounts for the internal coupling of the modes, $\sqrt{\gamma_1\gamma_2}$ the coupling via the radiation continuum, and ϕ the phase shift between the modes. In the two-mode approximation, the BIC condition is met when one eigenvalue becomes purely real with no decay.
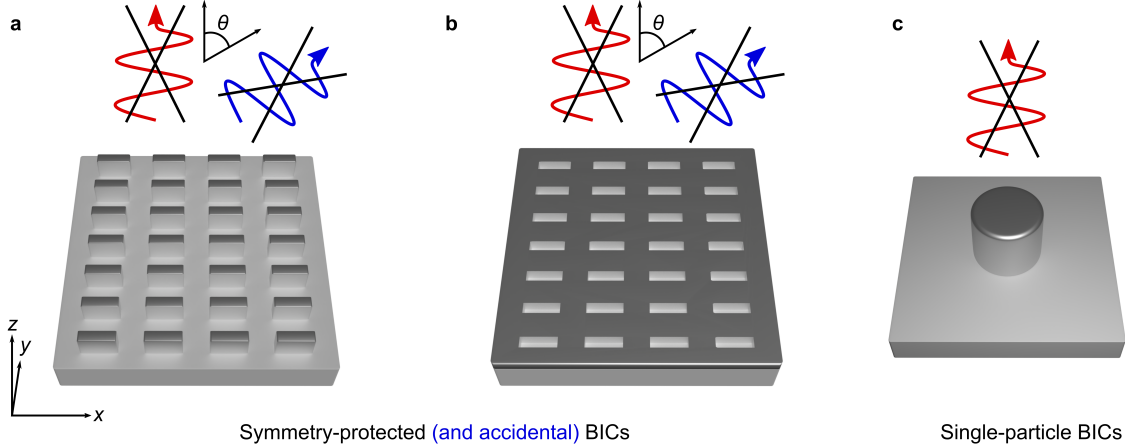
Figure 2.5. Overview of different platforms based on bound states in the continuum. The (a) positive and (b) inverse metasurfaces based on symmetry-protected BICs cannot emit radiation perpendicular to the *xy*-plane (red line). Accidental BICs can appear at different frequencies or other specially-tuned geometries, where a radiation channel at a non-zero angle of indidence is blocked (blue line). (c) BICs in single particles do not emit radiation perpendicular to the *xy*-plane (red line).

Then, the other eigenvalue becomes lossier. The BIC condition can be written as[86]

$$\kappa(\gamma_1 + \gamma_2) = e^{i\phi}\sqrt{\gamma_1\gamma_2}(\omega_1 - \omega_2), \tag{2.52}$$

$$\phi = \pi m, \tag{2.53}$$

where *m* is an integer. Conditions (2.52) and (2.53) can be met either by appropriately tuning the system parameters underlying two coupled resonances, resulting in a Friedrich-Wintgen BIC, or when $\omega_1 = \omega_2$ and $\gamma_1 = \gamma_2$, resulting in a Fabry-Perot BIC.

BICs in photonic structures can also be described via the multipole expansion method and as a topological charge.[86] The multipole expansion uses vector spherical harmonics (multipoles), an orthogonal set of solutions to the Helmholtz equation given in equation (2.42) and (2.43), to relate the polarization currents induced inside the scattering units by an incident electromagnetic wave with the directional pattern of outgoing radiation. The multipole expansion shows that BICs form when all open diffraction channels coincide directionally with the nodal lines of the unit cell field.

A simpler method of characterizing BICs is via their distinct and unique properties.[38,87] Firstly, their reflection spectra showcase a smooth profile without any distinct resonances at the BIC condition. Secondly, as the system parameters deviate from the BIC condition, a narrow resonance appears in the reflection spectra, indicating the excitation of a q-BIC with a finite Q factor. Thirdly, there must be an inverse quadratic relationship between the radiative Q factor and the BIC detuning parameter.[87] Lastly, the near-field patterns of the

q-BIC on resonance can offer further insights into the near-field cancellation mechanism, which prevents the electric near fields from radiating into the far field.[20]

The non-existence theorem predicts that no BICs can exist in either infinite periodic structures with real (lossy) materials or finite dimensional structures with $\varepsilon = \pm\infty$, $\mu = \pm\infty$, $\varepsilon = 0$ or $\mu = 0$.[84] This makes true photonic BICs a theoretical concept with experimental demonstrations being limited by the need for finite dimensions and real (lossy) materials.

Accidental and single-particle BICs are more complex, difficult to predict, and sensitive to perturbations than symmetry-protected BICs. Due to their straightforward theoretical framework and robustness towards system perturbations, we study symmetry-protected BICs in this work.

2.1.1.1 Symmetry-Protected Bound States in the Continuum

The coupling amplitude of a resonant mode due to normally incident (to xy-plane) plane waves polarized in x can be written as[87]

$$D_{j,x}(k) = -\frac{k}{2\sqrt{S_0}} \int \underbrace{E_{j,x}(\mathbf{r}')}_{\text{Mode symmetry}} [\varepsilon(k,\mathbf{r}')-1] \underbrace{e^{ikz'}}_{\text{Incidence angle}} d\mathbf{r}', \tag{2.54}$$

where k is the wavenumber, S_0 is the area of the unit cell, E_x is the electric field polarized in x, and j is the index of the resonant state. When the coupling amplitude vanishes the photonic mode cannot couple to or into the far field and the resonant mode is a BIC.

Symmetry-protected BICs are a theoretical concept satisfying the nonexistence theorem, requiring an infinite periodicity in at least one dimension or unachievable materials with a diverging permittivity and permeability.[84] Due to Noether's theorem,[95] the intrinsic translational invariance of the periodic configuration necessitates the conservation of in-plane momentum for incident light. For normally incident light, the in-plane momentum is null, referred to as the Γ point in reciprocal space. Then, light that is incident perpendicularly can solely interact with modes existing at the Γ point.

To gain further physical insights, the simple example of a grating periodic in y with period L that supports BICs can be considered.[86] The electric field can be written as a Bloch function

$$\mathbf{E}_{n,k_B}(x,y,z) = e^{ik_B z + ik_y y} \mathbf{u}_{n,k_B}(x,z), \tag{2.55}$$

where k_B is the Bloch wavenumber, k_y is the wavenumber component in y, and n is the index of the photonic band. $\mathbf{u}_{n,k_B}(x,z)$ is a periodic function that can be expanded into its Fourier series as

$$\mathbf{u}_{n,k_B}(x,z) = \sum_s \mathbf{c}_{n,s,k_B}(x)e^{i\frac{2\pi s}{L}z}, \tag{2.56}$$

with s counting the diffraction channels over which the summation runs. These channels can be open or closed. On the outside of the resonators, the expansion coefficients turn into plane waves as

$$\mathbf{c}_{n,s,k_B}(x) \rightarrow \mathbf{c}_{n,s,k_B}e^{\pm iK_s x}, \tag{2.57}$$

$$\tag{2.58}$$
$$K_s = \sqrt{\frac{\omega^2}{c^2} - k_y^2 - \left(k_B + \frac{2\pi s}{L}\right)^2}.$$

If K_s is real (imaginary) the diffraction channel is open (closed). To achieve a BIC, all coefficients $\mathbf{c}_{n,s,k_B}$ corresponding to open diffraction channels must be set to zero. However, in subwavelength structures, only one open diffraction channel exists associated with $s = 0$. $\mathbf{c}_{0,k_B}(x)$ must then be zero, where n was dropped for clarity. Since $\mathbf{c}_{0,k_B}(x)$ is the initial Fourier coefficient in the expansion given in equation (2.56), it follows that

$$\mathbf{c}_{0,k_B}(x) = \int_{-L/2}^{L/2} \mathbf{u}_{k_B}(x,z)dz. \tag{2.59}$$

For the point ($k_B = 0$) then

$$\mathbf{c}_{0,0}(x) = \int_{-L/2}^{L/2} \mathbf{u}_0(x,z)dz = \langle \mathbf{u}_0(x,z)\rangle_z. \tag{2.60}$$

When the grating's unit cell exhibits symmetry under the $z \rightarrow -z$ transformation, the eigenstates at the Γ point can assume either even or odd functions with respect to z. In the case of odd functions, their average value over z becomes zero, making these states symmetry-protected BICs. The feature of symmetry protection makes such BICs resilient to imperfect conditions such as low-contrast and high-contrast photonic structures.[96] $\mathbf{c}_{0,k_B}(x)$ can also nullify for certain system parameters instead of symmetry, where it results in an accidental or a Friedrich-Wintgen BIC.[27]

In a generalized context, $\mathbf{c}_{0,k_B}(x)$ is a complex vector. Then, the BIC condition demands both real and imaginary parts of $\mathbf{c}_{0,k_B}(x)$ to be zero. Fortunately, it can be shown that $\mathbf{c}_{0,k_B}(x)$ is real anywhere in k-space if the metasurface possesses time-reversal symmetry ($\varepsilon^*(\mathbf{r}) = \varepsilon(\mathbf{r})$), in-plane inversion symmetry ($\varepsilon(-\mathbf{r}) = \varepsilon(\mathbf{r})$), and mirror symmetry w.r.t. the sample plane. The last condition is not needed for symmetry-protected BICs making them more robust than other types of BICs. For the other BICs index matching techniques should be used to satisfy the last condition. The above treatment can be extended to resonators larger than the wavelength of light for which multiple open radiation channels can exist.

Furthermore, to generalize the symmetric aspect of symmetry-protected BICs, it can be shown that any C_{2z} symmetric infinitely periodic metasurface at the Γ point cannot couple to or into the far field owing to a symmetry mismatch between incident light and the metasurface. A resonant mode must be part of the same symmetry class as the plane wave incident on the metasurface. Since plane waves are odd under a π rotation around the normal to the periodic plane it cannot possess C_{2z} symmetry since the polarization of the plane wave is inverted under the symmetry operation.

In experimental conditions, the limited size of structures and lossy materials means that the radiative quality factors will be limited. Yet, experimental demonstration of BICs have been realized and optically mapped via electron energy loss spectroscopy.[85] With a plethora of design options for symmetry-protected BIC-based platforms,[97] the goal is to prevent coupling with the far field via symmetry considerations.

2.1.1.2   *Losses and the Quality Factor of Bound States in the Continuum*

The total Q factor of BICs is limited by losses, only the radiative Q factor Q_{rad} tends to infinity. In general, the Q factor can be decomposed[86] into its contributions (Figure 2.6) as

$$Q^{-1} = \underbrace{Q_{\text{rad}}^{-1} + Q_{\text{surf}}^{-1} + Q_{\text{str}}^{-1} + Q_{\text{size}}^{-1} + Q_{\text{subs}}^{-1}}_{\text{radiative}} + \underbrace{Q_{\text{abs}}^{-1}}_{\text{non-radiative}}, \qquad (2.61)$$

where Q_{surf}, Q_{str}, Q_{size}, Q_{subs} take into account the radiative losses due to surface roughness, structural disorder, the finite size of the sample, and a high refractive index substrate, respectively. Q_{abs} considers nonradiative losses due to all kinds of absorption, such as material absorption, free-carrier absorption, multiphoton absorption, etc. For this reason, the total Q factor of BICs cannot be infinite.

Within a metasurface's resonators, the substrate, and the environment, absorption losses occur. Structural defects and surface roughness lead to light scattering. Due to the finite size of the periodic array, edge effects occur. Light diffracts into the substrate. Specifically for BIC-driven metasurfaces, at least one channel of radiation connected to a specific angle of radiation is protected. For other angles, the radiation channels are unprotected and diffraction may occur.
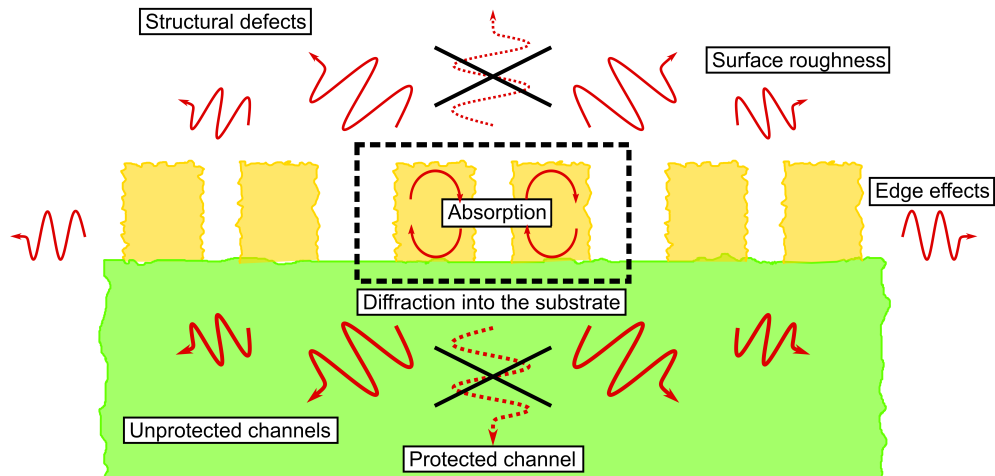
Figure 2.6. Sources of loss in metasurfaces composed of periodic arrays of finite size, with a focus on BIC-driven periodic metasurfaces. The unit cell whose loss is considered is highlighted (black dashed box).

2.1.1.3 *Symmetry Breaking and Coupling to the Continuum*

Since BICs are a mathematical concept characterized by infinite lifetimes, zero linewidths, and an infinite radiative Q factor their resonances are inaccessible in the far field making them unsuitable for applications such as sensors, filters, coherent light generation, or nonlinear enhancement, since the coupling to the far field is suppressed. By slightly perturbing or detuning a system from its BIC condition, high-Q resonances with a finite resonance lifetime and linewidth can be achieved. This detuning will open channels of radiation and allow for coupling to the far field. A straightforward method to achieve high-Q resonances is to perturb or break the symmetry of a symmetry-protected BIC metasurface. Then the coupling amplitudes given in equation (2.54) will become non-zero. The resulting leaky resonance is called a quasi-BIC or supercavity mode.

For symmetry-protected BICs, there are two fundamental ways to achieve high-Q resonances. As can be seen in equation (2.54) the coupling amplitudes can be tweaked either by manipulating the underlying electric near-field distribution of the unit cells or by detuning the angle of incidence. The symmetry of symmetry-protected BICs is only protected for normal incidence, at 90° to the periodic plane. As soon as the angle is unequal to 90°, the BIC condition is broken and a finite Q factor resonance emerges in the far field. The second option for obtaining a q-BIC resonance is to break the underlying symmetry of the metasurface. Four primary ways have been shown in the literature: breaking the in-plane inversion symmetry, the out-of-place symmetry, the permittivity symmetry, and the displacement symmetry (Figure 2.7).
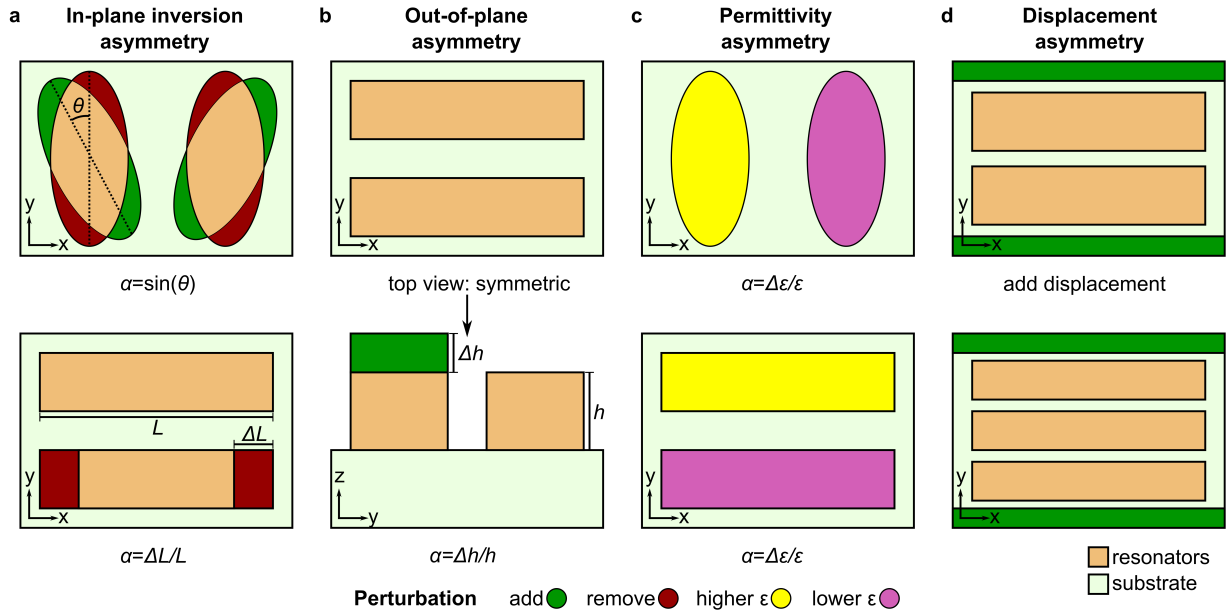
Figure 2.7. Various configurations of symmetry-breaking approaches to obtaining q-BIC resonances. (a) The in-plane inversion symmetry can be broken by adding to (dark green) and removing (red) material from the resonators (light brown) in the plane (*xy*) of parallel to the subtrate (light green). (b) The out of plane symmetry can be broken by adding or subtracting material in the *z* direction asymmetryically from one of multiple resortors in a unit cell. (c) By using different materials for different resonators in the unit cell, the permittivity contrast will lead to a q-BIC. (d) By displacing the resonators in a unit cell from those in the next unit cell asymmetrically in one direction a q-BIC can be obtained.

The most common way of achieving q-BIC resonances in the literature is by breaking the in-plane inversion symmetry.[7,45,87] There are several ways to break the in-plane inversion symmetry, by tilting two resonators w.r.t. each other, by asymmetrically removing material from one resonator w.r.t. to another and by asymmetrically removing and adding material to one or multiple resonators.[87] Recently, out-of-plane symmetry breaking has been shown to also successfully unlock q-BICs from BICs.[98] Here, one of two resonators in a unit cell was made of a different height w.r.t. one another. Furthermore, two different materials have been used to make up two resonators in a unit cell, thereby breaking the permittivity symmetry and creating a finite-Q-factor resonance from a BIC.[99] In this work, we will show that a q-BIC can be experimentally realized from a symmetry-protected BIC via displacement asymmetry breaking, whereby the in-plane inversion symmetry is maintained.[20]

An asymmetry parameter α can be defined to quantify the degree of asymmetry with which a symmetry-protected BIC can be converted into a q-BIC. α can be tuned linearly and continuously. For example, when ellipses (Figure 2.7) are tilted by an angle θ w.r.t. their unperturbed major axis, the asymmetry of the system is given as $\alpha = \sin\theta$.[7] It can

be shown[87] that the radiative quality factor follows an inverse quadratic relationship with α leading to the universal behavior for the Q factor of a q-BIC

$$Q_{\mathrm{rad}} = \frac{Q_0}{\alpha^2},$$ (2.62)

where Q_0 is a constant that needs to be determined for each metasurface. Equation (2.62) holds for q-BIC resonances if their central frequency is below the diffraction limit and is a key distinguishing feature of q-BICs.

As long as α remains small enough to be considered a perturbation, the reciprocal radiation lifetime γ_{rad} can be computed by summing up the radiation losses into all available open radiation channels. Below the diffraction limit

$$\frac{\gamma_{\mathrm{rad}}}{c} = |D_x|^2 + |D_y|^2,$$ (2.63)

$$D_{x,y} = -\frac{k_0}{\sqrt{2S_0}} \left(p_{x,y} \mp \frac{1}{c} m_{y,x} + \frac{ik_0}{6} Q_{xz,yz} \right),$$ (2.64)

where **p**, **m**, and $\widehat{\mathbf{Q}}$ are the normalized electric dipole, magnetic dipole, and electric quadrupole moments per unit cell. From equations (2.63) and (2.64) it can be seen that for a true BIC $\gamma_{\mathrm{rad}} = 0$ since the electric field components are odd under the inversion of coordinates $(x, y) \rightarrow (-x, -y)$.

Another interesting aspect of q-BIC is the gradual increase in modulation with increasing α up to a maximum modulation followed by a decrease with further decreasing α. Interestingly, the modulation in transmission ΔT or reflection ΔR is intrinsically connected to the Fano formula, elucidating that a BIC collapses to a Fano resonance when $\alpha \neq 0$. The transmission T at the q-BIC resonance can be calculated by taking into account both ΔT and the background contribution. It can be shown[87] that

$$T(\omega) = \frac{T_0}{1 + q^2} \frac{(q + \Omega)^2}{1 + \Omega^2} + T_{\mathrm{bg}},$$ (2.65)

where q is the Fano asymmetry parameter, $\Omega = 2(\omega - \omega_0)/\gamma$ is a dimensionless frequency, and T_{bg} and T_0 represent the inherent background contribution of non-resonant modes to the amplitude of the resonant peak and the offset, respectively. Interestingly, at the BIC condition q in equation (*2.65*) becomes ill-defined linked to a collapse of the Fano resonance.

2.2   Angular Dispersion in Metasurfaces

The angular dispersion of photonic resonances has been studied only in a few studies,[48,49] where two primary factors have been found to control it: the near-field coupling between neighboring unit cells and the radiation pattern of a single unit cell. Together, both factors can explain the behavior of resonances when the angle of incidence is changed. The theory outlined here applies to any dispersive (or non-dispersive) materials and constitutes a general and systematic approach to controlling angular dispersions. The theory was experimentally and numerically validated from the NIR to the low-frequency THz spectral range on metallic metasurfaces.

2.2.1   Frequency Shifts Driven by Changes in the Angle of Incidence

With the advent of a general tight-binding model for dispersive and non-dispersive photonic systems in few-resonator [100] and then in periodic systems,[49] their angular dispersion could be described via the near-field coupling between neighboring unit cells. We will focus on two-dimensional periodic metasurfaces since they were studied in this work. It can be shown that the interaction of a unit cell with any other can be described via their coupling strength t as

$$t_{\{m,n\}}^{\{k,l\}} = -f_0 \frac{\int \mathbf{P}_{\{m,n\}}^*(\mathbf{r}) \cdot \mathbf{E}_{\{k,l\}}(\mathbf{r}) d\tau}{\langle \Phi_s | \Phi_s \rangle}, \tag{2.66}$$

where $\mathbf{P}_{\{m,n\}}(\mathbf{r})$ describes the polarization field inside each unit cell with lattice site location $\mathbf{R}_{\{m,n\}}$, $\mathbf{E}_{\{k,l\}}(\mathbf{r})$ describes the electric field distribution at the lattice site location $\mathbf{R}_{\{k,l\}}$, and $\langle \Phi_s | \Phi_s \rangle$ normalizes the coupling strength to the total energy stored inside a single unit cell.

In periodic metasurfaces, the interaction between the unit cells is described via equation (2.66) and leads to collective modes. These modes can be labeled via a Bloch wavevector $\mathbf{k}$. The eigenfrequency of such a collective mode is given by[49]

$$f_r(\mathbf{k}) = f_0 + \sum_{\{m,n\}} t_{\{0,0\}}^{\{m,n\}} \cos\left[\mathbf{k} \cdot \left(\mathbf{R}_{\{m,n\}} - \mathbf{R}_{\{0,0\}}\right)\right], \tag{2.67}$$

where $\mathbf{R}_{\{0,0\}}$ is the site location of the studied reference unit cell with the summation running over all neighboring unit cells.

The coupling strength decreases with increasing distance between two unit cells, which is why the summation has to be truncated in periodic structures. The truncation depends on the Q factor of the metasurface at normal incidence. Since the Q factor quantifies the light confinement within each unit cell in periodic arrays, a higher Q factor means that

light is better confined within each unit cell and the coupling strength to neighboring unit cells decreases. Then, the summation can be truncated with fewer neighboring unit cells being considered. Studies on low-Q factor systems have shown that a five-by-five square of unit cells around a reference unit cell leads to converging results with numerical models and experiments.

For incident light to interact with a metasurface, the wavevector of the incident radiation must match that of the underlying resonance of the system. This means that the collective mode of a periodic system must have a matched in-plane **k** to the wavevector of incident light. At an angle of incidence θ the Bloch wavevector is given by

$$\mathbf{k} = \hat{x} k_0 \sin\theta, \tag{2.68}$$

where k_0 is the free space wavevector at normal incidence. By inserting equation (2.68) into equation (2.67) the frequency shift of a resonance can be predicted depending on the angle of incidence. In a simplified form and truncated at the first three terms in the summation the angular shift of the central frequency of a resonance can then be written as

$$f_r(\theta) = f_0 + J_0 + J_1 \cos(P k_0 \sin\theta) + J_2 \cos(2 P k_0 \sin\theta) + \cdots, \tag{2.69}$$

where P is a unit cell length and $\{J_i\}, i \in \mathbb{N}_0$ describe the near-field coupling between neighboring unit cells. $J_0, J_1,$ and J_2 quantify the effective near-field coupling within a unit cell row, between two nearest-neighbor rows, and between two next-nearest-neighbor rows, respectively. These constants can be calculated via the tight-binding model when the electromagnetic near fields are known. $\{J_i\}$ are given by

$$J_0 = \sum_{i=-2}^{2} t_{\{0,0\}}^{\{i,0\}}, \quad J_1 = 2 \sum_{i=-2}^{2} t_{\{0,0\}}^{\{i,1\}}, \quad J_2 = 2 \sum_{i=-2}^{2} t_{\{0,0\}}^{\{i,2\}}, \tag{2.70}$$

where the summations were truncated for a five-by-five square around a reference unit cell. Since J_0 is angle insensitive, only $\{J_i\}, i \in \mathbb{N}$ shift the central frequency of the resonance. If J_1 and J_2 are negative, the resonance will blueshift with increasing θ. Between J_1 and J_2, J_1 is the dominating term since the coupling between nearest-neighbor rows is stronger compared to next-nearest-neighbor rows, as the distance between them is smaller. Experimentally, it has been found that J_1 is roughly one order of magnitude larger than J_2.[49] Within J_1, $t_{\{0,0\}}^{\{0,1\}}$ is the dominating term.

For some metasurfaces, opposing shifts in the central frequency have been shown between s (ϕ = 0°) and p (ϕ = 90°) polarized light. This phenomenon is attributed to a crossing of J_1 and J_2 from negative to positive values at a certain ϕ between 0° and 90°.

2.2.2 Angle Dependence of the Optical Line Shape

The change in the optical line shape with changes in the angle of incidence depends on the radiation pattern of a single unit cell.[48] Using temporal coupled-mode theory[93] and a one-port single-mode model, the reflectance R can be derived and is given by[48]

$$R = \frac{2\gamma_{\text{rad}}}{-i2\pi(f - f_r) + \gamma_{\text{int}} + \gamma_{\text{rad}}} - 1, \tag{2.71}$$

where γ_{int} and γ_{rad} are the intrinsic and radiative damping rates. The angle dependence of f_r is given in equation (2.69). The intrinsic damping rate is relatively insensitive to changes in the angle of incidence, which should be expected since, in a first approximation, losses due to material absorption should be angle-independent. Therefore, we can write

$$\gamma_{\text{int}}(\theta) \approx \gamma_{\text{int}}(0). \tag{2.72}$$

The radiative damping rate is weakly dependent on the angle of incidence. This feature explains why a perfect absorption condition at normal incidence can stay near-perfectly absorbing when the angle of incidence is changed.[48] However, this depends strongly on the radiation property of a single unit cell.

For example, a metasurface supporting a magnetic mode polarized along the *y* direction that radiates almost uniformly and equally into all directions of the *xz*-plane features almost angular-independent radiative damping under *p* polarized light. This is because the coupling between the magnetic field vector and magnetic mode of the metasurface is almost angle-independent, so its radiative damping should be as well. If for the same structure *s* polarized light is used, the resonance is found to behave very differently compared to the *p* polarized case. The magnetic dipole is then on the *xz*-plane and the radiation power is proportional to $\cos^2\theta$. Then, the radiative damping constant decreases as *θ* increases. Consequently, the coupling condition changes, which changes the resonance bandwidth and peak absorption.

2.3 Surface Enhanced Infrared Absorption Spectroscopy

SEIRAS detects IR active vibrational modes of molecules. For a mode to be IR active, there must be a change in a molecule's dipole moment as a result of the vibration that occurs when IR radiation is absorbed.[101] Light is absorbed by molecules when the energy of the photons matches the energy of the vibrational modes. SEIRAS is a derivative technique of conventional infrared spectroscopy based on the enhancement of the local electromagnetic near fields.[102,103] To further enhance the electromagnetic near fields, SEIRAS has been paired with plasmonics to improve biosensing. Plasmonic-based sensors have become the method of choice in the label-free detection of biomolecules.

They can be used either as 1) refractive index sensors or 2) by coupling the resonances to the molecular modes and analysing the perturbation of the intensity either in reflection or transmission,[104] termed perturbed intensity sensing here.

There are a few important considerations that need to be made for SEIRAS. First, the environment needs to be chosen and adjustments have to be made depending on how strongly it absorbs. As IR characterization techniques suffer from high losses in aqueous environments, two geometries are typically used to acquire IR spectra of molecules suspended in analyte or adsorbed on resonator surfaces, namely the external reflectance approach or measuring in an attenuated total internal reflectance geometry. Next, if a plasmonic underlying platform is used instead of a roughened metallic film with random electric near-field enhancement, then the absorption enhancement between the vibrational modes of the molecules and the resonator modes have to be engineered carefully by tuning the coupling constants appropriately. Finally, if the molecules adsorb on the metallic film or resonators, the surface selection rule needs to be considered. These concepts will be discussed in the following sections.

2.3.1 Geometries to Improve Signal-to-Noise Ratios in Lossy Environments

First, the external reflectance approach consists of squeezing a thin layer of electrolyte between the working electrode and a prism to reduce optical losses.[105,106] The advantage of the external reflectance approach is a high degree of freedom in choosing the morphology and thickness of the studied material. However, although the lossy analyte layer is thin, it still suffers from dampened signals due to the resulting light absorption.

A second geometry used to decrease optical losses from the electrolyte is to operate a sensing platform in an ATR configuration.[105–107] As light is totally reflected on a surface, evanescent waves with an exponential decay probe the other side of the reflective surface. Due to the evanescent approach, the losses stemming from the lossy environment are minimized. Additionally, the higher reflection also ensures enough signal is received by the detector, which improves the signal-to-noise ratio.

2.3.2 Engineering Absorption Enhancement in Coupled Molecular-Plasmonic Resonator Systems

The interaction between resonators in a sensing platform and the vibrational modes of a molecule can be described as a system of a damped harmonic oscillators consisting of a coupled bright and dark mode. The bright mode (resonator) is driven by external radiation and damped at a given rate. The bright mode has two loss channels, one due to externally radiation γ_{ext} and one due to intrinsic material absorption γ_{int}. Moreover, the external driving rate of the bright mode is interdependent with γ_{ext} because of time reversal

symmetry and energy conservation.[42] In other words, the rate of driving the system should correspond to the rate of the reverse process. The dark mode (molecule) does not interact with the driving field but dampens the system by its intrinsic coupling to the bright mode. Since the bright mode has more loss channels, its overall damping rate is higher.

To maximize SEIRAS performance an impedance matching procedure should be performed, corresponding to tuning the system parameters towards reaching critical coupling. Critical coupling is when $\gamma_{ext}/\gamma_{int} = 1$. To understand the effects of under $(\gamma_{ext}/\gamma_{int} < 1)$, over $(\gamma_{ext}/\gamma_{int} > 1)$, and critically coupled oscillator systems, the absorption cross-section (σ_{abs}) of a silver prolate spheroid can be evaluated using analytical quasi-static approximations with the radiation damping correction and compared before and after being coated with a dielectric shell featuring an absorption line (Figure 2.8a-b).[42] As it turns out, the particle-cross section is related to the damping rates via

$$\frac{\sigma_{sca}}{\sigma_{abs}} = \frac{\gamma_{ext}}{\gamma_{int}}, \tag{2.73}$$

where σ_{sca} is the scattering cross-section. The interdependent relationship between the absorption and scattering cross-sections can be seen in Figure 2.8c in connection with Figure 2.8a.

For SEIRAS the absorption of a dark mode or absorber coupled to a bright oscillator has to be maximized for ideal performance. Valuable insights can be gained by considering a simpler coupled oscillator system by using temporal coupled-mode theory, namely with only one bright mode interacting with incident light. In this work, the SEIRAS measurements were made in ATR mode collecting only the reflectance R. Then, the system can be treated as a one-port system with an input and output channel. In this case, the absorption Abs. is given by[42]

$$\text{Abs.} = 1 - R = \frac{4\gamma_{rad}\gamma_{int}}{(\omega - \omega_0)^2 + (\gamma_{rad} + \gamma_{int})^2}, \tag{2.74}$$

where ω and ω_0 are the frequency and central frequency when the bright mode is driven on resonance, respectively. On resonance ($\omega = \omega_0$), equation (2.74) transforms to

$$\text{Abs.} = \frac{4f}{(1+f)^2}, \tag{2.75}$$

with $f = \gamma_{ext}/\gamma_{int}$. As can be easily seen, the absorption maximizes to 1 at the critical coupling condition.
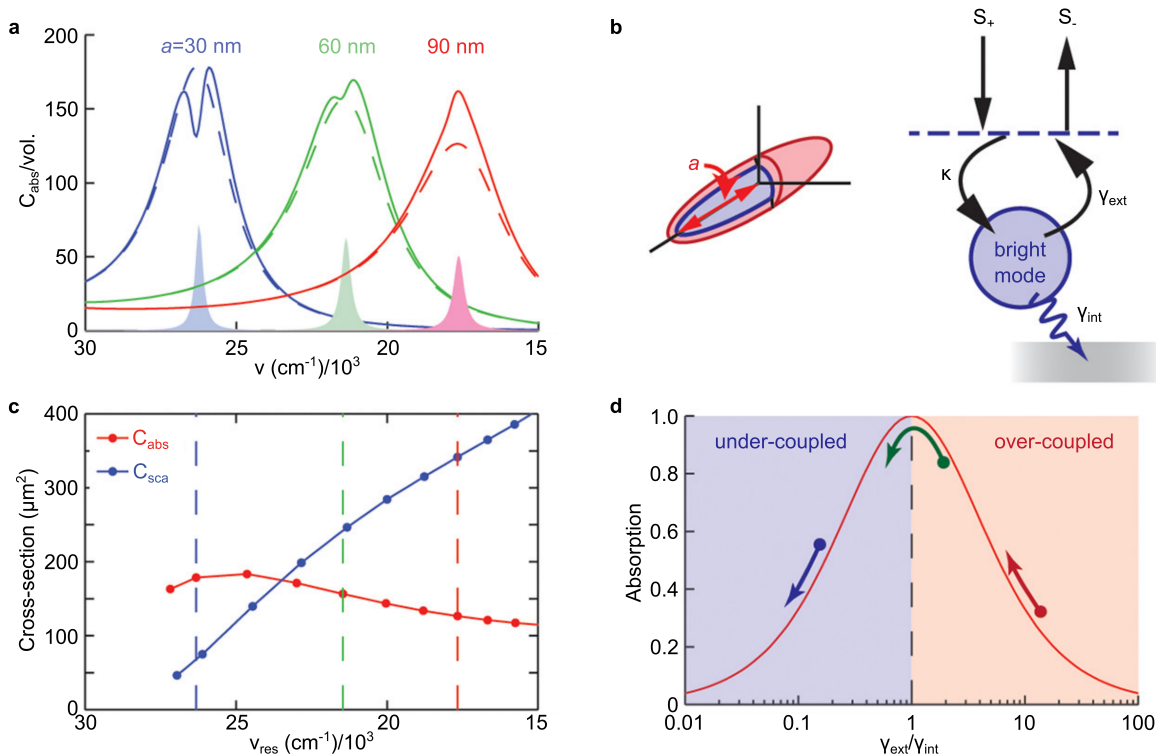
Figure 2.8. Under, over, and critical coupling. (a) The absorption cross sections normalized to the particle volume with (solid line) and without (dashed line) a model material that absorbs at the center frequency of each resonance for three semiaxis lengths *a* of Ag prolate spheroidal particles. (b) Schematic of the system composed of Ag particles enveloped in a 5 nm thick shell of absorbing material and its generalized cavity model, excluding the presence of the absorber. (c) Cross-sections for absorption and scattering on resonance. (d) The peak absorption for the generalized cavity as a function of the ratio of external to intrinsic damping rates. The colored arrows highlight relevant movements along the curve for the three distinct ellipsoids in (a). Adapted with permission from Ref.[42] Copyright 2013 American Chemical Society.

However, as is the case in SEIRAS, in addition to the bright mode interacting with incident light, a dark mode interacts with the bright mode. We can neglect the interaction between the additional mode with incident light due to the usually very small absorption cross-sections of molecular vibrational modes. The added mode leads to increased damping of the bright mode, which corresponds to a leftward move along the graph in Figure 2.8d. The magnitude of the leftward move depends on the damping strength of the dark mode. When the system is slightly overcoupled, the presence of the dark mode will drive the system towards the critical coupling condition. If the system is slightly undercoupled, the dark mode will make the system even more undercoupled.

Note that in Figure 2.8a, the central resonance shows only a small perturbation of the resonance associated with the bright mode. Although the bright mode is near the critical

coupling condition, the presence of the dark mode corresponds to the coupling condition shifting along the curve in Figure 2.8d from one side of the peak to the other side. The absorption is not significantly altered and the perturbation of the bright modes resonance profile is not strongly affected. In contrast, the other two resonances are perturbed more strongly. For the overcoupled system, the path change corresponds to a push towards the critical coupling condition towards extraordinary optical absorption. For the undercoupled system to a push towards extraordinary optical transmission.

For SEIRAS that means that the bright mode should ideally be tuned close to the critical coupling condition, if it were alone, tendentially closer to being undercoupled than overcoupled. The dark mode then perturbs the resonance towards extraordinary optical transmission causing a strong modulation in reflection or absorption. Ideally, the change in the coupling constants corresponds to a leftward push away from the peak. The push should not go through the peak. The bright mode can alternatively be engineered to be overcoupled enough that the system moves towards extraordinary optical transmission.

Along with the impedance matching procedure described above, the electric near-field enhancement plays a crucial role in amplifying the signals of the dark mode. The enhancement of the dark mode signals is tangentially limited from below by the electric near-field intensity enhancement factor $|E/E_0|^2$, where E is the maximum electric near-field strength near the resonators and E_0 is the maximum incident electric field strength. In reality, however, the real enhancement of the dark mode's signals is significantly lower. This is due to a much lower average electric near-field intensity enhancement experienced by the dark mode due to imperfect coupling between the dark mode and the bright mode, imperfections in fabrication, adhesion layers not considered in simulations,[108] etc. The average electric near-field intensity enhancement experienced by the dark mode can be improved by choosing resonators with high $|E/E_0|^2$ or with linearly instead of exponentially decaying electric near-fields from its resonator surface as is the case for plasmonic slots.[52] The resonance strength and therefore near-field enhancement can be increased by choosing thin metallic adhesion layers instead of thick ones or molecular linkers.[108]

Finally, as explained in section 2.1.4.5, the resonance should always be tuned on the low-frequency side of the RA to ensure the resonance is in an environment dominated by evanescent decay as opposed to radiative decay. The resulting higher Q factors and electromagnetic near-field enhancements strongly improve the sensing performance.

2.3.3   Band Selection Rule in IR Spectra of Adsorbed Species

Another important consideration needs to be taken into account when designing a SEIRAS system employed to characterize molecules adsorbed on a metal film. As the (IR-active) molecules adsorb on the film, their orientation is fixed leading to a fixed electric dipole. The band selection rule dictates that the IR signals extracted from molecules

depend on the alignment of the average molecular dipole with the electric near-field vector orientation.[109] The best signals will be extracted when the electric near-field vector aligns well with the electric dipole of the adsorbed molecules. Then, the electric near field can best interact with the dipole and the most energy can be absorbed into the molecular vibration. When the electric near field vector is normal to the molecular dipole, then no interaction between the two exists and the adsorbed molecules cannot be detected.

A consequence of conventional ATR-SERIAS consisting of an unstructured metallic film on a transparent substrate employed to detect adsorbed molecules with a dipole-oriented perpendicular to the metallic film is that only *p* polarized light can interact with the adsorbed molecules. Since *s* polarized light has its electric field vector oriented parallel to the metallic surface, its electric field vector is oriented normally to the molecular dipole.

When more complex resonator geometries are chosen to amplify the SEIRAS signals, the active surfaces of the resonators should be investigated before choosing a certain geometry. The active surfaces support the band selection rule for a certain polarization and angle of incidence. Maximizing the active surfaces and the alignment between the dipoles of the adsorbed molecules and the incident light will contribute to optimizing the SEIRAS signals.

2.4   Electrochemistry

Electrochemistry is a branch of chemistry that studies the relationship between chemical processes and the flow of electrons.[56] Typically, the interaction between chemical substances in a confined system is studied with respect to changes in the measured electric currents as a potential is externally controlled. The systems are confined in electrochemical cells consisting of a working electrode interacting with the substances, a counter electrode, and a reference electrode, usually solid conductive materials immersed in an electrolyte solution. Electrochemistry explores various phenomena, including reduction-oxidation (redox) reactions, electrode kinetics, ion transport, and the generation of electrical energy via chemical reactions or vice versa. In this work, the two half-reactions of the CO_2 redox reaction are investigated. Oxidation means the loss of electrons and reduction means the acquisition of electrons.

2.4.1   Electrolytic and Voltaic Cells

As the potential inside an electrochemical cell is changed, chemical energy is converted to electrical energy and vice versa. If the cell releases energy during the reaction, it is called galvanic or voltaic. Voltaic cells use spontaneous reactions to extract electrical

energy from a system. An example of a voltaic cell are batteries. If an electrochemical cell requires an external electrical energy source to drive a non-spontaneous chemical reaction, it is known as an electrolytic cell. Electrical energy is then introduced into the system to facilitate processes that would not occur spontaneously. Electrolysis can be used to separate substances into their original constituents. It can be also used to form constituents that are not thermodynamically favorable. An electric current is introduced into the electrochemical cell via the application of an external potential. When the potential reaches a certain threshold to overcome the activation energy of a given reaction, the current is strong enough to run a non-spontaneous reaction that, for example, separates the substances that were chemically bound together.

2.4.2   Connection between Cell Potential and Gibbs Free Energy

The total energy available to carry out electrical work is contingent upon both the cell potential and the number of electrons transferred from the reducing to the oxidizing substance during a reaction. The total charge that is transferred during a redox reaction from a reductant to the oxidant is nF, where n is the number of moles of electrons and F is one faraday, the charge of one mole of electrons.

The maximum amount of work that can be done by an electrochemical cell w_{max} corresponds to the change in the Gibbs free energy ΔG. An electrochemical cell with a positive potential will do work on the system, then $w_{max} < 0$. The potential of an electrochemical cell E_{cell} and the change in the free energy is

$$\Delta G = -nFE_{cell}. \tag{2.76}$$

When a redox reaction occurs naturally, it generates a voltage itself and is called spontaneous. If a voltage is necessary to perform the reaction, it is called nonspontaneous. A spontaneous reaction is exergonic meaning it releases energy. Therefore, ΔG is negative and E_{cell} is positive for spontaneous reactions.

The standard conditions for redox reactions are room temperature (298.15 K), pressure at 1 atm (101.325 kPa), and a solution concentration of 1 mol.dm^{-3} (1 M). As redox reactions can be split into their half-reactions, the voltage of each half-reaction can be measured and is given w.r.t. to its reduction reaction. This is then called the reduction potential. The standard reduction potential E^o_{cell} is given relative to the potential of the hydrogen reduction potential, which is set at zero as a baseline, and at standard conditions. When reactants and products are in their standard states, the potential of the cell is not pH-dependent and the Gibbs free energy difference is

$$\Delta G^o = -nFE^o_{cell}. \tag{2.77}$$

Adding together the ΔG values for the half-reactions gives ΔG for the overall reaction, which is proportional to both the potential and the number of electrons transferred.

Summing up the ΔG values of the half-reactions results in the complete reaction's ΔG, a quantity that is proportional to both the potential and the number of electrons exchanged during the reaction. When $\Delta G = 0$, the reaction is at equilibrium.

2.4.3 The Nernst Equation

Above, we discussed how the reduction potential of a redox reaction at standard conditions can be found. At non-standard conditions, we can calculate the reduction potential using the Nernst equation, derived by Walther Nernst in 1889,[110] given by

$$E_{\text{cell}} = E_{\text{cell}}^o - \left(\frac{RT}{nF}\right) \ln Q, \tag{2.78}$$

where R is the ideal gas constant, T is temperature, and Q is the reaction quotient. Q gives the relative amounts of products and reactants as a ratio. Q may change during a reaction. At equilibrium, $E_{\text{cell}} = \Delta G = 0$ and $Q = K$, where K is the equilibrium constant, the reaction quotient at chemical equilibrium. Equation (2.78) then becomes

$$E_{\text{cell}}^o = \left(\frac{RT}{nF}\right) K. \tag{2.79}$$

The Nernst equation at room temperature ($T = 298$ K) can be written as

$$E_{\text{cell}} = E_{\text{cell}}^o - \left(\frac{0.0591\ V}{n}\right) \log Q, \tag{2.80}$$

where the natural logarithm was converted to a base-10 logarithm, and V is the unit of the potential.

2.4.4 Faraday's Laws of Electrolysis

Faraday's laws of electrolysis, established in 1833 by Michael Faraday,[111] link the amount of substance produced or consumed during electrolysis to the electric charge flowing through the electrochemical cell. The first of two laws states that the mass of elements deposited at an electrode is proportional to the charge passing through the cell. The second law states that the quantities of chemical transformations induced by a certain amount of electricity in distinct substances are proportional to their equivalent weights.

2.4.5 Strategies for CO_2 Recycling

Along with carbonate minerals, CO_2 is the most oxidized form of carbon. It has a formal oxidation state of +4. CO_2 can be converted into a more energetic product by the transfer of its electrons to carbon, thereby effectively reducing its oxidation state in the process. When CO_2 is converted to a more reduced product, the reaction is called CO_2 reduction. If these reactions are thermally driven, they are called CO_2 hydrogenation. If they are based on photosynthesis or bioinspired catalysis they are called CO_2 fixation.[112]

To obtain a closed cycle, the source of electrons and protons for the CO_2 reduction should be water as the combustion of hydrogenated carbon products release water. The overall formula followed by CO_2 reduction/hydrogenation/fixation is therefore

$$x CO_2 + y H_2O \rightarrow \text{product} + z O_2, \tag{2.81}$$
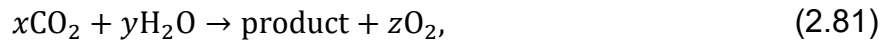
where x, y, and z are integers to balance out the equation.

A thermally activated pathway for CO_2 hydrogenation is the reverse water gas shift reaction to reduce CO_2 to CO by

$$CO_2 + H_2 \rightarrow CO + H_2O. \tag{2.82}$$

Using this reaction and using excess H_2, the H_2 and CO gas mixtures can be used as precursors to methane on a Ni catalyst,[113] to multi-carbon hydrocarbons on a Fe or Co catalyst,[114] or to methanol on a Cu/ZnO catalyst.[115] The variety of different reaction pathways shows the underlying complexity of CO_2 reduction. The three aforementioned reaction pathways require high pressures and temperatures. For instance, for the synthesis of methanol, approximately 100 bar and 250 °C are needed.[116]

For CO_2 hydrogenation to be green, the needed hydrogen should come from water-electrolysis

$$2 H_2O \rightarrow O_2 + 2 H_2. \tag{2.83}$$

The two half-reactions making up the water-electrolysis reactions are the hydrogen evolution reaction at the cathode

$$2 H^+ + 2 e^- \rightarrow H_2 \tag{2.84}$$

and the oxygen evolution reaction at the anode

$$2 H_2O \rightarrow O_2 + 4 H^+ + 4 e^-. \tag{2.85}$$
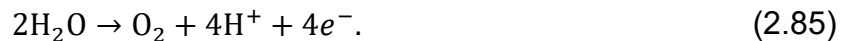
2.4.6 Electrochemical CO_2 Reduction

The electrochemical CO_2 reaction at the cathode takes the general form

$$xCO_2 + nH^+ + ne^- \rightarrow \text{product} + yH_2O, \tag{2.86}$$
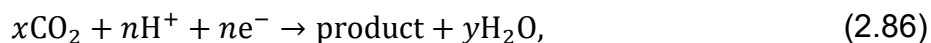
which is balanced by the oxygen evolution reaction given in equation (2.85). In particular, as outlined in the introduction, the electrochemical CO_2RR to CO is given by a simple two-electron transfer given in equation (1.2), which is also balanced by the oxygen evolution reaction given in equation (2.85). The electrochemical CO_2 reduction to CO is one of the most promising options to close the carbon cycle due to its scalability, cost-competitiveness, and sizeable market share.[50]

2.4.7 Intermediates and Product Selectivity in Electrochemical Reactions

The emphasis of electrocatalysis was initially placed on the reaction rate and required overpotentials.[117] Recently, the focus gradually moved towards improving the selectivity of reactions. For the primary electrochemical reactions of interest, namely the hydrogen evolution reaction and the CO_2RR, multiple pathways can be used at different rates and efficiencies depending on factors such as environment, temperature, pressure, catalyst material, and more. On top of that, the products can continue to react to create new products at different efficiencies and in different pathways leading to a complex underlying chemical framework that needs to be understood to optimize reactions towards a given goal. Important to note is that during reactions intermediate species form that do not exist in the final product. Intermediates are transient species in a multi-step reaction mechanism. They are produced and consumed to ultimately create the final product. Reaction intermediates play a significant avenue in manipulating the reaction selectivity since they are complex yet necessary for achieving the final product.

Parameters that have been shown to influence the product selectivity and therefore the underlying formation of intermediates have been shown via changes in the pH near the catalyst's surface, the electrolyte composition, temperature, pressure, and the catalyst material.[118] The pH determines the number of protons available in the electrolyte solution. pH plays a crucial role in reaction selectivity, influencing the availability of protons for reactions like CO_2 reduction.

pH-induced surface charge changes impact the adsorption behavior of intermediates.[119] Electrolyte composition affects ion concentration near the electrode surface, influencing surface charge distribution, intermediate stability, and reactivity, leading to diverse product outcomes.[120] Pressure influences reaction rates and coverage of catalyst surface adsorbates, affecting selectivity in reaction pathways. Temperature influences reaction kinetics, activation energy, and thermodynamic favorability of pathways.[121] Catalysts modify activation energy and adsorption preferences, leading to favored reaction pathways. Surface poisoning can alter selectivity by hindering certain pathways. Catalysts also alter reaction rates, potentially favoring specific pathways.

To study the effects of changes in pH, electrolyte composition, temperature, pressure, and catalyst material, the interaction between the catalyst and reaction intermediates need to be studied. Since these occur at the interface between the catalyst and the electrolyte, surface-enhanced optical spectroscopic techniques like SERIAS or surface-enhanced Raman spectroscopy are convenient tools for studying these interactions. By using these surface-sensitive and surface-selective techniques, the effects of choosing different electrolytes, catalysts, temperatures, pressures, etc. can be studied.

2.4.7.1 *Product Selectivity in Electrochemical CO_2 Reduction*

CO_2 reduction can lead to the production of several C_1 products such as CO, HCOOH, CH_3OH, etc. before its complete $8e^-/8H^+$ reduction to CH_4.[117] More C_2 and C_3 products can also be generated in what leads to complex reaction pathways including various intermediates (Figure 2.9). The hydrogen evolution reaction competes with the CO_2RR, as the low-valent electron-rich metal catalysts are prone to reduce to protons. Similarly, low-valent metal catalysts are prone to oxidation by atmospheric O_2, causing the oxygen reduction reaction and requiring anaerobic conditions for the CO_2RR. Another consequence of the selectivity of the CO_2RR is that, if the information about O_2 is neglected and O_2 is involved in the reaction, it leads to the release of partially reduced O_2 species such as O_2^-, H_2O_2, etc. These species are reactive and result in oxidative degradation of the catalyst.

Depending on the type of catalyst used during electrochemical reactions in general, and the electrochemical CO_2RR in particular, the reaction pathways and therefore selectivity process will be altered.[118] In a comparison between Au, Cu, and Pt, Au produces adsorbed CO and H_2. Cu can produce a variety of products including CO, formate, methane, and ethylene during the CO_2RR, where a variety of O-bound and C-bound intermediates occur on Cu's surface. Pt favors the competing hydrogen evolution reaction, as the stability of Pt leads to adsorbed CO formation, which poisons the surface. In the case of Pt, its surface becomes covered in a stable layer of adsorbed CO. The adsorbed CO layer prevents other reaction intermediates from interacting with the catalyst surface, thereby effectively preventing the catalyst from performing the CO_2RR.
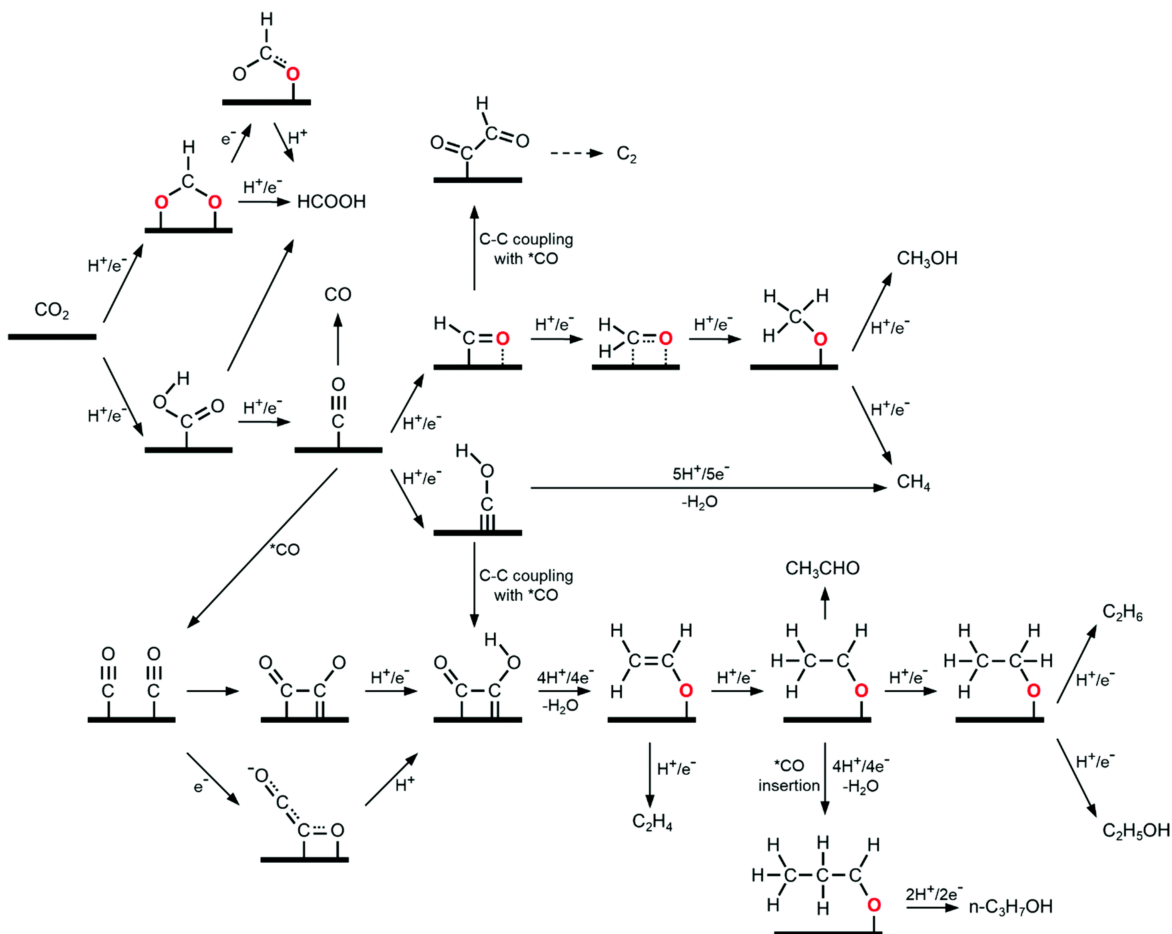
Figure 2.9. Schematic of the reaction pathways of the CO_2RR to various C_1-C_3 products. O-bound catalyst binding is shown in red. Dashed arrows show consecutive proton/electron transfer steps toward different C_2 products. Reprinted from Ref.[122] with permission from The Royal Society of Chemistry.

2.4.1   SEIRAS for Electrochemical CO₂ Reduction

Due to complex reaction pathways, a low IR signal intensity, and an aim to improve and increase the understanding of the selectivity process of the CO_2RR, improved monitoring platforms need to be developed. Conventionally, however, the electrodes used electrochemical surface roughening techniques that were highly unreproducible providing only a random signal-enhancing effect.[118] Studying reaction pathways and intermediates using electrochemically roughened metal/catalyst surfaces means careful adjustment of the reaction parameters, such as pH, electrolyte composition, temperature, pressure, and catalyst material, to yield a desired and predictable outcome. This is difficult, especially when the outcome is unknown and the vibrational bands of adsorbed species are weak.
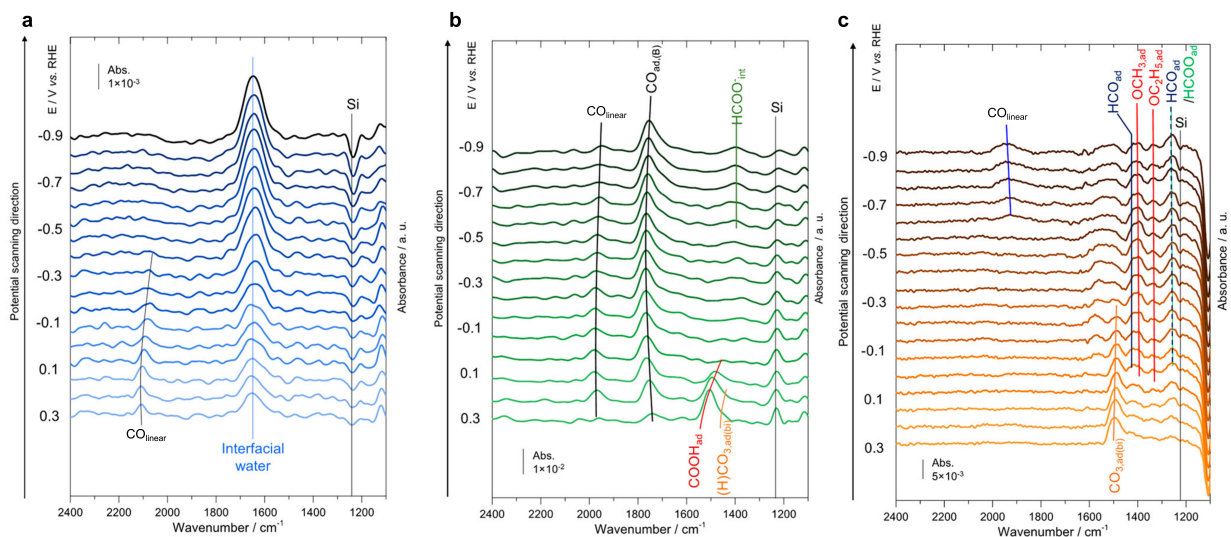
Figure 2.10. In situ ATR-SEIRAS spectra obtained during linear sweep voltammetry in a potential window from 0.3 V_{RHE} to −0.9 V_{RHE} in 1 M KHCO$_3$ (pH 6.8) on a (a) Au, (b) Pt, and (c) Cu electrode. The top site configurations of adsorbed CO are highlighted (CO$_{linear}$) and show poor signals. Reprinted (adapted) with permission from Ref.[118] Copyright 2018 American Chemical Society.

Then, it becomes hard to determine if an intermediate is either not present during the reaction or if the sensing platform did not resolve the vibrational mode well enough. Certainty can then only be gained by measuring a certain vibrational band, not by not measuring it. For example, top site configurations of adsorbed CO (shown as CO$_{linear}$ in Figure 2.10) on metallic surfaces are very difficult to detect with SEIRAS when electrochemically roughened electrodes are used (Figure 2.10).[118] The avenue pursued in this work is to improve the sensing power and reproducibility of the SEIRAS electrode to make negative results more significant.

2.4.2   The Stark Shift

The Stark shift is a field-dependent shift in the central frequency of a vibrational molecule associated with an adsorbate resulting from the interaction between a molecule's dipole and the electric field present at the interface.[123] Changes in a surrounding electric field will change the energy levels of the adsorbed molecule. For example, during the CO$_2$RR, when the applied potential is tuned more negatively, a decrease in the CO wavenumber results.[123] A possible explanation is that the occupancy of the CO antibonding 2π* molecular orbital is increased, leading to a decreased bond strength.[124] Moreover, changes in the bond length affect the charge donation between the metal and the molecular orbitals of the adsorbate.[125] The Stark shift can provide valuable insights into

adsorption and desorption processes, as well as the electronic properties of the adsorbates, by measuring the shifts in vibrational frequencies in response to an applied electric field.

3. Methodology

The results presented in this work followed a systematic process, starting with the conception of the project and culminating in its completion as a coherent storyline documented in a manuscript. Discussions with colleagues and supervisors were invaluable in developing and evaluating new ideas, finding solutions to problems, improving results, choosing the next steps, and compiling and organizing the results into a cohesive narrative for manuscripts aimed for publication in scientific journals. The process flow started with an idea, usually a metasurface with novel optical features or providing a solution for a specific problem, and continued with numerically modeling, optimizing, and evaluating it. If the simulations looked promising based on chosen metrics specific to an idea, then the metasurface was fabricated. The fabrication procedure usually involved a multitude of steps, which each needed to be optimized. Therefore, the priority should lie in preparing quick prototypes to verify the theory and simulations. The prototype was then characterized experimentally and its performance was assessed via data analysis. If the results appeared promising, the simulation-fabrication-experimental characterization-data analysis workflow was repeated iteratively to improve the results, with each step being optimized. In this chapter, we elucidate the methodology used in this work.

3.1   Numerical Models

As discussed in Chapter 2, nanophotonic theory is constrained to specific idealized conditions, such as an ideal sphere, lossless or perfectly conducting materials, a perfect interface, etc. This makes analytical models inaccurate when the behavior of real nanophotonic systems, such as metasurfaces, is investigated. The theory outlined in Chapter 2 shows, in part, analytical models that assume continuous problems. When the continuous problems become too complex to describe analytically, a solution is to discretize the problem to approximate its continuous nature, a process called the finite element process. The finite element process requires the continuum to be split up into finite elements characterized by a finite set of parameters. The final solution comes from a set of linear equations being solved across the assembly of elements following the rules of standard discrete problems.[126]

In the context of developing metasurfaces, therefore, it is instrumental to employ numerical models to study them. In this work, the finite-element frequency-domain Maxwell solver of CST Studio Suite 2021 was used to numerically model metasurfaces.

There are two different key methods to model the interaction of light and matter. The first is the Fourier-transform time-domain method. It solves Maxwell's equations as differential equations (see Chapter 2) in time steps Δt across a rectangular mesh making up the numerical model.[127] Multiple frequencies can be evaluated within one simulation making it advantageous when broad frequency ranges are required. In contrast, the finite-element frequency-domain Maxwell solver used here assumes a time-harmonic dependence of the electromagnetic fields, which allows Maxwell's equations to be converted into the frequency domain as[64]

$$\nabla \times \mu^{-1} \nabla \times \mathbf{E} - \omega^2 \varepsilon \cdot \mathbf{E} = i\omega \mathbf{J}, \tag{3.1}$$

where $\mathbf{J}$ is the current density, which acts as a source for the electric field.

Within the frequency-domain solver, electric and magnetic fields are described by phasors with a harmonic time dependence. The time-harmonic fields are given by

$$\mathbf{E}(t) = \Re\left[\mathbf{E}(\omega) \cdot e^{i\omega t}\right]. \tag{3.2}$$

Typically, the simulations have to be carried out frequency by frequency with every frequency solving a system of equations. This would be very time-consuming. However, CST Studio Suite 2021 uses a broadband sweep technique optimized to derive a full broadband spectrum from a small number of frequency samples. We chose the default general-purpose broadband sweep and set the stop criterion based on the convergence of all available S-parameters at 0.01 with two checks.

S-parameters are the elements of the scattering matrix that depend on the number of ports that are chosen. CST Studio Suite 2021 introduces electromagnetic radiation into the system via power waves. For n amount of ports, an incoming wave a_i and outgoing wave b_i at port i are given by

$$a_i = \frac{1}{2}\left(\frac{V_i}{\sqrt{Z_i}} + \sqrt{Z_i}I_i\right), \tag{3.3}$$

$$b_i = \frac{1}{2}\left(\frac{V_i}{\sqrt{Z_i}} - \sqrt{Z_i} + I_i\right), \tag{3.4}$$

where V_i is the voltage, I_i is the current, and Z_i is the reference impedance, which relates voltage and current.

The scattering matrix $\mathbf{S}$ relates the incoming and outgoing radiation via

$$\begin{pmatrix} b_1 \\ b_2 \\ b_3 \\ \cdots \\ b_n \end{pmatrix} = \mathbf{S} \begin{pmatrix} a_1 \\ a_2 \\ a_3 \\ \cdots \\ a_n \end{pmatrix} \tag{3.5}$$

Then, $\mathbf{S}$ can be written as

$$S = \begin{pmatrix} S_{11} & S_{12} & S_{13} & \cdots & S_{1n} \\ S_{21} & S_{22} & S_{23} & \cdots & S_{2n} \\ S_{31} & S_{32} & S_{33} & \cdots & S_{3n} \\ \cdots & \cdots & \cdots & \ddots & \cdots \\ S_{n1} & S_{n2} & S_{n3} & \cdots & S_{nn} \end{pmatrix}, \tag{3.6}$$

where the matrix elements S_{ij} are called S-parameters. In the frequency-domain solver, the S-parameters are frequency-dependent

$$S_{ij} = S_{ij}(\omega). \tag{3.7}$$

The diagonal elements of the scattering matrix describe the reflection, and the off-diagonal elements describe the transmission at each port.

To solve equation (3.1), the finite element method was used, which splits a one-, two-, or three-dimensional model up into small volume elements across which the electric or magnetic fields are approximated to be uniform. For fields to be uniform, the phase change across an element must be negligible. Therefore, the size of the mesh cells should not be larger than $\lambda_n/4$, where λ_n is the wavelength of light in the material of the mesh cell. A tetrahedral mesh with up to eight iterations of adaptive mesh refinement was used to locally increase the number of mesh cells where needed. The advantage of the tetrahedral mesh is that non-rectangular surfaces can be resolved more accurately. Upon convergence of the simulation, each mesh cell will be associated with a calculated field value, which can be extracted and used to create the electric near-field plots presented in this work.

In particular, metasurfaces confine light at corners where more mesh cells are needed to resolve the electromagnetic near fields. During the adaptive tetrahedral mesh refinement, an error of the field solutions is calculated across a number of frequencies located within the entire frequency range. Where the estimated error is high, the mesh is refined locally. When the convergence or stopping criteria are reached, the adaptive mesh refinement procedure stops. We chose the range of passes from a minimum of three to a maximum of eight, with a threshold error of S-parameters of 0.01 and one check. The stop criterion is reached upon the convergence of all near and far field probe frequency spectra.
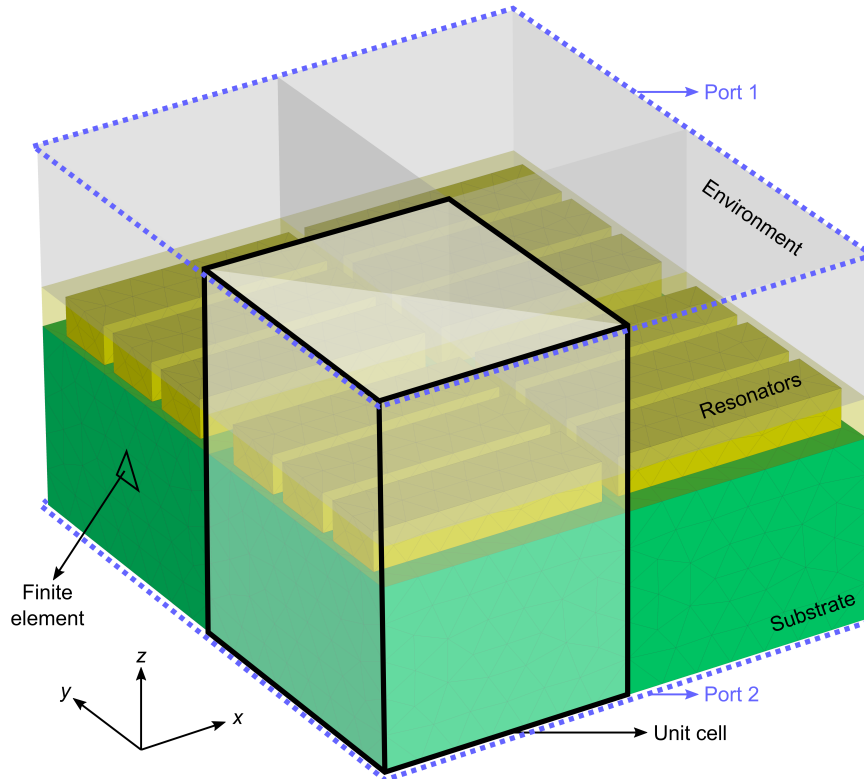
Figure 3.1. Schematic of the numerical model using the finite element method. The mesh of the substrate (green) and the resonators (yellow) is shown, with one finite element being highlighted. The environment mesh is not shown for clarity. The unit cell of the model (white translucent box) constitutes the elementary unit of the periodic metasurface, infinitely repeated in the *x* and *y* directions. Two ports are oriented normally to the *z* direction to introduce or transmit light or function as an electric port.

Modeling periodic metasurfaces was achieved by modeling their unit cell (Figure 3.1) and choosing appropriate boundary conditions. Periodicity in the sample plane (*xy*-plane) was achieved via perpendicular unit cell boundaries and parallel open ports introducing plane waves. Impedance-matched open boundaries extend the touching geometry virtually to infinity by using a perfectly matched layer, where waves can pass with minimal reflections. In this work, only the fundamental *s* or transverse electric (TE) and *p* or transverse magnetic (TM) polarized plane waves were introduced into the system, written as TE(0,0) and TM(0,0), respectively. The Floquet modes were limited to propagating modes only, which are characterized by a real and non-zero wavevector. No Floquet modes with an imaginary wavevector were included in the simulation and therefore convergence was reached faster. This limited artifacts and sped up the calculations.

If light was introduced at an angle larger than the critical angle, total internal reflection occurred. In that case, no signal was received by the port on the opposite side of the light-introducing open port, which caused problems as the errors on the S-parameters could

51

no longer be calculated. This problem was mitigated by setting the non-receiving port to an electric port, acting as a perfect electric conductor. A perfect electric conductor sets all tangential electric fields and normal magnetic fluxes to zero.

A number of important considerations had to be made, especially when light at a non-normal angle of incidence was introduced into the system via an azimuthal ϕ and polar θ phase shift/scan angle. First, the background, an environment assumed by the software to encapsulate the unit cell and crucial in the impedance matching procedure of the ports, had to be defined to match the permittivity of the material adjacent to the open port introducing light. The environment can only take a real and non-dispersive permittivity value. Therefore, the material immediately adjacent to the open ports had to be real and non-dispersive too.

The materials other than the substrate and environment were modeled depending on how strongly the material-dependent losses and dispersion was across the considered spectral range. For example, Si is only marginally dispersive with low losses across the NIR to mid-IR spectral range. For that reason, we modeled Si via $\tilde{n} = 3.48$. For the metals modeled in this work, losses and dispersion effects had to be considered. For this reason, the experimental data of the complex refractive index was used to model gold[128] and platinum.[129] The refractive index was converted to the permittivity as described in Chapter 2 and then inputted into CST Studio Suite.

If a layer of dispersive substrate or environment is placed adjacent to the non-dispersive layer next to a port, then an artificial interface between a dispersive and non-dispersive layer is created with the dispersive layer being modeled as finite instead of infinite. This leads to artifacts resulting from artificial scattering at the interface where the refractive index is not matched. By artifacts, we mean spectra that show sharp resonances that vanish for non-trivial changes in the model geometry, such as increasing the substrate or environment layers that should not affect the spectra. Moreover, Fabry-Perot modes can appear as artifacts due to the limited thickness of the dispersive substrate or environment layer. For this reason, the second consideration that was made to accurately model metasurfaces was to approximate the environment and substrate as real and non-dispersive materials to minimize artificial scattering effects. In the NIR to mid-IR spectral range, CaF_2, as the substrate, was modeled via a real and non-dispersive refractive index $\tilde{n} = 1.4$, air via $\tilde{n} = 1$, and water (or K_2CO_3) via $\tilde{n} = 1.33$.

Dielectric/semiconductor materials, such as CaF_2 or Si, transmit light in the visible to mid-IR spectral range. All-dielectric metasurfaces feature resonances with light confined within the resonators. The relatively extended electromagnetic near fields in these materials can be resolved easily and the default setting of CST Studio Suite 2021 usually sufficed. In contrast, in the mid-IR spectral range metasurfaces composed of metallic resonators feature light confinement into significantly tighter spots than for all-dielectric/semiconductor materials, as discussed in Chapter 2. Therefore, the resolution of the near fields required for metallic structures had to be much higher than for all-dielectric/semiconductor materials. This, in turn, required a higher number of mesh cells.

Moreover, the penetration of light into the metal is negligible in the NIR to mid-IR spectral range. Since the electric and magnetic field values, which are calculated across each mesh cell, are extremely small inside but close to the metal-air interfaces, the solver showed weaknesses in the form of artifacts in the S-parameters due to a too high number of mesh cells being generated during the adaptive mesh refinement procedure ($>10^5$). We will refer to this phenomenon as over-meshing.

The intuitive method of improving the quality of the simulations, i.e. increasing the number of adaptive mesh refinement passes, decreasing the threshold error of the S-parameters below 0.01, and increasing the number of checks, can lead to over-meshing that leads to artifacts. One solution to over-meshing consists of decreasing the maximum number of adaptive mesh refinement passes. This procedure reduced artifacts but decreased the fidelity of the calculated spectra, in particular around the resonances. In fact, often the resonance line shape and central frequency were found to change via non-trivial geometrical changes. Therefore, over-meshing was instead reduced by adding frequency samples to the frequency-domain solver parameters. For example, convergence was improved drastically by adding four equidistant frequency samples around the resonance and six more across the entire frequency range. Moreover, the solver accuracy resulted in optimal results when it was set at 10^{-6} for dielectric/semiconductor materials. For metals, the above procedure worked best at a solver accuracy of 10^{-4}. Lower accuracy limits usually lead to artifacts, while higher limits lead to convergence problems.

A better strategy to model metals in the mid-IR spectral range was to take advantage of the fact that light is expelled from metals in that spectral region. Metals were approximated as perfect electric conductors and modeled via their surface impedance via an internal macro. The numerical simulations converged significantly faster with a reduced number of mesh cells needed ($\sim10^4$). The model did not generate mesh cells inside the metallic resonators as it assumed no field inside them.

3.2   Nanostructure Fabrication

Once the numerical models showed promising capabilities and the structural parameters were optimized, the metasurfaces were fabricated in a multi-step procedure that itself needed to be optimized. Nanofabrication procedures are strongly affected by changes in temperature, pressure, and humidity. Therefore, the fabrication was performed in a clean room ensuring a constant temperature of 21-22 °C, pressure of 1 atm, and humidity at 50%.
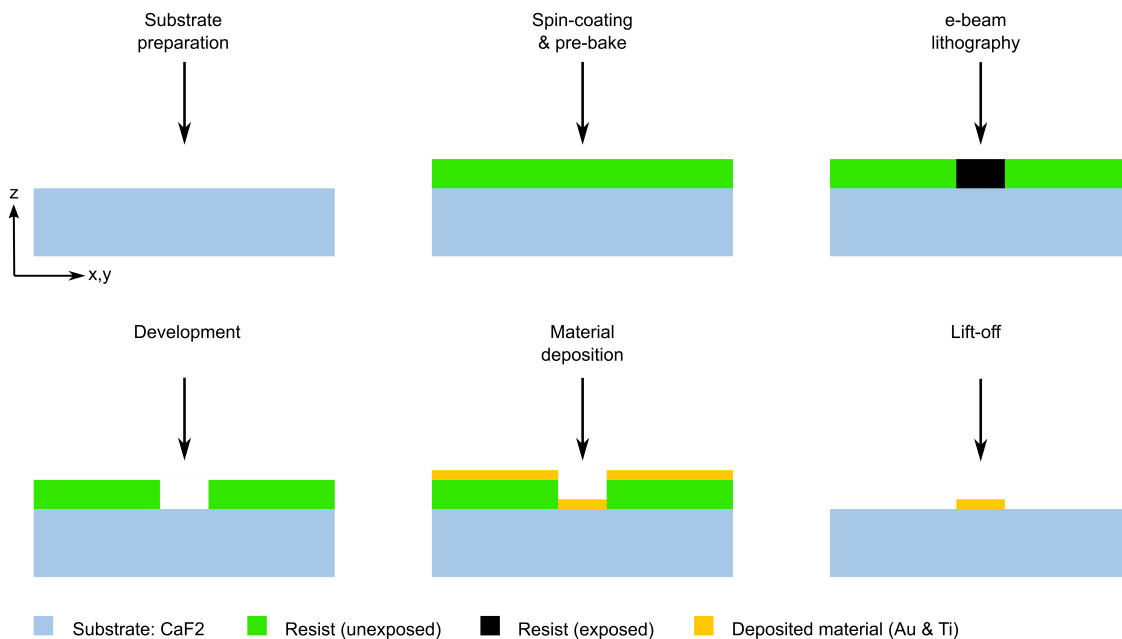
Figure 3.2. Schematic fabrication protocol of the positive metallic metasurfaces.

3.2.1 Substrate Preparation and Cleaning

For all samples presented in this work, CaF_2 windows were used as the substrate due to their transparency in the mid-IR spectral region. Two different shapes of substrates were used throughout this work. For the electrochemical measurements, round (diameter 25 mm) and thin (thickness 0.5 mm) CaF_2 windows were used to comply with the requirements of the electrochemical cell. For the metasurfaces based on bound states in the continuum, square (side length 10 mm) and thicker (thickness 1 mm) CaF_2 windows were used.

The substrate was cleaned in acetone inside an ultrasonic bath at 55 °C for at least 5 minutes, followed by isopropanol rinsing for at least 30 s to prevent acetone residues. Isopropanol was used as it dries without leaving behind contaminating traces on the substrate surface. Then, the substrate was placed in an oxygen plasma cleaner (Diener electronic) at 100 W and 40 Hz for 5 minutes. The oxygen plasma cleaner removed contamination and increased the substrate's surface energy, which facilitated better substrate surface wetting. Via the increase in the hydrophilicity of the substrate surface, the air between the surface and the layer of subsequently spin-coated resists or deposited materials was removed, promoting the adhesion of the resists, improving its quality, and decreasing its surface roughness.
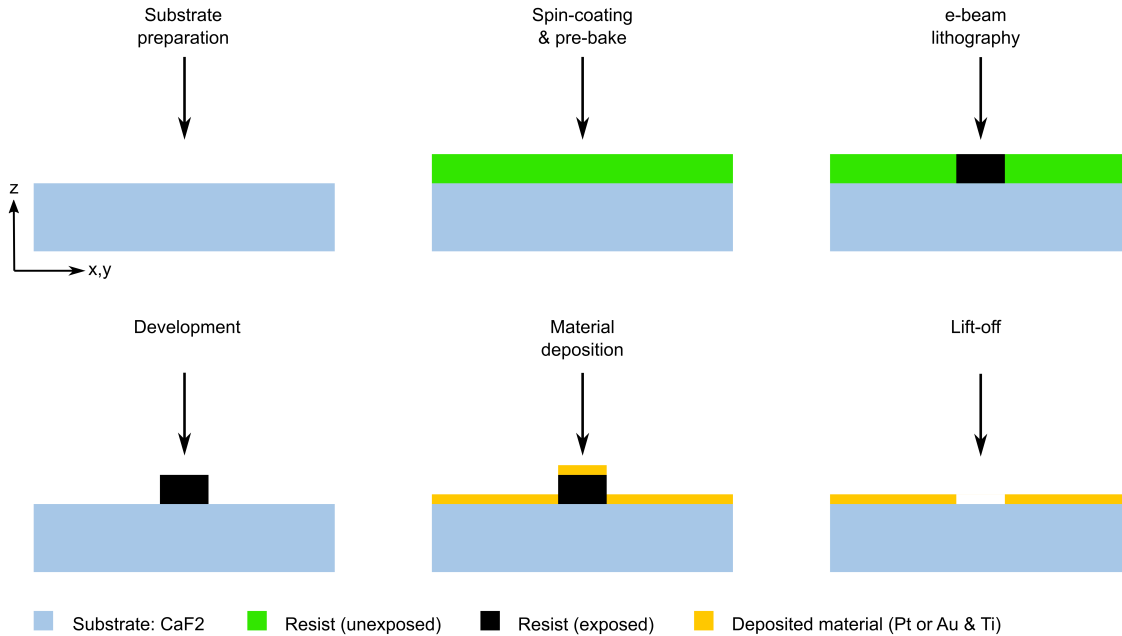
Figure 3.3. Schematic fabrication protocol of the inverse metallic metasurfaces.

3.2.2 Resist Spin-Coating, Prebaking, Lithography, and Lift-Off

After the substrate (CaF_2 or CaF_2 with amorphous silicon) was cleaned, it was spin-coated with a layer of either negative or positive tone resist. Resists can have their chemical bonds locally changed either via the exposure of an electron beam (e-beam) of a scanning electron microscope or by a light beam. Since we used e-beam lithography in this work, we will continue to talk about resists that are activated via electrons. E-beam lithography was used to create the metasurface patterns in resist. The fundamental difference between negative and positive resists is how they interact with electrons. When positive resists are exposed to electrons, the electrons trigger a chemical reaction that breaks down the molecular bonds within the resist (Figure 3.2 and Figure 3.4). Then, when the resist is developed, which means that it is placed for a certain amount of time in an organic solvent, the area that was exposed to electrons is washed away. In contrast, when negative resists are exposed to an e-beam, the local surplus of electrons triggers a chemical reaction that stabilizes and forms molecular bonds within the exposed area of the resist (Figure 3.3 and Figure 3.5). Then, when the resist is developed, the area exposed to the e-beam remains, while the area not exposed to the e-beam is washed away. Therefore, these two resists have the power to produce inverse designs due to their inverse functionality.
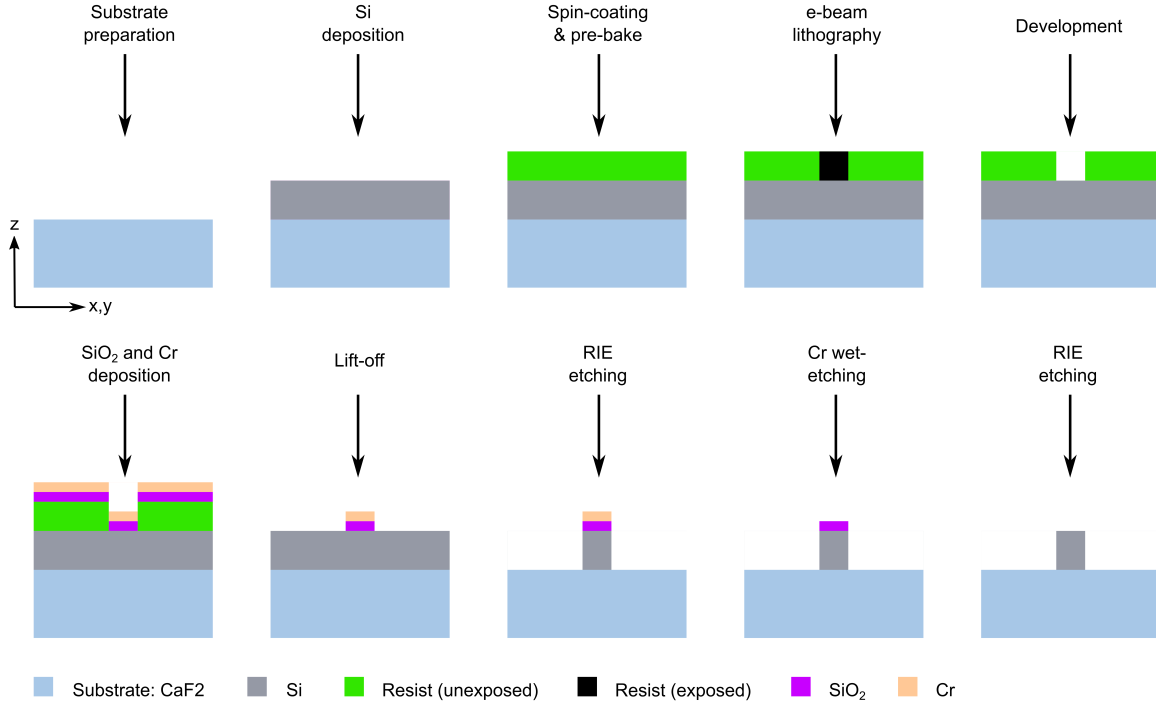
Figure 3.4. Schematic fabrication protocol of the positive all-dielectric metasurfaces.

The first step after the sample was prepared and cleaned was to spin-coat the resist. The resist was applied to the substrate in its liquid form. The centrifugal force coming from the rotations of the spin coater then redistributed the resist across the substrate's surface. The centrifugal force

$$F = m\omega^2 r \qquad (3.8)$$

is an inertial force that pulls an object of mass m at a distance from the origin r away from the origin with a strength proportional to ω^2, where ω is the angular velocity. Therefore, with increasing ω the centrifugal or the redistributing force increases and the resist film thickness decreases as more resist is accelerated away.

Proper adherence of the resist to the substrate's surface was crucial, wherefore the oxygen plasma step, as explained in Section 3.2.1, should not be omitted. In particular, the negative resist (ma-N 2403, micro resist technology GmBH, Germany) showed poor adhesion on CaF_2. For this reason, an adhesion promoter (Surpass 4000, micro resist technology GmBH, Germany) was first spin-coated at 3000 rotations per minute for 30 s, without a prebake step, before the negative resist was spin-coated.
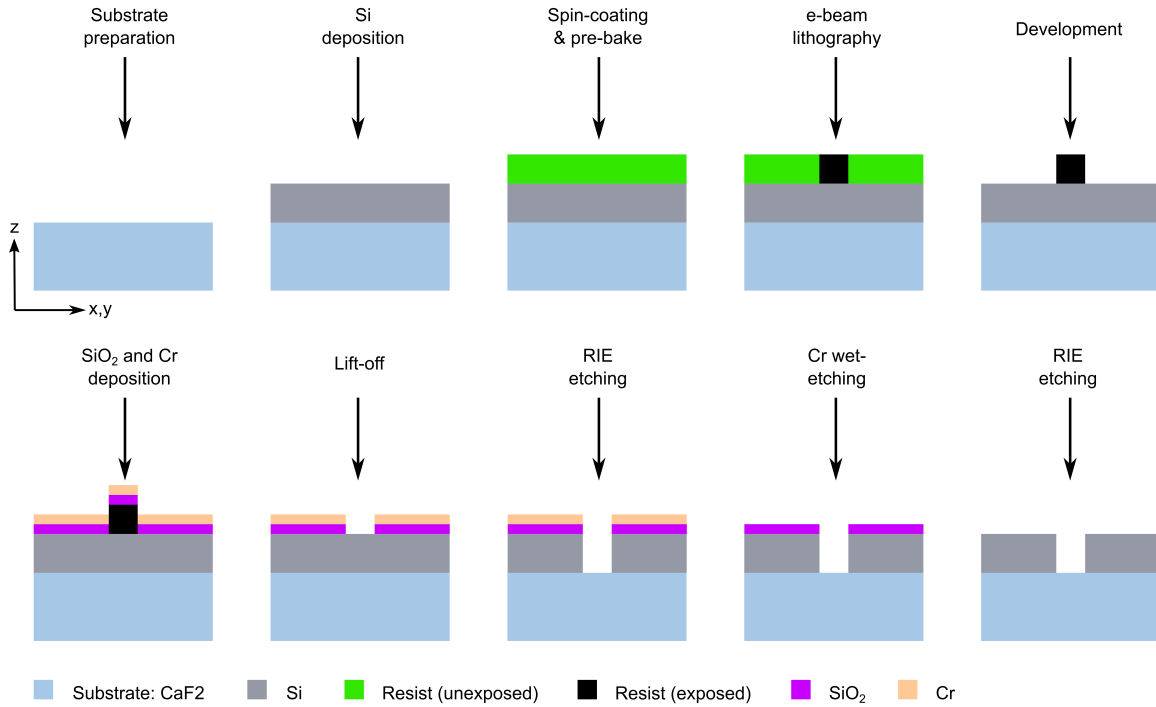
Figure 3.5. Schematic fabrication protocol of the inverse all-dielectric metasurfaces.

How thick the resist layer became after spin-coating depended on what resist was used. Different resists have different viscosities. A resist with a higher viscosity results in a higher average resist thickness at the same spin rate than a resist with a lower viscosity. The spinning time also affects the resist thickness and uniformity. Longer spinning times result in a smoother resist surface but thinner resist film. The companies producing each resist usually provide information on the thickness of their specific resist depending on what spin rate and spinning time is used. The relevant table should first be consulted before choosing a certain spin protocol.

As a rule of thumb, for positive resists, the film thickness should be at least three times the cumulative thickness of the evaporated materials, after development, to succeed in the lift-off procedure. For the negative resist we used, ma-N 2403, we found that the resist thickness had to exceed six times the cumulative thickness of evaporated materials for the lift-off to work. The difference in these values stems from the electron interaction volume of the e-beam inside the resist leading to an undercut profile for the positive resist and an overcut profile for the negative resist. When materials are evaporated into the exposed and developed resist areas, the undercut profile limits or prevents material from depositing on the sidewalls. When the sample is placed in removing solution after material deposition, the exposed sidewalls allow the solution to access and dissolve the resist, thereby facilitating the lift-off. On the other hand, the interaction volume of the e-beam leads to an overcut profile in negative resists. The overcut profile leads to material being

deposited on the resist sidewalls, which negatively affects the lift-off procedure. Therefore, a thicker negative resist layer relative to the thickness of evaporated materials is needed.

To meet the requirements of the positive metasurface shown in this work, the positive resist poly(methyl methacrylate) (PMMA, 950k, A4) was spin-coated at 3000 rotations per minute for one minute ensuring a resist thickness of above 200 nm. The negative resist was spin-coated at 3000 rotations per minute for 30 s ensuring a resist film thickness of 300 nm.

The positive resist was then prebaked at 180 °C for 3 minutes on a hot plate. A Si wafer was used between all samples and the hot plate to decrease the high-temperature gradients. The prebake step removed the remaining solvent from the resist and formed the molecular bonds that were then broken down by e-beam exposure. Since the negative resist (ma-N 2403) turns into a hard mask at high temperatures or long baking times, it was prebaked at 100 °C for 1 minute on a hotplate. To avoid resist burning and electronic charge accumulations leading to pattern distortions during e-beam lithography an additional conducting polymer layer (ESpacer 300Z) was spin-coated at 2000 rotations per minute for 1 minute.

After the spin-coating and prebake step, the samples were introduced into the ultra-high vacuum chamber of the e-beam lithography (eLine Plus, Raith) machine. The lower acceleration voltages caused a more pronounced undercut (overcut) profile for the positive (negative) resists due to the interaction volume shifting closer to the surface of the resist. Therefore, an acceleration voltage of 20 kV (30 kV) was used. The working distance was 10 mm and the aperture sizes ranged between 15 and 20 μm. The smaller the aperture size the smaller the beam current and focus diameter. Moreover, the area dose, defined as the charge per area, was constrained by the current of the e-beam and the speed at which the beam was deflected, which was 15 mm s^{-1}. Therefore, smaller apertures were used when a higher resolution was required or the beam dose had to be below the allowed threshold linked to a larger aperture.

The ideal dose depended strongly on the development time. For example, for longer development times more time is available to dissolve areas exposed with the e-beam in the case of a positive resist. Then, a lower dose is ideal as the molecular bonds do not need to be completely broken apart for them to be dissolved in the developer solution. The contrary is true for negative resists. If the development time is too long, however, the unexposed resist gets partly dissolved, leading to rougher metasurface edges. Therefore, the development time is crucial and characteristic to each resist. To determine the ideal development time, a dose sweep was performed on various samples for various development times.

The best results then determined the best development time and area dose, which was 70 s in ma-D 525 (micro resist technologies GmBH, Germany) after using an area dose of 60-70 μC cm^{-2} for ma-N 2403. The development was stopped by placing the sample in

deionized and distilled water for 30 s. The e-beam patterns in PMMA were developed by first removing the conductive polymer in deionized and distilled water for 20 s, then developing the patterns for 50 s in a 7:3 mixture of isopropanol to water solution after exposure with an area dose of 140-220 µC cm^{-2}. The development was stopped by placing the sample in isopropanol for 30 s. Then the samples were placed in an oxygen plasma cleaner at 40 W for 15 s to obtain sharper edges.

After the development step, materials were deposited onto the resist patterns, either as a hard mask for etching or to create the metasurface patterns directly via a lift-off procedure. Either way, a lift-off was necessary. The lift-off consisted of placing the sample in remover overnight at 80 °C. Mr-REM 700 (micro resist technologies GmBH, Germany) was used to remove the remaining ma-N 2403. We found that the remover left behind residual material that contaminated the surface, which was removed by rinsing the sample in deionized and distilled water for 1 min, then for 1 min in isopropanol, and finally by cleaning the sample at 100 W power in an oxygen plasma cleaner for 20 min. Remover 1165 (Microposit) was used to remove the remaining PMMA.

3.2.3 Material Deposition

Materials ranging from metallic to dielectric were used to create the metasurfaces described in this work. Au, Pt, Ti, Cr, and SiO$_2$ were deposited via e-beam evaporation (Figure 3.6a) after the resist was spin-coated. Their metasurface patterns were created solely via a lift-off procedure. In contrast, amorphous silicon (a-Si) was deposited before the resist spin-coating via plasma-enhanced chemical vapor deposition (PECVD), shown schematically in Figure 3.6b. The metasurface patterns were then created via an etch mask and an etching procedure.

3.2.3.1 Electron-Beam Evaporation

Electron-beam evaporation is a physical vapor deposition technique utilizing a beam of high-energy electrons to heat and evaporate a material. Two different e-beam evaporators were used in this work. For the evaporation of Pt and Ti in the context of electrochemical experiments (Figure 3.3), the electron-beam evaporator PRO Line PVD 75 from Lesker was used. For the evaporation of Au, Ti, Cr, and SiO$_2$ in the context of metasurfaces based on bound states in the continuum (Figure 3.2, Figure 3.3, Figure 3.4, and Figure 3.5), the UHV E-Beam from Bestec was used. The reason for the use of both was their different availability of materials.
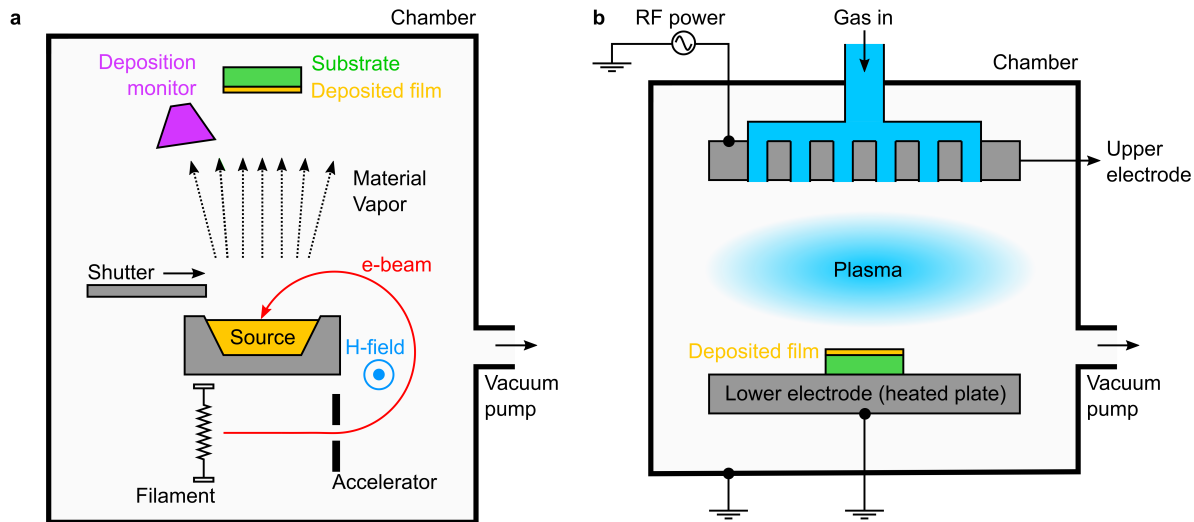
59

Figure 3.6. Material deposition techniques. Schematic illustrations of (a) electron-beam evaporation and (b) plasma-enhanced chemical vapor deposition.

For both systems, the samples were mounted upside down on a sample holder which was then introduced into the e-beam evaporator's chamber (Figure 3.6a). After an ultra-high vacuum was created (pressure below 10^{-5} bar), electrons were extracted from a filament by driving a current through it, accelerated via an electric field (accelerator), and deflected onto the target material or source via a magnetic field. The electrons hit the source locally, where they heated and sublimated the material when the e-beam strength and therefore local temperature were high enough. The sublimated atoms rose towards the top of the chamber, where they attached to the substrate.

Due to the high vacuum, the sublimated atoms only rarely scatter with atoms in the chamber. This leads to an overall directionally uniform evaporation that aids the lift-off procedure, making this technique advantageous compared to e-beam sputtering when e-beam lithography patterns involve a lift-off. The lower vacuum of e-beam sputtering leads to the coating of the side walls of the developed e-beam lithography patterns, making the lift-off difficult to impossible, because the removing solutions are then prevented from accessing the resist.

By adjusting the electric current driven through the filament, the e-beam strength can be changed and optimized to reach a stable rate of evaporation. However, with an increase in the evaporation rate, the vacuum can decrease if the limit of the vacuum pump is reached. Moreover, when the rate gets too high, it can become unreliable for the deposition monitor (quartz crystal controller) that monitors the rate of evaporation. In addition, the temperature in the chamber increases with the increased heating of the source due to higher extraction currents and higher evaporation rates. Some resists, including the negative resist used in this work (ma-N 2403), become etch masks when

60

exposed to elevated temperatures for extended time periods. Conversely, however, a too-low evaporation rate can lead to high surface roughness in the created films and lead to problems in monitoring the rate. For this reason, the range of acceptable evaporation rates should first be found. For Au, a rate of 1 Å s^{-1} was used, for Ti 0.4 Å s^{-1}, for Pt 2 Å s^{-1}, for Cr 0.4 Å s^{-1}, and for SiO^2 0.8 Å s^{-1}. In particular, the relatively high evaporation rate for Pt of 2 Å s^{-1} was crucial as the lift-off worked significantly better than for lower rates. Moreover, the quality of the resonator edges improved significantly as the surface roughness decreased with higher evaporation rates.

A further material-dependent consideration had to be made for ideal e-beam evaporation. If a material melts during the e-beam evaporation process, the e-beam can be used in its collimated form without destroying the material. As the material is locally evaporated, nearby material flows into the hole created by the evaporation process. However, when the target materials do not melt during the evaporation process, as the material is locally evaporated and a hole is left behind, no surrounding material fills the hole and the hole remains. To avoid this problem, for these non-melting materials, the e-beam should be widened to increase its cross-section and therefore uniformly use the target material.

3.2.3.2   *Plasma-Enhanced Chemical Vapor Deposition*

Plasma-enhanced chemical vapor deposition (PlasmaPro 100, Oxford Instruments) was used for the deposition of amorphous silicon (Figure 3.4 and Figure 3.5). The sample was introduced bottom-up into an ultra-high vacuum chamber, where it was placed on top of a lower electrode (Figure 3.6b). Inside the chamber, a constant flow of 500 sccm of silane gas (SiH$_4$) was introduced, resulting in a chamber pressure of 1000 mTorr. A plasma was generated between the substrate and the radiofrequency (RF) electrode using 10 W of RF power. A plasma is a state of matter in which atoms are fully ionized. The RF power provided the energy to the electrons that ionized the gases. The plasma initiation triggered a chemical reaction on the substrate's surface, leading to Si as one of the reaction products. Silicon then condensed on the surface of the substrate, where it produced a uniform layer of amorphous silicon. The presence of the plasma had the beneficial effect of reducing the required silicon growth temperature on the substrate by lowering the reaction's activation energy. In this work, Si was deposited at 180 °C.

During plasma-enhanced chemical vapor deposition, the deposition rate or film thickness is proportional to the deposition time. With a deposition rate of 18.4 nm/min a thickness of 650 nm of a-Si was achieved after 35 min 20 s.

3.2.4 Hard Mask and Reactive Ion Etching

A hard mask was used to create the Si-based metasurfaces studied in this work. The hard mask was created by first coating an exposed and developed resist on a-Si and CaF$_2$ with 20 nm of SiO$_2$ and 40 nm of Cr. Then, an overnight lift-off created the hard mask patterns to be etched. The patterns were then transferred into Si via inductively-coupled plasma reactive ion etching (ICP-RIE, PlasmaPro 100, Oxford Instruments), a chemical dry etching technique (Figure 3.4 and Figure 3.5).

The ICP source was a coil wrapped around the main chamber carrying an RF time-varying electric current. The RF time-varying electric current created an RF time-varying magnetic field inside the chamber, which in turn generated RF electric fields that provided energy to the electrons that ionized the gas molecules and atoms, thereby creating the plasma. Due to the electric fields that ionized the gas inside the chamber, the advantage of coupling ICP and RIE was minimal erosion of the reactor walls. During ICP-RIE, the ions were attracted toward the wafer to be etched.

The hard mask protected the material underneath it. Hard masks are made of materials that do not interact with the gases during the RIE process. To etch the areas the a-Si film that were not protected by the hard mask, chlorine, and argon gases with a laminar flow of 20 and 7 sccm, respectively, were introduced into the chamber at a pressure of 2 mTorr. Then, the plasma was ignited using 20 W of RF and 200 W of ICP power. Then, the areas not covered by the hard mask were exposed to the plasma, which reacted with a-Si. The reaction with a-Si led to gaseous products only, which were removed via the vacuum pump. The areas protected by the hard mask remained intact. Due to the RF applied to the plasma, RIE is a directional etching technique with a reduced lateral etch rate, nearly vertical sidewalls, and sharp edges.[130] For this reason, metasurfaces with high fidelity and small-scale resonators can be made.

Similarly to PECVD, the etching rate is proportional to the etching time. With a rate of approximately 90 nm/min, we etched our 650 nm a-Si film for 7 min 15 s to make sure the a-Si film was fully etched, but not over-etched.

3.2.5 Fabrication Recipes

The four fabrication protocols used to create the metasurfaces presented in this work are briefly summarized below.

3.2.5.1   *Positive Metallic Metasurfaces*

The fabrication protocol of the positive metallic metasurfaces (Figure 3.2) started by first preparing and cleaning the substrate, then spin-coating and prebaking the positive resist (PMMA, 950k, A4) and the conductive polymer layer. Afterwards, e-beam lithography exposed the resist where it was to be removed via the development step. An adhesion layer (2 nm of Ti) and 70 nm of Au were then deposited on the sample via e-beam evaporation. A final lift-off step produced the final metasurface patterns.

3.2.5.2   *Inverse Metallic Metasurfaces*

The fabrication protocol of the inverse metallic metasurfaces (Figure 3.3) commenced with the substrate preparation and cleaning step. Then, the adhesion promoter (Surpass 4000), negative resist (ma-N 2403), and conductive polymer layer were spin-coated and prebaked. E-beam lithography exposed the resist where it was to be retained during the development step, while the unexposed areas were removed. Afterwards, an adhesion layer (2 nm of Ti) and then either 30 nm of Au or Pt were deposited on the sample via e-beam evaporation. A final lift-off step produced the final metasurface patterns.

3.2.5.3   *Positive All-Dielectric Metasurfaces*

The fabrication protocol of the positive all-dielectric metasurfaces (Figure 3.4) started by preparing and cleaning the substrate and then depositing 650 nm a-Si on it via PECVD. Afterwards, the positive resist (PMMA, 950k, A4) and conductive polymer layer were spin coated and prebaked. Then, e-beam lithography exposed the resist where it was to be removed via the development step. The hard mask was created by depositing 20 nm of SiO_2 and 40 nm of Cr via e-beam evaporation. The hard mask patterns were created via a lift-off and transferred to the a-Si layer via ICP-RIE. Finally, Cr and SiO_2 were etched away, leaving behind the finished positive all-dielectric metasurface.

3.2.5.4   *Inverse All-Dielectric Metasurfaces*

The fabrication protocol of the inverse all-dielectric metasurfaces (Figure 3.5) started with the preparation and cleaning of the substrate and then depositing 650 nm a-Si on it via PECVD. Then, the adhesion promoter (Surpass 4000), the negative resist (ma-N 2403), and finally the conductive polymer layer were spin-coated and prebaked. E-beam lithography exposed the resist where it was to be retained during the development step, while the unexposed areas were removed. The hard mask was created by depositing 20

nm of SiO_2 and 40 nm of Cr via e-beam evaporation. The hard mask patterns were created via the lift-off and transferred to the a-Si layer via ICP-RIE. Finally, Cr and SiO_2 were etched away, leaving behind the finished inverse all-dielectric metasurface.

3.3   Optical Characterization

Two purely optical and one hybrid-opto-electrochemical characterization devices were used to characterize the metasurfaces developed in this work. In the context of metasurfaces based on BICs, Quantum Cascade Laser (QCL) IR Microscopy and Fourier-transform IR (FTIR) spectroscopy were used. In the context of electrochemical measurements, a hybrid-opto-electrochemical platform was used that combined cyclic voltammetry (CV) and FTIR spectroscopy in an ATR configuration.

3.3.1   Quantum Cascade Laser IR Microscopy

For the near-normal incidence optical measurements presented in this work, we used a wide-field spectroscopic microscopy and imaging platform (Spero Chemical Imaging Microscope, DRS Daylight Solutions, USA) based on broadly tunable mid-IR quantum cascade lasers (QCL-IR) (Figure 3.7a). QCLs were first experimentally demonstrated by Jerome Faist et al.[131] and theoretically predicted by et al.[132] They are semiconductor-based lasers that emit in the mid to far-IR spectral range, between 5.56 to 10.55 μm (1800-948 cm^{-1}) for the QCL used in this work.

Conventional lasers are based on bulk semiconductor materials that emit light when electrons in the conduction band recombine with holes in the valence band. In contrast, QCLs use only electrons undergoing a chain of intersubband transitions to lower conduction energy levels as they pass through a superlattice semiconductor heterostructure. The size quantization of the periodic arrangement of semiconductor layers leads to the splitting of the conduction band into multiple subband energy levels. When electrons move through the superlattice, they move down a potential staircase. Every time they transition to a lower energy level, they release photons. The potential staircase consists of coupled quantum wells where population inversion is designed via the precise control of tunneling.
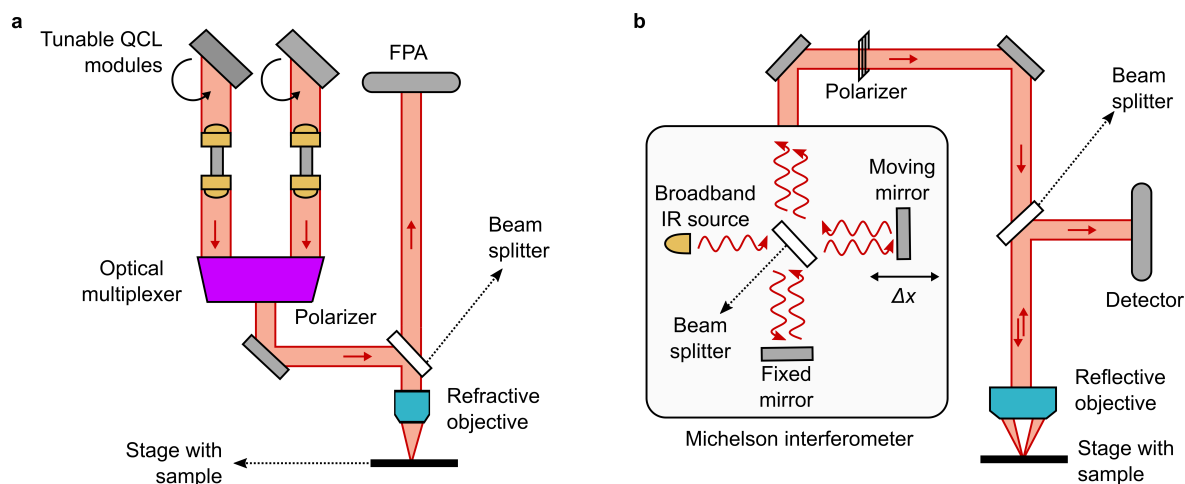
Figure 3.7. Schematics of the optical characterization techniques used in this work. (a) Schematic of the QCL-based mid-IR spectral imaging microscope equipped with a refractive objective and focal plane array detector (FPA). (b) Schematic of the FTIR spectrometer equipped with a reflective objective and a liquid-nitrogen-cooled mercury cadmium telluride detector. A linear polarizer gave control over the polarization of light. Both instruments were operated in reflection.

The QCL-IR microscope (Figure 3.7a) comprised an array of QCLs, a low numerical aperture (0.15) objective (Figure 3.8a) with a low 4× magnification and a 2 mm^2 field of view, and an uncooled IR-sensitive focal plane array detector. In advancing incremental time steps, the QCL was tuned through the mid-IR wavelength range, with the QCL emitting light in a narrow wavelength range at each point in time. The laser's exact wavelength was precisely controlled by adjusting an external cavity frequency-selective element, typically a diffraction grating. Moreover, the QCL featured a well-defined linear polarization state. Therefore, the polarization of light was rotated by rotating the sample on the sample stage. The measurements were conducted in reflection and normalized to the reflection signal of a plain gold mirror. A broadband and uncooled microbolometer camera was operated at video frame rates to collect real-time, single-frequency (step size of 0.5 cm^{-1}), and rapid hyperspectral images of the samples. The hyperspectral reflectance data corresponding to the metasurfaces were then averaged to reduce noise.

3.3.2   Fourier-Transform IR Spectroscopy

FTIR spectroscopy uses broadband IR as the light source in a Michelson interferometer with one fixed and one moving mirror (Figure 3.7b). The Michelson interferometer was used infamously during the Michelson-Morley experiment to investigate the speed of Earth through what they believed to be ether.[133] The light from the light source is split into two paths by a beam splitter. Light taking the first path is reflected back to the beam

splitter by a fixed mirror. Light taking the second path is reflected by a moving mirror back to the beam splitter. When the distance between the two mirrors and the beam splitter is the same, the entire broadband spectrum interferes constructively at the beam splitter, where they continue (partially) towards the sample and then the detector. In our case, a linear polarizer was used in front of the sample to allow control over the polarization.

As the distance between the movable mirror and the beam splitter was changed, a selection of wavelengths within the broadband spectrum was periodically amplified and blocked via constructive and destructive interference. Each position of the moveable mirror corresponded to a different interference between the two light beams, at which the power of incident transmitted or reflected light was recorded.

A Fourier transform then transformed the interferogram (displacement of the mirror in cm) into its inverse, the spectra in wavenumbers (cm^{-1}). Assuming a 50-50 beam splitter, the intensity received by the detector as a function of the path difference $I(\delta)$ was converted into the intensity in wavenumbers $B(v)$ or spectrum via[134]

$$B(v) = \int I(\delta)e^{i2\pi\delta v}d\delta. \qquad (3.9)$$

Here, a VERTEX 80v FTIR spectrometer (Bruker) was used in reflection mode to characterize BIC-based metasurfaces (Figure 3.7b). A gold mirror was used as a reference. Blackbody radiation from a thermal source was used to provide broadband radiation. The peak wavelength was tuned by changing the source temperature. The consequence of using a thermal source, however, was thermal noise that needed to be suppressed via a cooled detector. We used liquid nitrogen to cool a mercury cadmium telluride detector down to 77 K. The spectra were recorded with a resolution of 4 cm^{-1} and averaged across at least 32 scans.

To study small sample regions, the FTIR spectrometer was paired with a HYPERION 3000 microscope (Bruker). The microscope used a reflective microscope objective (Newport) with a numerical aperture of 0.4 and 15× magnification to illuminate the sample and collect its signal in reflectance (Figure 3.8b). The range of polar angles taken in by the reflective objective was between 12° and 23.6°.

3.3.3 Refractive and Reflective Microscope Objectives

In this work, the use of refractive and reflective microscope objectives served the purpose of experimentally showing the degradation in the performance of metasurface-driven resonance based on their angular dispersion. By comparing the same resonance under both objectives, conclusions on their angular robustness could be made. If a resonance was more angular robust, it changed less during a switch from a refractive to a reflective microscope objective in terms of Q factor, signal modulation, coupling constants, and resonance position.
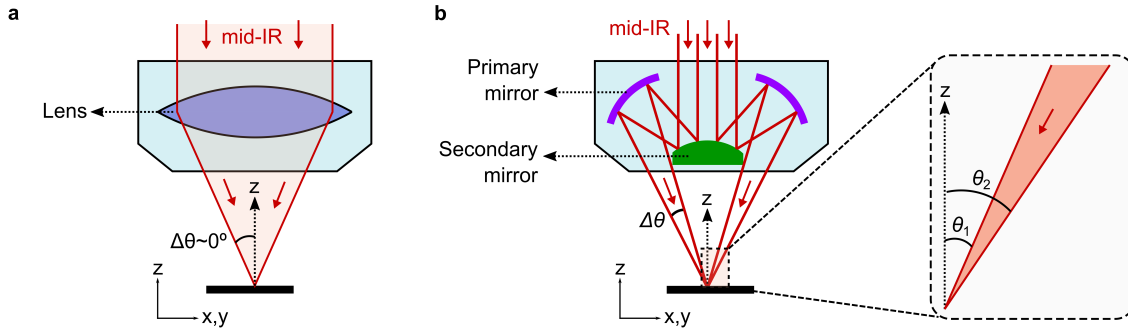
Figure 3.8. Schematics of the two fundamental types of objectives used in this work. (a) The basic concept behind a refractive objective is at least one lens that focuses light at a point by the use of refraction. The angle created by the focal cone is usually negligible and is centered around 0°. (b) A reflective objective has a primary and secondary mirror that reflect light into a focus. However, light comes in at a range of angles that are all larger than zero.

Refractive objectives require multiple glass elements with different Abbe numbers and refractive indices to control chromatic aberrations.[135] This strongly limits the wavelength range in which refractive objectives can operate and makes them unsuitable for broadband sensing or white light applications.[135] In the simplest case, a refractive objective is composed of one confocal lens that is used to focus light on a sample (Figure 3.9a). Due to the nature of foci, there is a small spread of incidence angles reaching the sample at the focal point. Since this spread is minimal and around $\theta = 0°$ (normal incidence), the spread of incidence angles $\Delta\theta$ is usually ignored.

In contrast, reflective microscope objectives use mirrored surfaces to focus light (Figure 3.8b). This process is inherently independent of the wavelength within a larger spectral range. The advantages of refractive microscope objectives are a high numerical aperture, a large working distance, and no chromatic aberration.[136–138] Therefore, reflective optical systems are the objectives of choice when broadband achromatic focusing is required, especially in the near to mid-IR range.[139] The main drawback of reflective objectives is the angular spread $\Delta\theta = \theta_2 - \theta_1$ with a nonzero average. Our objective featured $\theta_1 = 12°$ and $\theta_2 = 23.6°$. In the context of optical metasurfaces, this meant that resonances with a significant angular-dependent dispersion were only weakly detectable under a reflective objective.[43] Since strong resonances are vital for sensing applications, angular-robust resonances must be designed for reflective objectives.

67

3.4 In-Situ Opto-Electrochemical Measurements

The SEIRAS results presented in this work were measured in situ by recording the electrochemical and optical signals simultaneously via combining cyclic voltammetry and FTIR spectroscopy (Vertex 80, Bruker), respectively (Figure 3.9). The electrochemical cell was the IMAC chamber from Bruker. A specular reflection unit (VeeMax III from PIKE Technologies) paired with a CaF_2 prism and light polarizer introduced light at 72° w.r.t. an electrochemical jackfish cell, thereby enabling the attenuated total internal reflection geometry. The specular reflection unit was purged with nitrogen. The metasurface arrays faced upwards into the electrochemical cell (Figure 3.9).

Gold was tried first as the material of the metasurface following the same design as with the nano-slots, but with different structural parameters optimized to match the resonance with CO_{linear}. The CO_2RR on Au features low overpotentials and a high selectivity.[50] However, we were unable to detect CO_{linear} on Au during CO saturation, CO oxidation, and CO reduction. Even the detection of CO_{linear} on an electrochemically roughened thin gold film (thickness of 20 nm with 0.5-1 nm Ti) was sporadic and unreproducible. Notably, we found that the type and thickness of the metal adhesion layer played a significant role in the success rate of CO_{linear} detection, with 0.5 nm of Ti being the most successful adhesion layer. Habteyes et al.[108] offer a potential explanation for the adhesion layer thickness dependence on the success rate of the detection of CO_{linear}. According to them, the thickness of a metallic adhesion layer critically and negatively affects a metallic metasurface-driven resonance. The thicker the adhesion layer, the lower the Q factor and signal modulation of the resonance.

A switch from Au to Pt resulted in more reproducible results on an unstructured Pt film (thickness 20 nm with 0.5-1 nm Ti), again with the ideal thickness of the adhesion layer being 0.5 nm. Cr as an adhesion layer instead of Ti resulted in a lower success rate in detecting CO_{linear}. As the metasurface was created, an adhesion layer of only 0.5 nm often resulted in the lift-off of large parts of the metasurface arrays, thereby destroying the sample. A potential explanation could be that the holes in the Pt film allowed for the electrolyte to seep in under the Pt film and lift it off from the bottom. To mitigate this problem, we chose an adhesion film thickness of 1 nm.

The background of the resonance characterization was taken on the same metasurface but with *p* polarized light because the nano-slot metasurface-driven resonance was active under *s* polarization only. For the experiments aiming at the detection of CO adsorbed in top and bridge site configuration, the background was taken with *s* polarized light before CO was introduced into the electrochemical cell. The measurements were taken with *s* polarized light as the potential of the counter electrode was changed. In either case, the recorded data of the metasurface-active pixels was averaged to reduce the signal-to-noise ratio. A baseline correction and Savitzky–Golay filter were applied to the spectra.
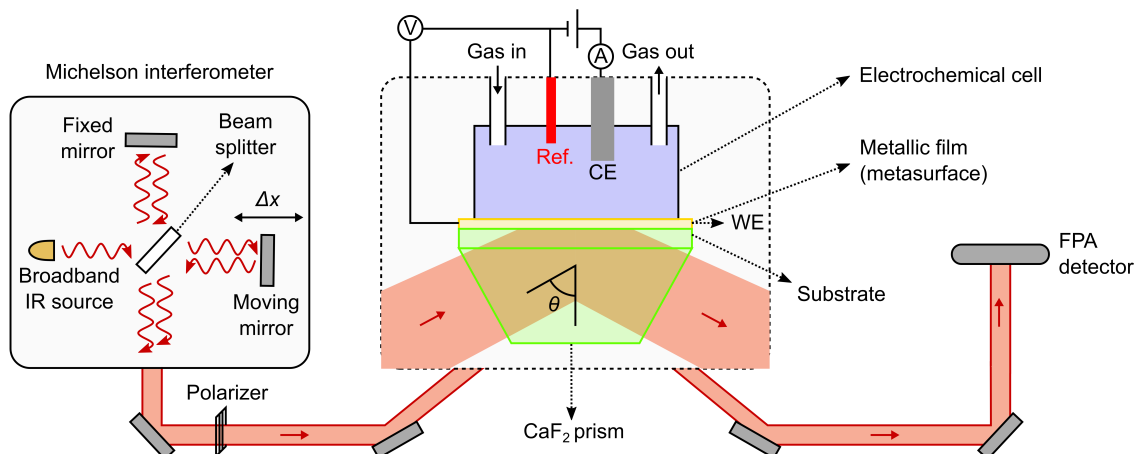
Figure 3.9. Schematic of the opto-electrochemical experimental set-up. The optical signals were monitored in an ATR geometry with an FTIR spectrometer. The mid-IR light was polarized via a linear polarizer and recorded with a focal plane array detector (FPA). To minimize reflection losses at the air-CaF$_2$ interface, a CaF$_2$ prism was used that was configured to have its sidewalls perpendicular to the Poynting vector of incident light. Simultaneously, the electrochemical experiments were performed via cyclic voltammetry. A counter electrode (CE) applied a potential compared to the working electrode (WE) in the electrochemical cell and was measured in comparison to a reference electrode (Ref.). The working electrode was the metallic film of the metasurface. Gases were introduced and expelled via tubes connected to the electrochemical cell.

Cyclic voltammetry was performed via the classical three-electrode system, consisting of a saturated calomel electrode (E = 0.244 V_{SHE}), a platinum wire as a counter electrode, and the platinum sample as working electrode. The IMAC chamber was equipped with a liquid-nitrogen-cooled focal plane array detector composed of 64 × 64 mercury cadmium telluride detectors. Each detector collected its own interferogram, which was then converted into a spectrum via a Fourier transform (see Section 3.3.2). To discern the pixels attributed to absorption coming from the metasurface arrays, each spectrum was integrated around the spectral range of the metasurface-driven resonances (between 1600 to 2800 cm^{-1}). The integration procedure delivered a pixelated two-dimensional absorbance heat map showing a strong contrast between the metasurface arrays and the unstructured Pt film.

Prior to the first characterization, the samples were cleaned via electrochemical cycling. A cyclic voltammogram (20 mV s^{-1}) was recorded to confirm the cleanliness of the electrode surface. For each sample, the resonance was measured in K$_2$CO$_3$ (0.5M, pH 11.9) electrolyte saturated with either Ar, CO, or CO$_2$. Each spectrum was recorded with a resolution of 4 cm^{-1} and the final absorbance heat map resulted from an average of 32 scans for the results shown in Chapter 5 and 10 scans for the results shown in Chapter 6. The signal enhancement factor of the nano-slot metasurfaces was

obtained by dividing the maximum value(s) of the differential absorbance peak(s) corresponding to the vibrational mode(s) of CO measured by our metasurfaces by the peak differential absorbance value measured on a pure Pt layer (30 nm) without nanostructures.

The adsorption of CO during the transition from Ar to CO-saturated electrolyte (0.5M K_2CO_3) was studied using the nano-slot metasurface with the best overlapping resonance with the vibrational mode of CO adsorbed in a top site configuration. Cleaning and background acquisition protocols were the same as described above. Carbon monoxide slowly flowed into the electrochemical cell and spectra were acquired regularly during the transition from Ar to CO-saturated electrolyte at the open circuit potential (OCP).

The oxidation of CO during potential sweeps was investigated after 2 h of CO bubbling. For the results shown in Chapter 5, a cyclic voltammogram, with a slow scan rate (0.25 mV s^{-1}), from the OCP to + 1700 mV$_{RHE}$ and back to −100 mV$_{RHE}$ was performed and a spectrum was acquired every 100 mV. For the results shown in Chapter 6, after bubbling CO for 2 hours, cyclic voltammetry was performed from +1650 mV$_{RHE}$ to -85 mV$_{RHE}$, using a scan rate of 0.25 mV.s^{-1}.

For the results shown in Chapter 6, finally, the electrolyte was saturated with CO_2, which decreased the pH to approximately 8. After 2h of gas bubbling, cyclic voltammograms were measured with a slow scan rate of 0.25 mV s^{-1}, from the OCP to + 1425 mV$_{RHE}$ and then back to +25 mV$_{RHE}$. SEIRAS spectra were acquired in intervals of 100 mV.

4. Metallic and All-Dielectric Metasurfaces Sustaining Displacement-Mediated Bound States in the Continuum

The results presented in this chapter are published in Ref.:[20]

Typically, metasurfaces featuring BICs are based on all-dielectric resonators arranged into a periodic array that break the in-plane inversion symmetry to offer both high-Q factors and strong near-field enhancement, enabling state-of-the-art technologies for sensing[7,34] and enhanced light-matter interactions.[36] In Chapter 2 we outlined a set of features characteristic to BICs and q-BICs by which they can be identified. A similar effect emerges for symmetric metasurfaces sustaining BICs at normal incidence when the angle of incidence is tuned.[37] A few studies[38–41] have been conducted introducing an emerging class of BIC-based metasurfaces that can unlock a finite-Q factor q-BIC resonance by relative displacement tuning while preserving the in-plane inversion symmetry. Another desired aspect of metasurfaces is control over the ratio of their radiative to intrinsic loss rates $\gamma_{ext}/\gamma_{int}$ that allows, for instance, transitioning between electromagnetically induced transparency and absorption.[42] Quasi-BICs allow easy control over the radiative Q factor (see Chapter 2 for the definition of the radiative Q factor) by tailoring the radiative loss rate by changing the asymmetry parameter α.

Apart from a few exceptions,[43,44] studies on nanophotonic or plasmonic metasurfaces yielding high-Q resonances have exclusively focused on (near) normal incidence or angle-multiplexed illumination with experiments focusing on refractive microscope objectives.[45] Unsurprisingly, most conventional metasurfaces based on q-BICs or other nanophotonic or plasmonic principles feature resonances that shift strongly with the angle.[45] While this feature has been exploited for angle-multiplexed sensing,[45] these metasurfaces cannot be used for applications requiring angular robustness (i.e., an optical response that does not vary with incidence angle), such as conformal optical devices, flexible substrate technology, displays, and photonic devices using focused light.[43]
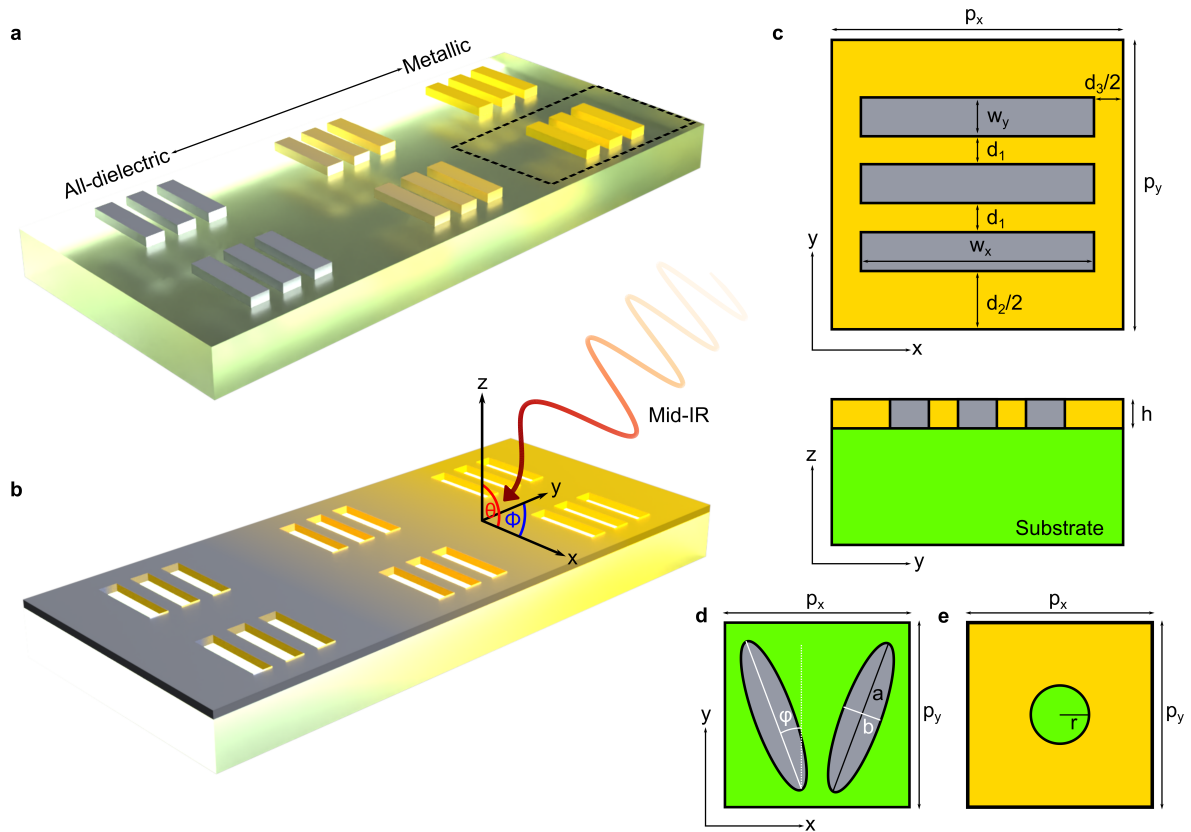
Figure 4.1. The displacement-mediated quasi-BIC metasurface. (a-b) Schematic of the superlattice metasurface made of periodic arrangements of all-dielectric and metallic (a) positive and (b) inverse beams. (c-d) The unit cell of the displacement-mediated q-BIC metasurface from the (c) top and side view. The three beams making up the superlattice have the dimensions $w_x \times w_y \times h$. They are separated in y from each other by a distance d_1 and to the next set of three beams by a distance d_2 and in x by a distance d_3. (d) The unit cell of the tilted ellipses metasurface. The ellipses with a height h are defined by a long axis a and a short axis b. The BIC is converted into a leaky resonance by breaking the in-plane inversion symmetry by tilting the ellipses under an angle φ with respect to the y-axis giving an asymmetry $\alpha = \sin(\varphi)$. (e) The unit cell of the gold nanohole metasurface consisting of cylindrical holes with a radius r and a height h. The dimensions of all unit cells are defined by $p_x \times p_y$.

To date, there are only very few mentions of angular robust metasurfaces in the literature,[43,46,47] with a further paucity of works aimed at a theoretical understanding of angular robustness.[48,49] For example, one study proposed a gold-based metasurface featuring a resonance that can be excited at a small range of angles wherein it shows angular robustness.[37] However, the proposed metasurface requires femtosecond laser writing in photoresist to make structures with different heights, which is difficult with electron beam lithography. A fundamental and systematic study on angular-robust BIC-driven metasurfaces is still missing.

72

Refractive objectives require multiple glass elements with different Abbe numbers and refractive indices to control chromatic aberrations.[135] This strongly limits the wavelength range in which refractive objectives can operate and makes them unsuitable for broadband sensing or white light applications.[135] In contrast, reflective microscope objectives use mirrored surfaces to focus light, a process inherently independent of wavelength within a larger spectral range, with the advantage of high-numerical aperture, large working distance, and no chromatic aberration.[136–138] Therefore, reflective optical systems are the objectives of choice when broadband achromatic focusing is required, especially in the near to mid-IR range.[139] The main drawback of reflective objectives in connection with optical metasurfaces is the difficulty of realizing angular robustness within the operational range of polar and azimuthal angles.[43]

In this chapter, we experimentally realize for the first time metasurfaces that can convert a BIC into a guided-mode resonance in the IR through relative displacement tuning while maintaining the in-plane inversion symmetry. We demonstrate the tolerance of this resonance toward changes in the angle of incident light, showing strong performance in combination with a high-numerical aperture (NA) reflective objective. We investigate both metallic and all-dielectric, positive (Figure 4.1a) and inverse (Figure 4.1b), displacement-mediated quasi-BIC metasurfaces. By inverting the structure, we mean that the material-filled parts of the positive structure become air (or other surrounding material) while the parts that were air (or surrounding material) become structural material. We confirm Babinet's principle (see Chapter 2 for a theoretical description of Babinet's principle), which allows for a straightforward implementation of an inverse (positive) structure if the positive (inverse) one is already understood, thereby broadening its range of applications.

4.1 Analytical Description of the Superlattice

Unlike conventional q-BIC-based platforms, our metasurfaces do not break the in-plane inversion symmetry. Instead, the BIC is converted into a leaky resonance by detuning the displacement of three equally spaced beams ($w_x \times w_y \times h$) forming the unit cell (Figure 4.1c) to adjacent unit cells in y. A displacement asymmetry parameter α can be defined as

$$\alpha = \frac{p_y}{p_{y0}} - 1, \tag{4.1}$$

$$p_{y0} = 3d_1 + 3w_y, \tag{4.2}$$

where p_{y0} is the unit cell length in y (p_y) when the distance between the beams within the unit cell d_1 and the distance between two beams of adjacent unit cells d_2 are the same. Since the beams are made of silicon or gold in air or air in silicon or gold (Figure 4.1c) our metasurface can be regarded as a superlattice.[38] As outlined in Chapter 2, the term

superlattice denotes a planar two-dimensional structural arrangement of unit cells characterized by alternating periodicities of two different materials.

Three superlattice metasurfaces, one silicon-based and two gold-based, are experimentally compared to two conventional metasurfaces used in the mid-IR spectral region, the Si-based tilted ellipses (Figure 4.1d) and gold nanohole (Figure 4.1e) metasurfaces. Both periodically arranged all-dielectric tilted ellipses and metal nanohole metasurfaces have led to cutting-edge breakthroughs in biospectroscopy,[7,45,140,141] catalysis,[16,142] higher harmonic photon generation,[143,144] and more exotic light-matter effects[145,146]. Consequently, they serve as a valuable platform for comparison. We numerically investigate the angular behavior of our metasurfaces and confirm the correct operation of our metasurfaces under near-normal incidence illumination. Then, the feature of angular robustness is explored by illuminating the samples under a reflective microscope objective. We complete our studies by performing a detailed comparison of performance metrics between the metasurfaces, with special attention to the relative changes in the resonances as the range of incidence angles is increased.

4.2   Numerical Design of the Superlattice

The unit cell of our displacement-mediated q-BIC metasurfaces (Figure 4.1c) forms the basis for the numerical simulations. When α is varied for the positive silicon superlattice (Figure 4.2a) a BIC above the Rayleigh anomaly is converted into a leaky resonance when the incident light is polarized with the electric field parallel to the long axis of the beams (Figure 4.2b). The RA is a phenomenon associated with light diffracted parallel to the surface of a periodic structure.[147] When a resonance occurs on the spectrally higher frequency side of the RA the resonance lifetime and electric near-field enhancement are strongly reduced.[74] Therefore, we will limit our investigations to the modes appearing on the spectrally longer wavelength side of the RA. Since the RA is proportional to the unit cell size

$$\Delta\alpha \sim \Delta\lambda_{RA}, \tag{4.3}$$

where λ_{RA} is the center wavelength of the RA. For $\alpha < 0.3$, the q-BIC resonance is spectrally significantly separated from the RA and yields strongly modulating sharp resonances (Figure 4.2c).
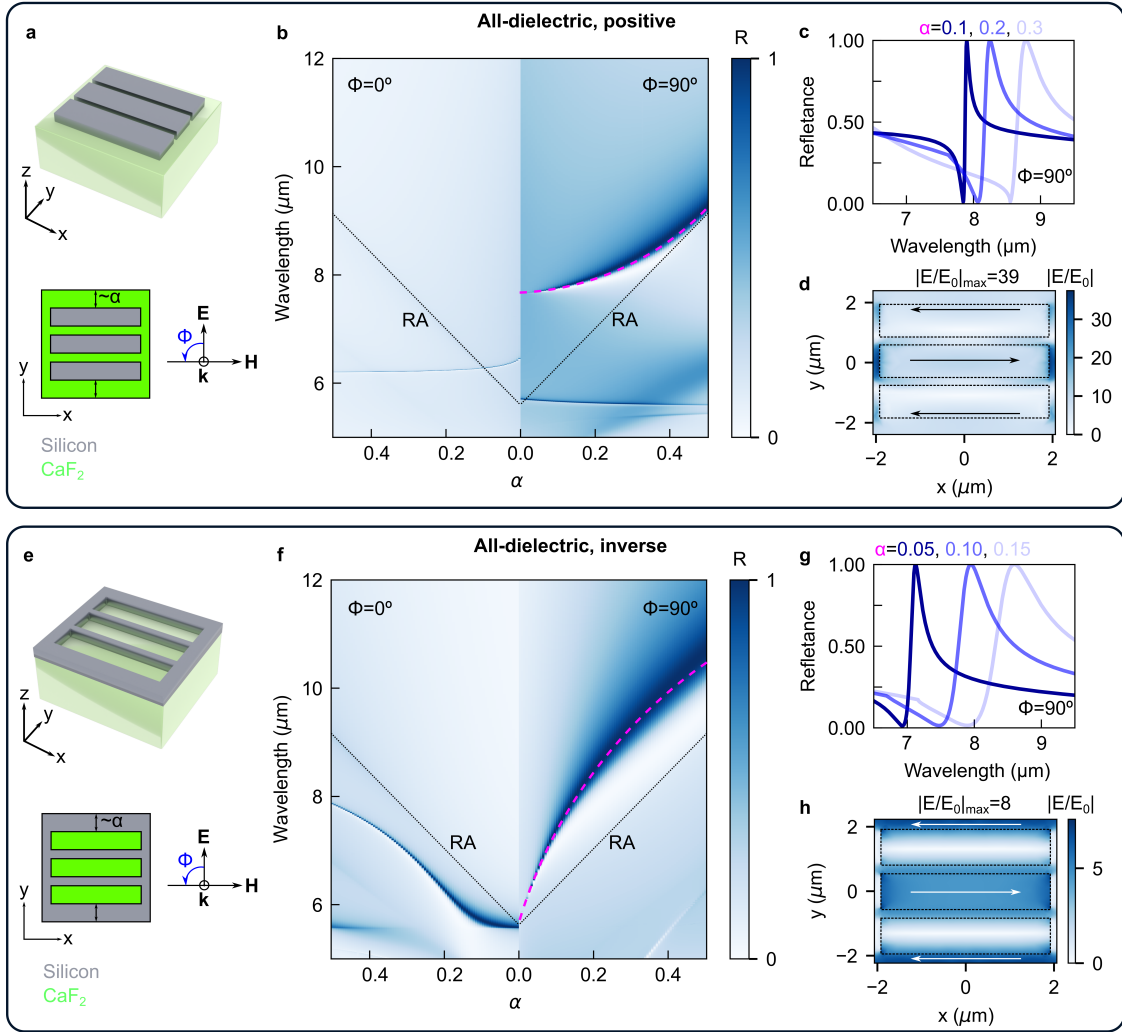
Figure 4.2. Numerical design of the all-dielectric (Si) displacement-mediated q-BIC metasurface. (a) Schematics of the unit cell of the positive silicon superlattice including the polarization of the normal incident light considered in the simulations, where **E** and **H** are the incident electric and magnetic field vectors, and **k** is the Poynting vector. Φ rotates the field vectors around the **k** axis. (b) The numerical reflectance spectra of the positive silicon superlattice, with $w_x = 3.85$ µm, $w_y = 1.1$ µm, $d_1 = d_3 = 275$ nm, $h = 650$ nm, recorded while varying α from 0 to 0.5 when Φ is 0° (left half) and 90° (right half). At $\Phi = 90°$ the q-BIC (pink-dashed line) appears around 8 µm and spectrally shifts closer to the RA with increasing α. (c) Selected reflectance spectra showing the q-BIC resonance at $\alpha = 0.1, 0.2, 0.3$. (d) Electric near-field distribution $|E/E_0|$ for $\alpha = 0.1$ at $z = h/2$, including schematic electric field vectors (black arrows), with a local maximum of 39. (e) Schematics of the unit cell of the inverse silicon superlattice similarly to (a). (f) The numerical reflectance spectra of the inverse silicon-based superlattice with the parameter definitions provided in (b) while varying α from 0 to 0.5 when Φ is 0° (left half) and 90° (right half). At $\Phi = 90°$ the q-BIC (pink-dashed line) appears on the longer wavelength side of the RA. (g) Selected reflectance spectra showing the q-BIC resonance at $\alpha = 0.1, 0.2, 0.3$. (h) Electric near-field distribution $|E/E_0|$ for $\alpha = 0.05$ at $z = h/2$, including schematic electric field vectors (white arrows), with a local maximum of 8.

The numerical multipolar expansion of the positive silicon superlattice performed by Shi et al.[38] confirmed the nature of the q-BIC and revealed the primary contributing modes as the toroidal dipole and magnetic quadrupole modes. At α = 0.1, a maximum local electric field enhancement $|E/E_0|_{max}$ of 39 is obtained, where E_0 and E is the incident and local electric field at $z = h/2$ (Figure 4.2d). This value shares an inverse relationship with α. Electric charge accumulates in an alternating fashion around the short edges of the beams.

The mechanism of q-BIC formation can be understood from the electric near-field plots. At the BIC condition, each adjacent beam has the local electric field confined to its core polarized along its long axis but in opposing directions to impede far-field radiation via cancellation of dipole moments. When a collection of beams is periodically displaced, the electric field in the central beam remains the same while the electric field of the outer two beams is pressed towards the outer edges of the beams, where the field scatters into the far field (Figure 4.2d).

We find that for the superlattice made of silicon, there is an inverse structure that works similarly to its positive counterpart. However, to the best of our knowledge, there is no analytical theory linking the physical properties of two inverse all-dielectric structures. The unit cell of the inverse silicon-based superlattice with the same parameters as its positive counterpart (Figure 4.2e), similarly to it, produces a q-BIC resonance for $\alpha \neq 0$ for light polarized with its electric field aligned parallel to the long axis of the beams (Figure 4.2f). Both the positive and inverse all-dielectric superlattice feature a q-BIC resonance above the RA under the same polarization.

Interestingly, as α is increased, the q-BIC resonance shifts to longer wavelengths faster than the RA, which opposes the behavior of its positive counterpart. Since the same definitions apply to the inverse as to the positive structure, the RA shift is proportional to equation (4.3). Compared to the positive silicon superlattice, the inverse's q-BIC resonance maintains a similar albeit more symmetrical Fano-type lineshape (Figure 4.2g). Moreover, its resonance increases in strength and detunes from the BIC condition at a faster rate.

For α = 0.05 the local electric near field reaches a maximum value of 8 which is considerably lower than for its positive counterpart with a maximum value of 39 at α = 0.1. The lower α for the inverse structure was taken due to the q-BIC resonance detuning faster from the BIC condition with increasing α. Due to the lower field enhancement, electric charge accumulates less around the short edges of the beams, compared to the positive silicon-based superlattice. The electric field vectors appear similar to the positive structure. Due to the significantly higher local electric near field, the positive structure is expected to be the better candidate for sensing applications.
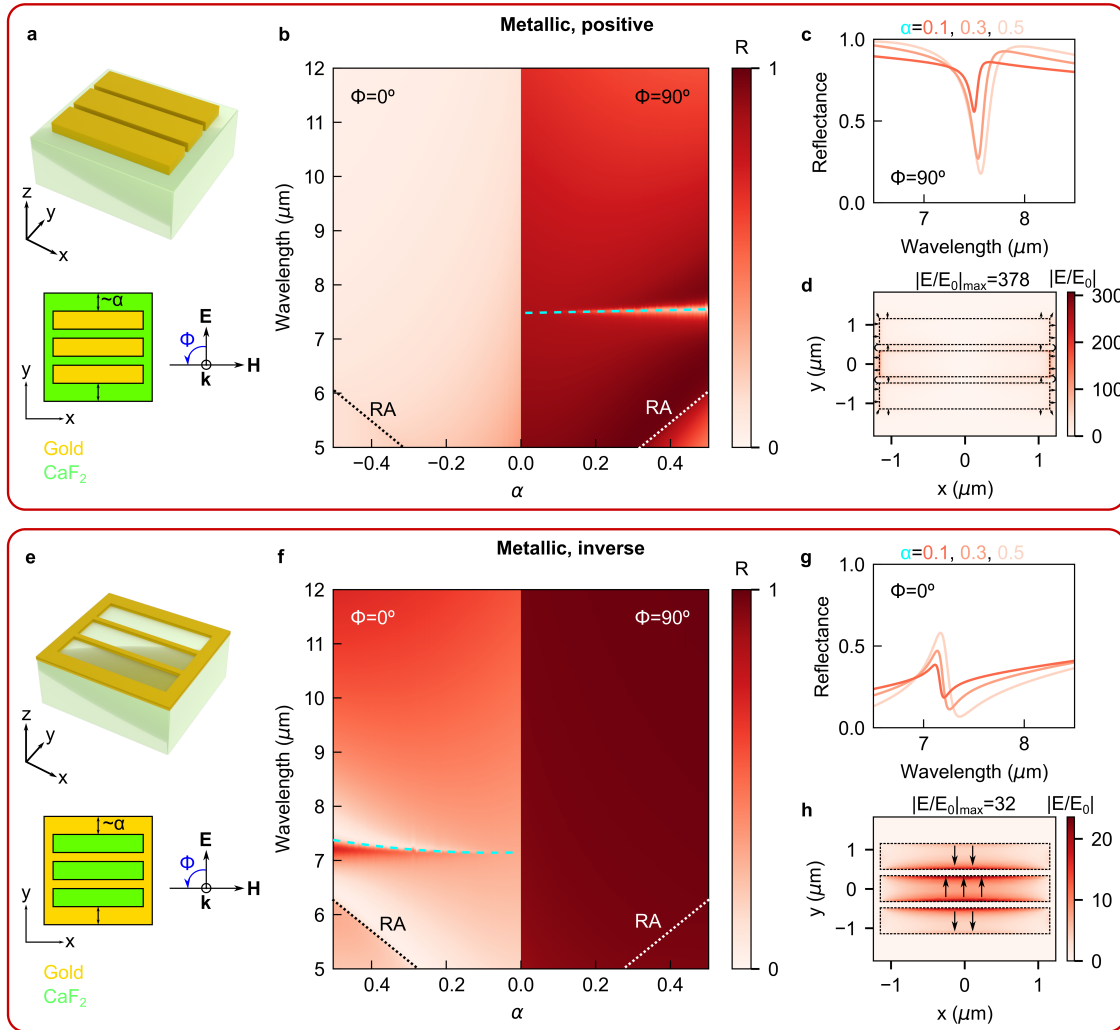
Figure 4.3. Numerical design of the metallic (gold) displacement-mediated q-BIC metasurface. (a) Schematics of the unit cell of the positive gold superlattice including the polarization of the normal incident light considered in the simulations, where **E** and **H** are the incident electric and magnetic field vectors, respectively, and **k** is the Poynting vector. Φ rotates the field vectors around the **k**-axis. (b) The numerical reflectance spectra of the positive silicon superlattice, with w_x = 2.31 μm, w_y = 660 nm, $d_1 = d_3$ = 165 nm, h = 100 nm, recorded while varying α from 0 to 0.5 when Φ is 0° (left half) and 90° (right half). At Φ = 90° the q-BIC (azure-dashed line) appears around 7.5 μm. (c) Selected reflectance spectra showing the q-BIC resonance at α = 0.1, 0.3, 0.5. (d) Electric near-field distribution $|E/E_0|$ for α = 0.3 at the air/CaF$_2$ interface, including schematic electric field vectors (black arrows), with a local maximum of 378. (e) Schematics of the unit cell of the inverse silicon superlattice. (f) The numerical reflectance spectra of the inverse gold-based superlattice with the parameter definitions given in (b) while varying α from 0 to 0.5 when Φ is 0° (left half) and 90° (right half). At Φ = 0° the q-BIC (azure-dashed line) appears on the longer wavelength side of the RA. (g) Selected reflectance spectra showing the q-BIC resonance at α = 0.1, 0.3, 0.5. (h) Electric near-field distribution $|E/E_0|$ for α = 0.3 at the air/CaF$_2$ interface, including schematic electric field vectors (black arrows), with a local maximum of 32.

Changing the material of the beams from silicon to gold (Figure 4.3a), the numerical reflectance spectra look qualitatively similar between the positive all-dielectric and metal superlattice (Figure 4.3b). However, there are a few important differences. First, the q-BIC resonance exhibits only small spectral shifts and grows significantly slower with increasing α compared to the positive silicon counterpart. Furthermore, while the RA shifts according to equation (4.3), the q-BIC resonance is spectrally located significantly further away from the RA, on its higher wavelength side. Since the losses are higher in gold than in silicon, the q-BIC resonances in gold modulate less with lower Q factors (Figure 4.3c), which is to be expected. However, these results appear very promising due to the symmetric line shape and high maximum local electric near-field enhancement of 378 found for α = 0.3 (Figure 4.3d), which can be further increased by decreasing α.

When α = 0, the positive and inverse gold superlattices (Figure 4.3e) become simple plasmonic rods and slots, respectively. Compared to previous plasmonic rod antenna geometries with a maximum achievable electric near-field enhancement of around 50,[52] our positive gold superlattice exceeds the obtained $|E/E_0|_{max}$ by at least one order of magnitude. In this case, the BIC condition consists of canceling out magnetic dipoles that suppress the far-field radiation.

The inverse gold superlattice (Figure 4.3e) features a q-BIC resonance for $\alpha \neq 0$ at normal incidence with the electric field vector polarized perpendicular to the long edge of the slots (Figure 4.3f). As Babinet's principle predicts, a nanostructure's line shape in reflection (transmission) should match its inverse's in transmission (reflection) under a 90-degree change in polarization. For this reason, the line shape of the inverse gold superlattice is less symmetric (Figure 4.3g), as it matches the transmission spectrum of the positive gold superlattice under a 90-degree change in polarization (Figure 4.4a). In contrast, the inverse gold superlattice's q-BIC resonance is significantly more symmetric in transmission (Figure 4.4b) compared to its positive counterpart (Figure 4.4a). Consequently, the inverse gold superlattice can be favorable for many applications requiring a symmetric resonance line shape in transmission, such as biosensing[7].

Due to Babinet's principle, the electric near field vector of the inverse gold superlattice (Figure 4.3h) is rotated by 90 degrees aligned parallel to the short axis of the slots in comparison to its positive counterpart (Figure 4.3d). Here, the BIC condition consists of canceling out electric dipoles. When α is increased the electric or magnetic dipoles no longer perfectly cancel and a scattering channel to the far field is opened. For α = 0.3 $|E/E_0|_{max}$ is 32 for the inverse gold superlattice, which is of the same order of magnitude as plasmonic slots.

In general, it can be easily seen that the first two conditions of BICs are fulfilled by all metasurfaces studied in this work (Figure 4.2b, f, and Figure 4.3b, f). Moreover, the inverse square law between the radiative Q factor Q_{rad} and α also holds true for all metasurfaces (Figure 4.5). Finally, the electric-near field plots (Figure 4.2d, h, and Figure 4.3d, h) also show the opposing electric near-field vectors. Therefore, all conditions are met ensuring that the underlying resonances are q-BICs.
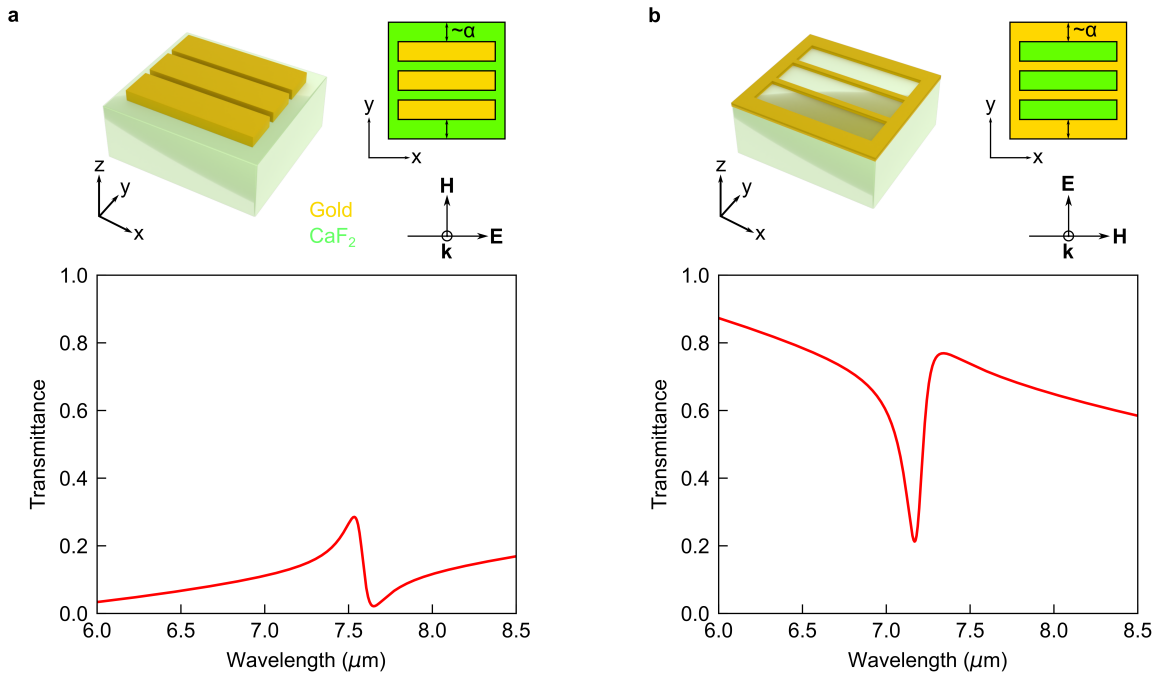
Figure 4.4. The simulated transmission spectra of the gold (a) positive and (b) inverse superlattice for *α* = 0.3 at normal incidence with the same parameters as provided in Figure 3. Schematics are included showing the unit cell and polarization of incident light.

4.1 Numerical Analysis with a Focus on Angular Behavior

A straightforward approach to predict how robust a structure's resonance is towards changes in the angle of incident light is to track the resonance as the polar angle is varied for a fixed azimuthal angle for *s* or TE and *p* or TM polarized light, resulting in an angular dispersion plot (Figure 4.6a-e). Only for metasurfaces with a unit cell whose symmetry belongs to the rotational groups C_n, for n > 2, there is polarization independence of the structure at normal incidence illumination.[148,149] For non-normal angles of incidence the degeneracy of the modes is typically lifted.

The properties extracted from the angular dispersion plots can predict a metasurface's performance under a reflective objective. A reflective objective can be paired with a polarizer that will define the polarization of incident light and will allow for the range of TE to TM polarized light across a window of polar angles.[43] For this reason, two crucial factors affecting the performance of metasurface resonances under reflective objectives are the magnitude and direction of the angular-driven shift in the resonance position for TE and TM polarized light.
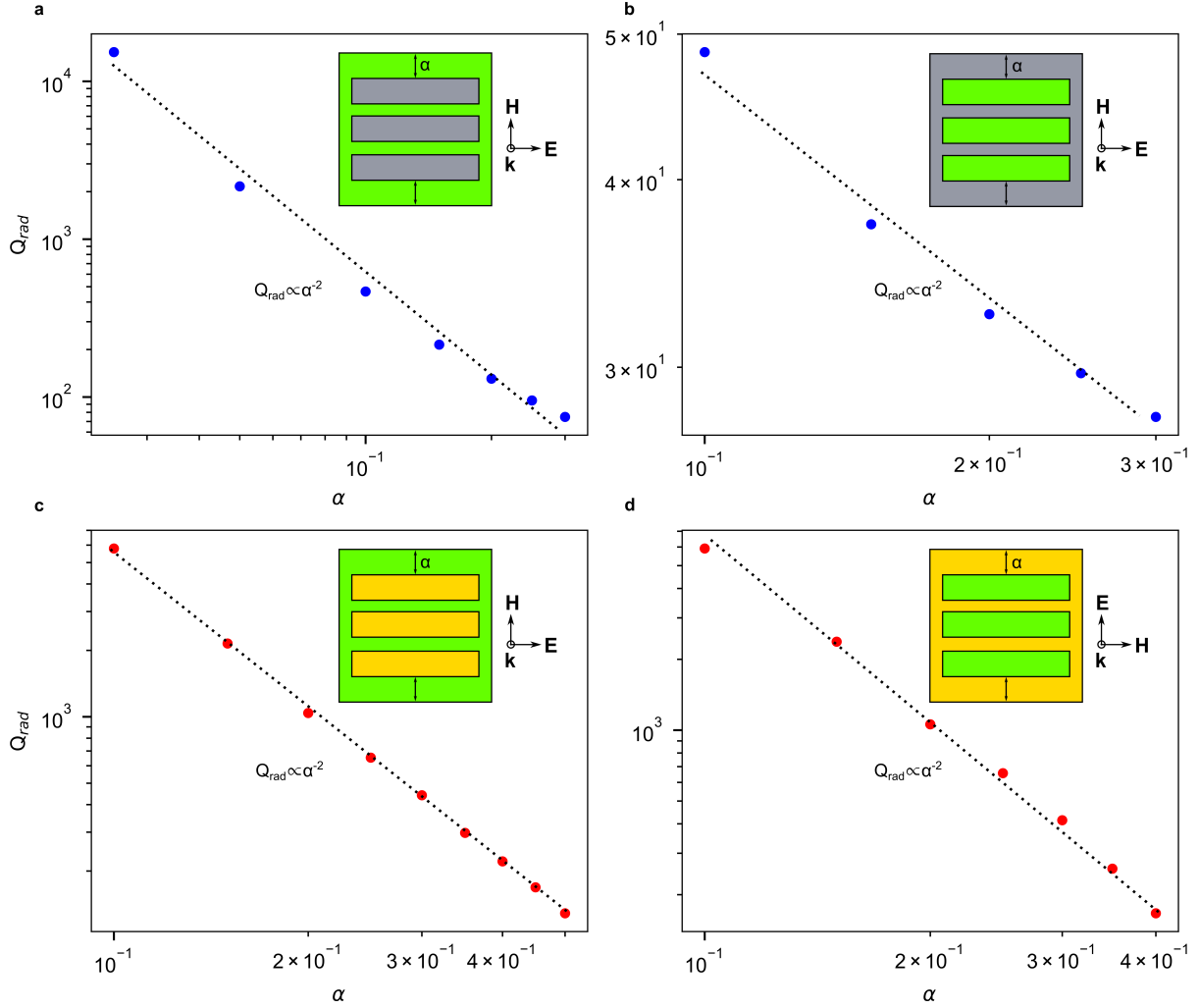
Figure 4.5. The inverse quadratic relationship between the radiative Q factor Q_{fac} and α for the (a) positive and (b) inverse Si and (c) positive and (b) inverse gold metasurfaces. Schematics of the respective unit cells and for the polarization of incident light are shown.

The angular dispersion of the main displacement-mediated q-BIC resonance emerging for $\Phi = 90°$ on the longer wavelength side of the RA was tracked (Figure 4.6a). Interestingly, there is a small resulting shift to shorter wavelengths in the resonance position of the displacement-mediated q-BIC resonance around $\lambda \approx 7.8$ μm for TM_x incident light for increasing polar angles θ. This shift is similar but smaller compared to silicon-tilted ellipses metasurfaces showing a resonance at around $\lambda \approx 6.6$ μm (Figure 4.6b). All-dielectric tilted ellipses produce a q-BIC mode for x-polarized incident light with an asymmetry parameter $\alpha = \sin(\varphi)$, where φ is the angle that the major axis of the ellipses make with the y-axis, also called tilt angle.[87] Almost mirroring across the $\theta = 0°$ axis in the angular dispersion plot (Figure 4.6a) the displacement-mediated q-BIC mode shifts to shorter wavelengths at a slightly faster rate with increasing θ for TE_y incident light until it meets its BIC point at around $\theta \approx 50°$.
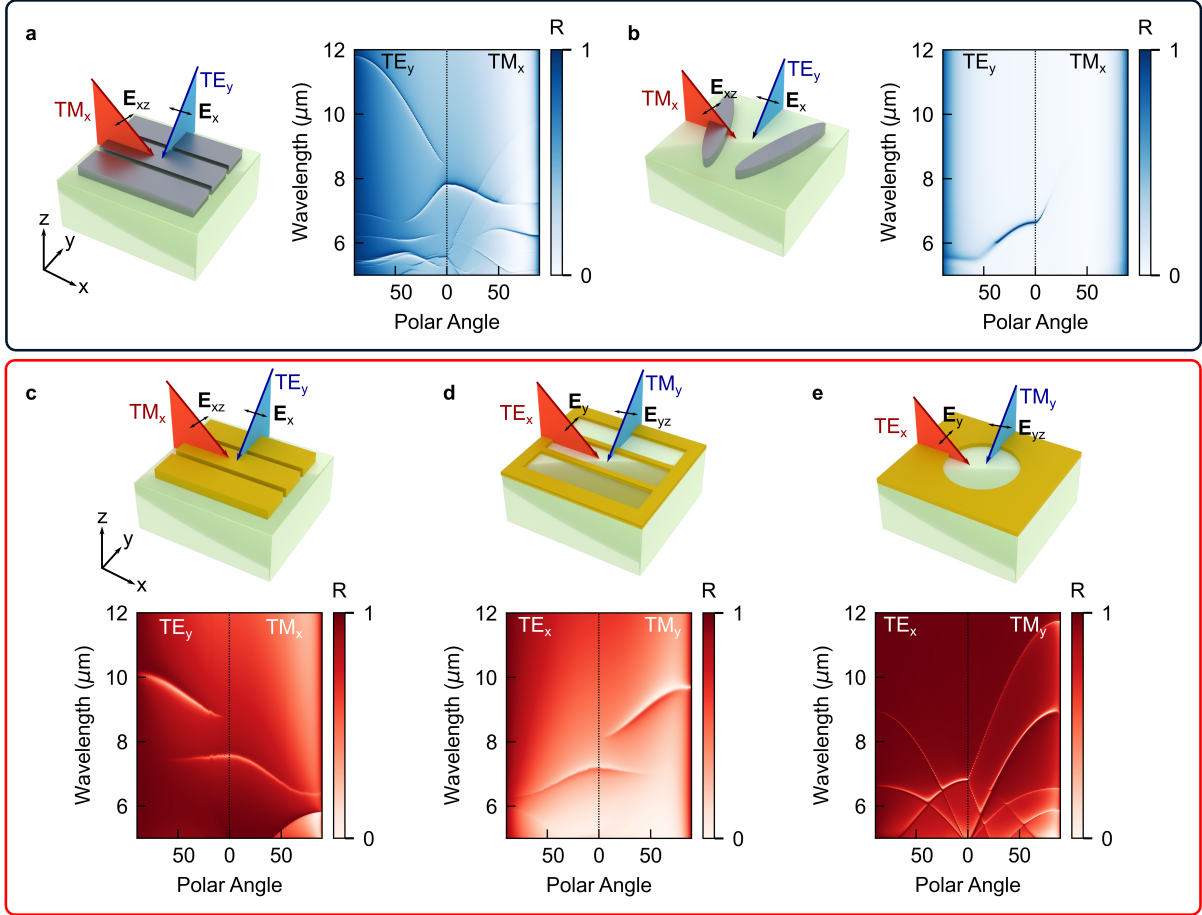
Figure 4.6. Angle sweeps of the displacement-mediated q-BIC and conventional rival metasurfaces. (a-e) Illustrative schematic and corresponding angular dispersion plots (polar angle vs reflectance) for s or TE and p or TM polarized light oriented to excite the primary resonance modes of the silicon (a) positive superlattice and (b) tilted ellipses metasurface, the gold (c) positive and (d) inverse superlattice and (d) nanohole metasurface. The polar angle was varied from 0° to 89°. The structural parameters underlying the polar angle dispersion plots are (a) $\alpha = 0.1$, $w_x = 3.85$ µm, $w_y = 1.1$ µm, $d_1 = d_3 = 275$ nm, $h = 650$ nm, (b) $\alpha = \sin(20°)$, $a = 3000$ nm, $b = 720$ nm, $p_x = 4650$ nm, $p_y = 3075$ nm, $h = 650$ nm, (c-d) $w_x = 2.31$ µm, $w_y = 660$ nm, $d_1 = d_3 = 165$ nm, $h = 100$ nm, and (e) $r = 1$ µm, $p_x = p_y = 5$ µm, $h = 100$ nm.

In contrast, the q-BIC mode of the silicon-tilted ellipses metasurface under TM$_x$ polarized incident light strongly shifts to longer wavelengths until it disappears (Figure 4.6b). Consequently, the relatively small and directionally similar (shift to shorter wavelengths) angular-driven shift in the TM$_x$ and TE$_y$ displacement-mediated q-BIC resonance position indicates a better performance under reflective objectives for the positive silicon superlattice over the silicon tilted ellipses metasurface. For the silicon superlattice, a second mode emerges for s polarized light with its BIC condition at $\theta = 0°$ (Figure 4.6a). This mode was numerically described by Shi et al.[38] Higher order modes on the shorter

wavelength side of the displacement-mediated q-BIC mode appear that are outside the scope of this article.

The angular behavior of the gold superlattice follows the same pattern as the silicon superlattice, although the q-BIC resonance shifts less strongly to shorter wavelengths. The resonance of the positive (Figure 4.6c) and inverse (Figure 4.6d) gold superlattice can be excited for TE_y and TM_x and TE_x and TM_y polarized light, respectively. It gradually disappears with increasing θ. As for the silicon counterpart, the gold superlattice features an emerging q-BIC resonance for $\theta \neq 0$ for TE_y and TM_y polarized incident light for its positive and inverse variations, respectively. Higher order modes of the gold superlattices are spectrally more separated.

The gold nanohole metasurface has a more complex band structure (Figure 4.6e). It produces a Fano resonance caused by multiple resonance interference at normal incidence illumination where the Q factor increases with decreasing radius r.[140] The degeneracy of the primary resonance mode at ca. 6.8 µm at normal incidence is lifted for $\theta \neq 0$ for TM polarized light. The upper branch strongly shifts to longer wavelengths due to the RA's similar spectral shift with increased incidence angles according to $\lambda_{RA} = p_{x,y}(\tilde{n} - \sin(\theta_{x,y}))$ (see Chapter 2),[150] where $\tilde{n}$ is the refractive index of the substrate and $p_x = p_y$ is the same for the nanohole metasurface. Under TE illumination the nanohole metasurface's resonance shifts to shorter wavelengths. Therefore, both versions of the gold superlattices are expected to show superior performance over the nanohole array when switching from a refractive to a reflective microscope objective or for other applications requiring angular-robust resonances.

4.1   Near-Normal Incidence Mid-IR Spectral Imaging

Mid-IR spectral imaging with a low numerical aperture (NA = 0.15) focusing objective (Figure 4.7a) of the positive silicon superlattice produced the predicted appearance of the displacement-mediated q-BIC resonance for $\alpha > 0$ (Figure 4.7b). The asymmetric line shape was predicted by the simulations (Figure 4.2c) but can be made more symmetric by appropriate parameter tuning. In contrast, the silicon tilted ellipses metasurface showed a symmetric q-BIC resonance emerging for $\alpha > 0$ with a low baseline reflectance of less than ca. 12% (Figure 4.7c). This result was expected as tilted ellipses are a staple q-BIC-based platform of choice for biosensing in the literature.[7,45]
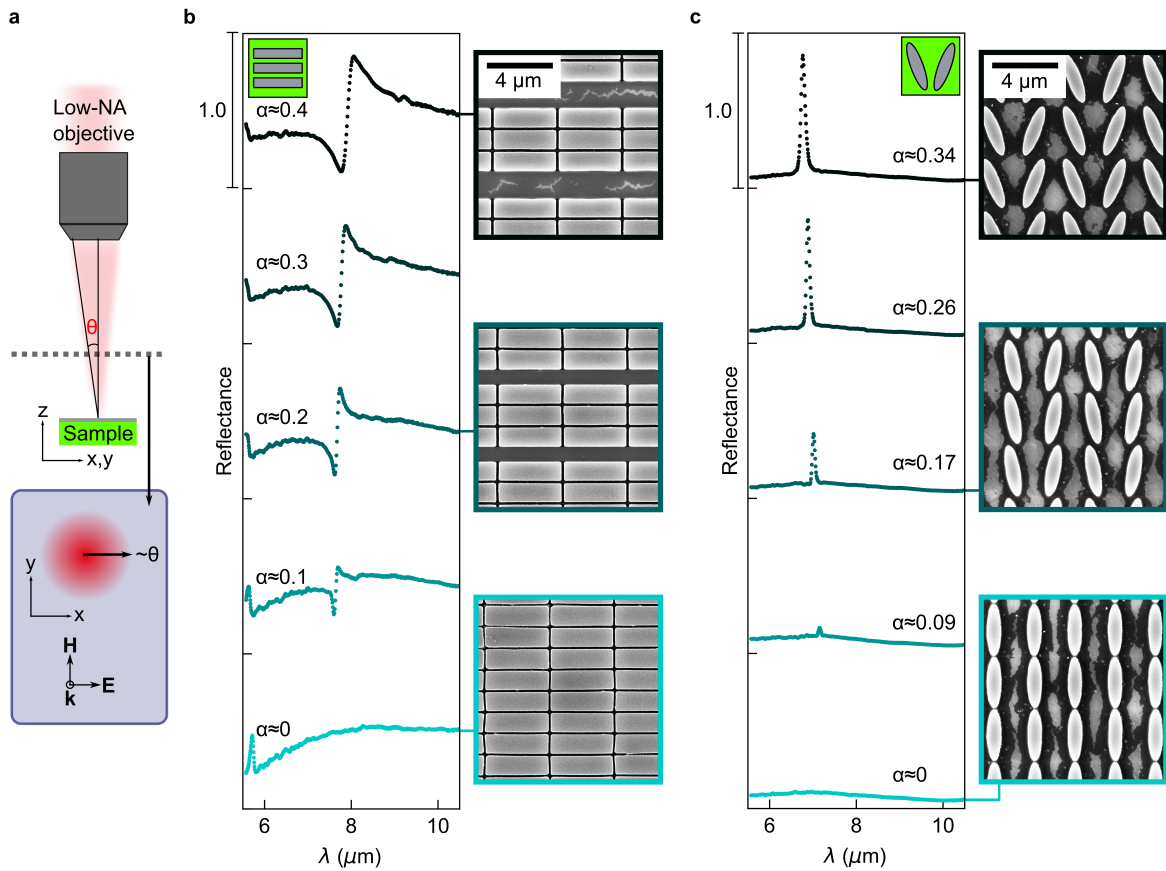
Figure 4.7. Near-normal incidence mid-IR spectral imaging of the all-dielectric superlattice and the tilted ellipses metasurface. (a) Schematic of the objective used and polarization of the incident light focused on the samples of the mid-IR spectral imaging microscope used for the following near-normal incidence optical measurements. (b) The measured reflectance spectra for the positive silicon superlattice for $\alpha \approx 0$, 0.1, 0.2, 0.3, 0.4 showing the displacement-mediated q-BIC resonance appearing for $\alpha > 0$. The adjacent scanning electron microscopy (SEM) images give the structural parameters of the structure as $w_x \approx 3.7$ µm, $w_y \approx 1.1$ µm, $d_1 \approx d_3 \approx 120$ nm, $h \approx 650$ nm. (c) The measured reflectance spectra for the silicon tilted ellipses metasurface for α varied from 0 to ca. 0.34. The adjacent SEM images give the structural parameters of the structure as $a \approx 3.3$ µm, $b \approx 760$ nm, $p_x \approx 2.41$ µm, $p_y \approx 3.12$ µm, $h \approx 650$ nm. Schematics of the relevant unit cell and the polarization of light are provided in the insets (b-c). The SEM images (a-b) show white discolorations between the resonator units which are due to a conducting layer (ESpacer 300Z) that was spin-coated on the all-dielectric metasurfaces to improve the image quality.
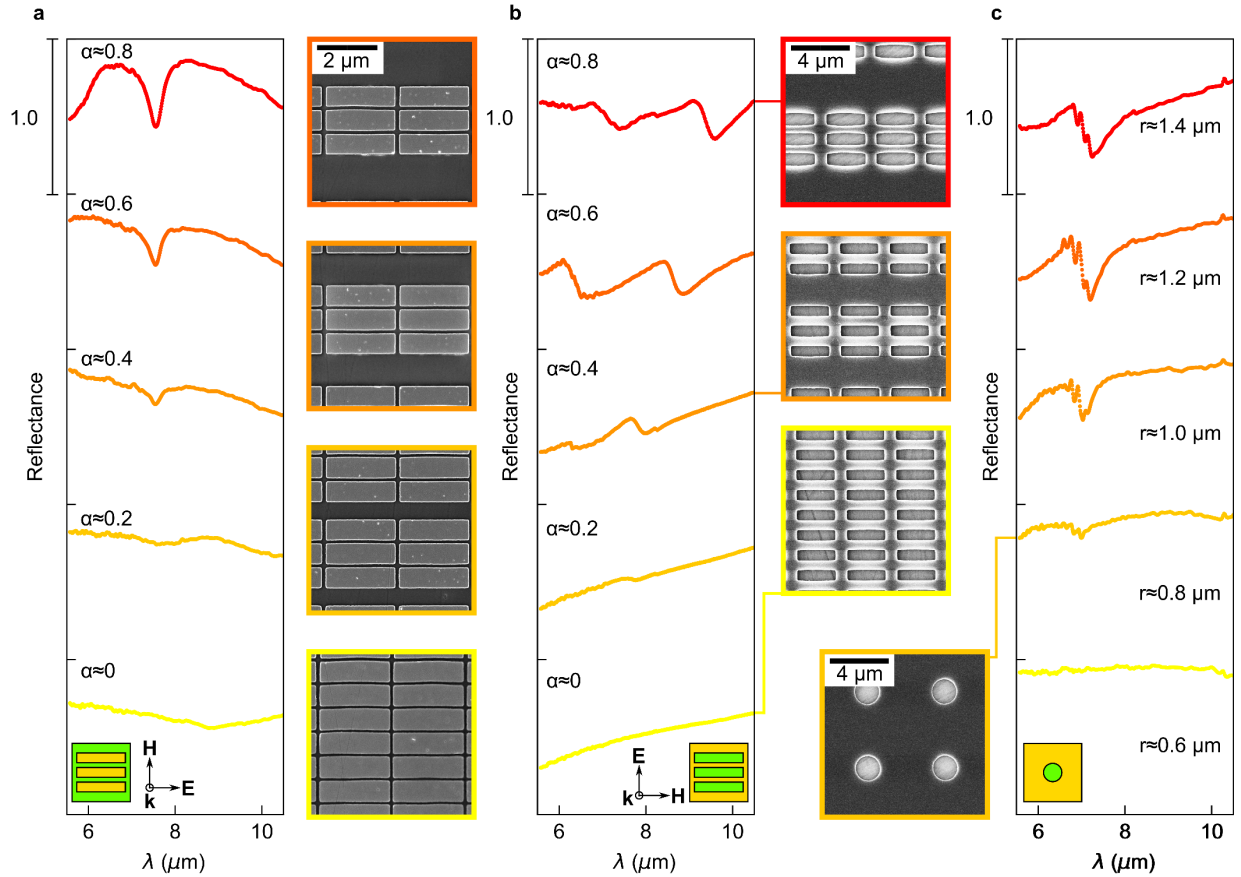
Figure 4.8. Near-normal incidence mid-IR spectral imaging of the gold superlattice and nanohole metasurfaces. (a-b) The measured reflectance spectra for the (a) positive and (b) inverse gold superlattice for $\alpha \approx$ 0, 0.2, 0.4, 0.6, 0.8 showing the displacement-mediated q-BIC resonance appearing for $\alpha > 0$. The adjacent SEM images provided the structural parameters of the structure as (a) $w_x \approx$ 2.3 µm, $w_y \approx$ 680 nm, $d_1 \approx d_3 \approx$ 100 nm, $h \approx$ 70 nm, and (b) $w_x \approx$ 2.5 µm, $w_y \approx$ 670 nm, $d_1 \approx$ 630 nm, $d_3 \approx$ 780 nm, $h \approx$ 30 nm. (c) The measured reflectance spectra and an SEM image for the gold nanohole metasurface for $r \approx$ 0.6, 0.8, 1, 1.2, 1.4 µm, $p_x \approx p_y \approx$ 5 µm, $h \approx$ 30 nm. Schematics of the relevant unit cell and the polarization of light are provided in the insets (a-c).

Near-normal incidence mid-IR reflectance spectra of the positive gold superlattice (Figure 4.8a) produced a displacement-mediated q-BIC resonance with a symmetric line profile emerging when $\alpha > 0$ as predicted by the numerical models (Figure 4.3b). As predicted by the simulations (Figure 4.3b, f), the q-BIC resonance of both the positive (Figure 4.8a) and inverse (Figure 4.8b) gold superlattice grew slower with α compared to the silicon version (Figure 4.7b). The asymmetric profile of the displacement-mediated q-BIC resonances for the inverse gold superlattice measured experimentally was expected from the simulations (Figure 4.3g). However, the overall quality of the resonances can be increased by improving the fabrication methods. Since the inverse structures were fabricated with a negative resist, which is significantly more sensitive to electron beam

exposure and strongly limits the achievable resolution, the distances between the inverse beams or slots had to be made very large, with $d_1 \approx 630$ nm and $d_3 \approx 780$ nm. Due to the larger gaps and unit cell, the RA was shifted to longer wavelengths cutting into and shifting the q-BIC resonance (Figure 4.8b). Moreover, negative resists suffer from a negatively impacting overcut profile that limited the inverse gold superlattice's metal film thickness to maximally 30 nm. In contrast, its positive complementary structure was made with a thickness of 70 nm, which allowed for stronger resonances.

The two gold superlattices produced cleaner line profiles compared with a gold nanohole metasurface (Figure 4.8c). The latter showed extra small modulations of the main resonance appearing at $\lambda \approx 7$ µm, which are explained by the numerically modeled angular dispersion plots (Figure 4.6e). Objectives with a non-zero NA take in light from a range of angles. The measured spectrum is formed by the average light power transmitted by the objective, which depends on the range of angles with which it can accept incoming light. Therefore, the measured spectrum can be predicted by averaging the spectra corresponding to the range of admissible angles and weighing them according to their relative contribution or power with which they pass the objective. Even for small-NA refractive objectives (Figure 4.8a), the measured spectrum is affected by the relative contributions it receives from light arriving across a small range of angles. The small modulations in the spectrum close to the resonance of the gold nanohole metasurface were caused by its main resonance at normal incidence splitting for small angular changes (Figure 4.8c).

4.1 Relative Change of Relevant Figures of Merit under a Reflective Objective

The numerical angular dispersion plots predicted a better performance for the superlattice compared to all-dielectric tilted ellipses or metal nanohole metasurfaces (Figure 4.6a-e). Using a reflective microscope objective mounted on a Fourier-transform IR (FTIR) spectrometer (Figure 4.9a), we measured the metasurfaces and compared the results with those measured under near-normal incidence (refractive objective, NA = 0.15) using mid-IR spectral imaging (Figure 5a).

To quantify the performance of the metasurfaces under a switch from a refractive to a reflective objective (NA = 0.4), we examine the change in relevant properties or parameters of metasurface-driven resonances, such as the resonance position λ_{res}, the modulation in reflection ΔR, the Q factor Q, and the ratio of coupling constants $\gamma_{ext}/\gamma_{int}$. Specifically, we introduce a relative change figure of merit (FOM) for the relevant resonance parameters as

$$C = \frac{x_2 - x_1}{x_1},\qquad\qquad\qquad (4.4)$$

where x_1 and x_2 are the resonance parameters under the refractive and reflective objectives, respectively.

With this procedure, the relative change of the resonance position ($C_{\lambda res}$), the Q factor (C_Q), the modulation in reflection ($C_{\Delta R}$), and the coupling condition ($C_{\gamma ext/\gamma int}$) can be quantified. The closer C is to zero, the better the angular-robust performance of the metasurface is when a switch from a refractive to a reflective objective is performed. To obtain a final performance metric $\bar{C}$ to compare the metasurfaces with each other, the relative change FOMs were averaged to a single value. The results are summarized in Table 4.1.

The silicon-based tilted ellipses metasurface demonstrated a strong and symmetric resonance at near-normal incidence illumination (Figure 4.7c), which was expected from the literature.[7,45,151] However, the signals strongly deteriorated when the switch from near-normal incidence illumination with a refractive objective to the reflective objective was performed (Figure 4.9b), as predicted by the numerical simulations (Figure 4.6b). The largest sources of deterioration in the resonance parameters came from the reduced modulation in reflection and $\gamma_{ext}/\gamma_{int}$, each at -0.93. The Q factor decreased at -0.6 and λ_{res} at -0.02. When the polarization was rotated by 90° no resonance was measured. The switch led to an overall performance $\bar{C}$ of -0.62. This means that by switching the objective from refractive to reflective, the performance of the resonance decreased by 62%. Conversely, 38% of the original resonance parameters remained intact during the increase in the range of incident angles. Consequently, we can quantitatively compare two metasurfaces by evaluating the percentage difference between their performances at maintaining their resonance during the objective switch 1-$\bar{C}$ according to equation (4.2).

In comparison, the positive silicon superlattice (Figure 4.9c) performed significantly better, with $\bar{C}$ at -0.43 compared to -0.62. Hence, we find that the silicon superlattice performed 50% better than the tilted ellipses. Furthermore, the Q factor decreased from 31 to 19 at -0.93. Similar to the ellipses, the largest and smallest sources of deterioration of the resonance parameters were $C_{\gamma ext/\gamma int}$ and $C_{\lambda res}$ with -0.73 and -0.02, respectively. The silicon superlattice resonance was more robust with respect to maintaining its modulation in reflectance, with $C_{\Delta R}$ at -0.57 compared to -0.93. Additionally, as predicted by the numerical angular dispersion plots (Figure 4.6a), a smaller second resonance appeared at longer wavelengths under the reflective objective. For y-polarized illumination, the resonance was still visible which can be attributed to an imperfect polarizer.
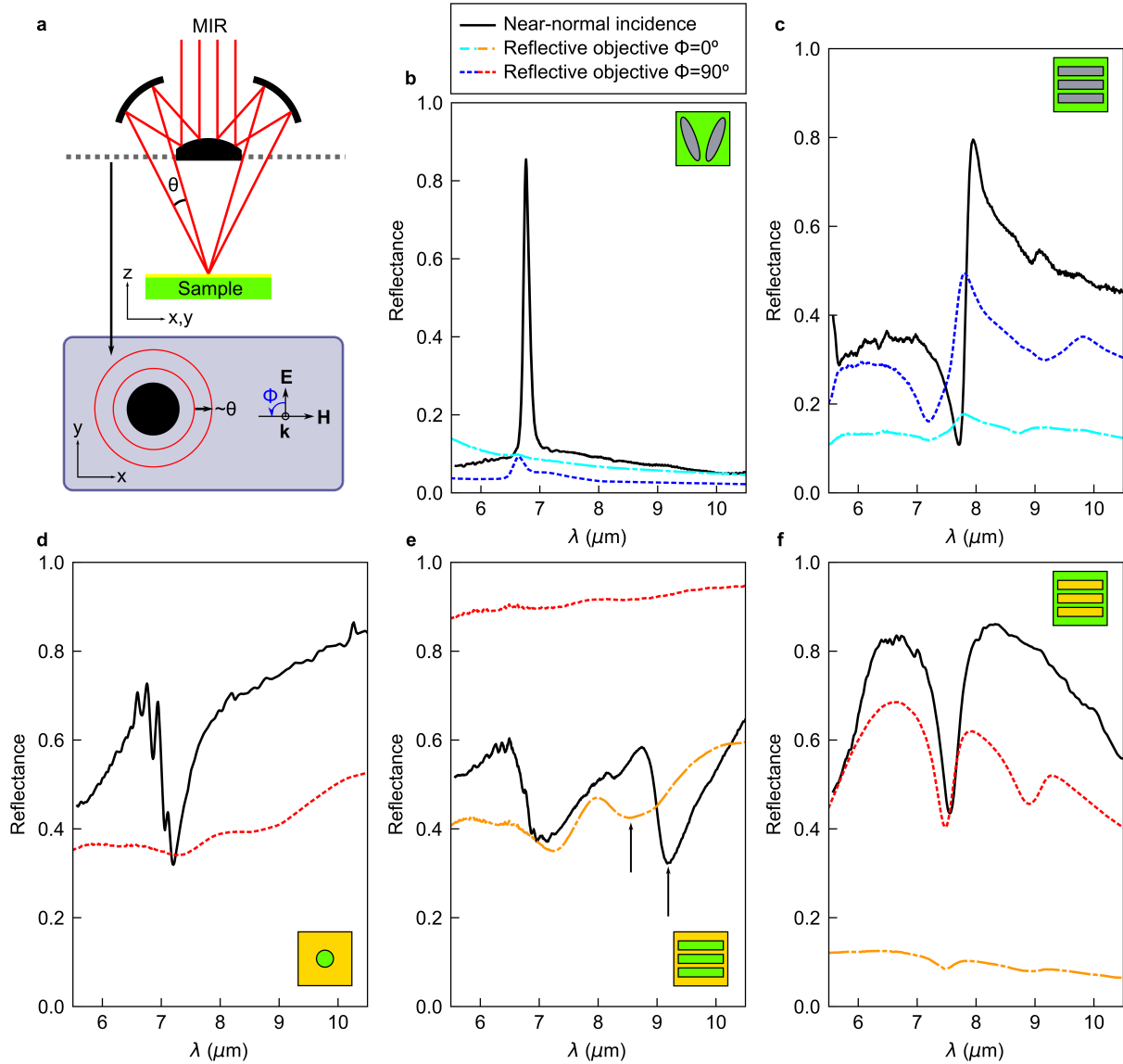
Figure 4.9. Comparison of the superlattice metasurfaces to traditional platforms under a reflective microscope objective. (a) Schematic of the reflective objective used in the Fourier-transform infrared spectrometer indicating the angular stability of the metasurfaces and the definition of the polarization of incident light. (b-f) Comparison of the effect on the metasurface-driven resonances in reflectance by moving from a near-normal incidence illumination polarized to excite the primary resonance (black line) to a reflective objective polarized with *Φ* = 0° (azure or orange dashed-dotted line) and 90° (blue or red dashed line). The metasurfaces shown are the silicon (b) tilted ellipses and (c) silicon superlattice, gold (d) nanohole, (e) inverse and (f) positive superlattice. The q-BIC resonance of the inverse gold superlattice (e) is indicated (black arrows). Schematics of the relevant unit cells are provided in the insets (b-f).

Table 4.1. Comparative summary of the results of the different metasurfaces under the refractive and reflective objectives. The final performance metric $\bar{C}$ for the different metasurfaces was highlighted by appropriately splitting the table.

Type	Objective	λ_{res} (nm)	~ΔR	Q	$\gamma_{ext}/\gamma_{int}$	$C_{\lambda res}$	$C_{\Delta R}$	C_Q	$C_{\gamma ext/\gamma int}$	$\bar{C}$
Tilted ellipses	Refractive	6764	0.75	65	2.08	-0.02	-0.93	-0.6	-0.93	-0.62
	Reflective	6615	0.05	26	0.14					
Silicon pos. superlattice	Refractive	7761	0.70	31	1.27	-0.02	-0.57	-0.39	-0.73	-0.43
	Reflective	7623	0.30	19	0.34					
Gold nanoholes	Refractive	7217	0.40	15	0.36	-1	-1	-1	-1	-1
	Reflective	-	0	0	0					
Gold inv. superlattice	Refractive	9050	0.30	24	0.38	-0.03	-0.67	-0.83	-0.37	-0.48
	Reflective	8742	0.10	4	0.24					
Gold pos. superlattice	Refractive	7576	0.40	20	0.23	-0.01	-0.38	-0.05	-0.22	-0.17
	Reflective	7474	0.25	19	0.18					

For the gold nanohole metasurface, switching from the refractive to the reflective objective had the biggest impact out of the structures analyzed here (Figure 4.9d). The metasurface-driven resonance that appeared under near-normal incidence vanished under the reflective objective. Hence, $\bar{C}$ was -1. Due to symmetry, the nanohole metasurface is invariant towards rotations of the polarization by 90° and only one polarization had to be measured. In contrast, the resonance of the inverse gold superlattice was measured with the reflective objective with *y*-polarized light (Figure 4.9e), with $\bar{C}$ at -0.48. Compared to the tilted ellipses, the inverse gold superlattice performed 37% better. Similarly to all other metasurfaces studied here, the smallest source of relative change in the resonance parameters of the inverse gold superlattice came from the change in resonance position, at -0.03. Unlike the other metasurfaces, the Q factor contributed to the deteriorating $\bar{C}$ the most with -0.83, where the Q factor decreased from 24 to 4.

The best results were achieved with the positive gold superlattice (Figure 4.9f). Under *x*-polarized illumination, the highly symmetric displacement-mediated q-BIC resonance only marginally deteriorated at -0.17, with the Q factor decreasing at only -0.05 from 20 to 19. The largest contribution to $\bar{C}$ was $C_{\Delta R}$ at -0.38, although the modulation in reflection with the reflective objective still exceeded 20%. The performance was 118%, 46%, and 59% better than the tilted ellipses, silicon superlattice, and gold inverse superlattice, respectively. A second resonance appeared at longer wavelengths, as predicted by the numerical angular dispersion plots (Figure 4.6c), similar to its silicon counterpart (Figure 4.9c).

The lower quality resonance of the inverse gold superlattice compared to its positive counterpart can be explained by fabrication limitations due to the negative resist, which required a thinner gold film to allow for a working lift-off and larger gaps between the slots and yielded rounder edges (Figure 4.7b, scanning electron microscopy (SEM) images). The quality of the resonance and its angular stability can be improved further by structural optimizations and superior fabrication (see previous discussion in Section 4.4). Higher Q factors can easily be achieved for all metasurfaces by decreasing α.

4.2   Conclusion

In summary, we have investigated positive and inverse, metal and all-dielectric superlattices and found that they produce displacement-mediated q-BIC resonances that can be described by a displacement asymmetry parameter α. Numerical models revealed that an inverse all-dielectric superlattice can produce a displacement-mediated q-BIC resonance under the same polarization as its positive counterpart. Furthermore, the numerical analysis revealed that Babinet's principle applies to the displacement-mediated q-BIC mode for metal superlattices. Numerical investigations of the angular dependence of the q-BIC resonance position successfully led to conclusions on the angular stability of the superlattice variations. The experimental realization of the superlattices confirmed that under near-normal incidence, a displacement-mediated q-BIC resonance emerges for $\alpha \neq 0$. The silicon positive, gold positive, and inverse superlattice metasurfaces were fabricated and tested under a reflective microscope objective and compared to two conventional platforms used for sensing: silicon-based tilted ellipses and gold nanohole metasurfaces. We quantified the performance of the metasurfaces by their relative change in their resonance parameters when the range of angles was increased by a switch in microscope objectives. This switch corresponds to an increase in the range of angles and a test of their angular robustness.

The strong performance of the fabricated superlattice metasurfaces compared to rivaling platforms was attributed to better angular robustness predicted by numerical angular dispersion plots. Despite the strong resonances of the silicon tilted ellipses and gold nanohole metasurfaces at near-normal incidence, their resonance parameters deteriorated at -0.62 and -1, respectively. The best performance was achieved with the positive gold superlattice, which performed 118%, 46%, and 59% better than the tilted ellipses, silicon superlattice, and gold inverse superlattice, respectively, and was characterized by a highly symmetric line shape. The numerical models showed that a maximum local electric near-field enhancement of ca. 378 can be achieved for $\alpha = 0.3$.

We anticipate that our experimental results will be useful for the wider research community working with hyper-spectral imaging, FTIR spectroscopy, and laser materials processing. Our results on the angular robustness of the superlattice predict that our

metasurfaces can be adopted by researchers working on conformal optical devices, displays, and photonic devices using focused light. In particular, we anticipate that the positive gold superlattice will be used in biospectroscopy and sensing due to the externalized and high electric near-field enhancement and symmetric resonance profile.

4.3 Experimental Section

4.3.1 Numerical Simulations

The simulations were performed in CST Studio Suite 2021 using the finite-element frequency-domain Maxwell solver. CaF_2 was simulated with a refractive index, n, of 1.35, the surrounding medium as air with n = 1, silicon with n = 3.48, and gold using the data given in Ref.[129] An impedance-matched open port with a perfectly matched layer introduced linearly polarized light at an azimuthal and polar angle (Figure 4.1b) through the air boundary into the system. The same port was placed on the opposite side to transmit the transmitted power. The reflectance was recorded by comparing the reflected power to the introduced power. The unit cell (Figure 4.1c) was defined and then simulated as an infinite periodic array via Floquet boundaries. A field monitor recorded the electric near-field distribution. The value of the highest field enhancement of the system was evaluated within the volume of the numerical model. To extract the radiative and total Q factor, central wavelength, and $\gamma_{ext}/\gamma_{int}$ of the resonances, the measured spectra were fitted in reflectance (Figure 4.9) using temporal coupled mode theory.[16]

4.3.2 Metasurface Fabrication

With CaF_2 as the substrate for all fabricated metasurfaces, there were two fabrication protocols, one for the positive and one for the inverse metasurfaces. The metasurfaces were made 100 by 100 μm^2 in size. The CaF_2 windows were cleaned in an acetone bath in an ultrasonic cleaner followed by oxygen plasma cleaning. For the gold-based metasurfaces, the substrate was directly spin coated with resist. For the silicon-based metasurfaces, first a 650 nm thick amorphous silicon layer was deposited at 180 °C via plasma-enhanced chemical vapor deposition. For the positive metasurfaces, the substrate was spin-coated with positive tone resist (PMMA 950 K A4), baked at 180 °C for 180 s, and with a conducting layer (ESpacer 300Z). For the inverse metasurfaces, the substrate was spin-coated first with an adhesion promoter (Surpass 4000), then with a layer of negative tone resist (ma-N 2403), which was baked at 100 °C for 60 s, and finally with a conducting layer (ESpacer 300Z).

The metasurface patterns were created by defining the unit cell and reproducing it in the *x* and *y*-directions. Then, the patterns were written via electron-beam lithography (Raith Eline Plus) with an acceleration voltage of 20 kV for the positive and 30 kV for the inverse metasurfaces, each with an aperture of 20 µm. Since the positive (inverse) metasurfaces were made with positive (negative) resist the different acceleration voltages were used to facilitate the lift-off procedure. The exposed resist was developed at room temperature in a 7:3 isopropanol:H_2O solution for 50 s for the positive, and in ma-D 525 for 70 s for the inverse metasurfaces.

For the gold-based metasurfaces, the patterned and developed surface was then coated with a titanium adhesion layer (2 nm at 0.4 Å s^{-1}) and a gold film (70 nm for the positive, 30 nm for the inverse metasurfaces at 1 Å s^{-1}) using electron-beam evaporation. Finally, an overnight lift-off at 80 °C in Microposit Remover 1165 for the positive, and mr-REM 700 for the inverse metasurfaces concluded the top-down fabrication process. Residual mr-REM 700 was removed in a water bath and by oxygen plasma cleaning.

For the silicon-based metasurfaces, an etching hard mask was created by electron beam evaporation of a 20 nm silicon dioxide layer and a 40 nm Cr layer onto the patterned resist, followed by a lift-off process as described above. The hard mask was then transferred to the Si film via inductively coupled reactive ion etching using chlorine and fluorine chemistry. After etching, the Cr and silicon dioxide layers were removed using a Cr wet etch and a final ICP-RIE step, respectively. All resists, solutions, and the conducting layer was from micro resist technology GmbH, Germany. Mid-IR Spectral Imaging with a Refractive Microscope Objective

The near-normal incidence optical responses of the fabricated metasurfaces (Figure 4.7 and Figure 4.8) was characterized with a mid-IR spectral imaging microscope Spero from Daylight Solutions Inc., USA, using a low-numerical aperture objective (NA = 0.15) with a low 4× magnification and a 2 mm^2 field of view. The Spero microscope is equipped with four tunable quantum cascade lasers continuously covering the mid-IR spectral range from 948 to 1800 cm^{-1} (5.56 to 10.5 µm) with a step size of 0.5 cm^{-1}. The measurements were conducted in reflection mode and normalized to the reflection signal of a plain gold mirror. The hyperspectral reflectance data corresponding to the metasurfaces were then averaged to reduce noise.

4.3.3   FTIR Imaging with a Reflective Microscope Objective

A VORTEX 80V FTIR (Bruker) paired with a HYPERION 3000 microscope (Bruker) was used to measure the spectra of the metasurfaces with a reflective microscope objective (Newport) with a NA = 0.4 and 15× magnification (Figure 4.9). The spectra were recorded with a liquid nitrogen-cooled mercury cadmium telluride detector in reflection mode. The range of polar angles taken in by the reflective objective was between 12° and 23.6°.

5. Improved In Situ Characterization of Electrochemical Interfaces Using Metasurface-Driven Surface-Enhanced IR Absorption Spectroscopy

The results presented in this chapter are published in Ref.:[55]

Berger, L. M., Duportal, M., Menezes, L. de S., Cortés, E., Maier, S. A., Tittl, A., Krischer, K., Improved In Situ Characterization of Electrochemical Interfaces Using Metasurface-Driven Surface-Enhanced IR Absorption Spectroscopy. *Adv. Funct. Mater.* 2023, 33, 2300411. https://doi.org/10.1002/adfm.202300411

As motivated in the introduction of this dissertation, electrochemical reactions underpin many technologies ubiquitous for a future carbon-zero world such as green-hydrogen generation for long-term sustainable energy storage[152] and CO_2 degradation to combat the current trends of climate change.[153] Unfortunately, in general, the monitoring, and therefore understanding, of many electrochemical reactions remains a challenge. In particular, resolving the electrochemical CO_2 reduction reaction with high efficiency, selectivity, and sensitivity remains an issue[50] especially due to the competition with the hydrogen evolution reaction at high current densities.[154] During the CO_2RR to desired carbon products, a compulsory step to the key intermediate CO is still not fully understood and requires further investigation.[155] In particular, the vibrational mode of top-site CO adsorption configurations on platinum (CO_{linear}) at 2033 cm^{-1} has proven difficult to detect by using conventional unstructured working electrodes in a three-electrode electrochemical cell.[156–160]

For the detection and characterization of molecules, optical spectroscopy, mass spectrometry, chromatography, and fluorescence microscopy are often used.[161] Provided that analyte concentrations are high enough, optical spectroscopy methods, such as IR or Raman spectroscopy, are highly advantageous because they allow for the retrieval of the spectral fingerprint of molecules via the detection of their rotational or vibrational modes. Unfortunately, during electrochemical reactions, most adsorbed intermediates occur in low concentrations and limit their detection with conventional spectroscopic techniques.[102,103] SEIRAS is a derivative technique from conventional

infrared spectroscopy based on the enhancement of the local electromagnetic near fields. To increase the sensitivity of SEIRAS during electrochemical reactions typically a rough metal surface is chosen to enhance the local electromagnetic near fields.[162] Rough and highly disordered metallic nm-sized edges coming from perforations and extrusions in the metallic film locally confine and enhance the electromagnetic near fields. Unfortunately, this approach is random, does not allow for spectral tailoring of plasmonic hotspots, and consequently generates a relatively weak electromagnetic near-field enhancement. Even after improvements in the sensitivity of SEIRAS using an ATR geometry,[102,103] the characterization of CO adsorption on catalysts is still hampered by weak signal traces.[118,163,164]

We overcome the challenge of detecting weak signal traces by taking inspiration from other fields of nanophotonics. In biomolecular sensing, a plethora of alternatives are used to improve molecular detection using controlled and tunable electromagnetic near-field enhancement via the excitation of resonances through tailored system parameters on the nanoscale. Examples are plasmonic nanoparticles, non-plasmonic nanogap dimers,[165] metasurfaces based on plasmonics[13] or exotic phenomena like quasi-bound states in the continuum,[7] waveguides[166] or 2D-integrated[167] platforms, among others.[168] Plasmonic-based sensors have become the method of choice in label-free detection of biomolecules. They can be used either as 1) refractive index sensors or 2) by coupling the resonances to the molecular modes and analysing the perturbation of the intensity either in reflection or transmission,[104] termed perturbed intensity sensing here.

In fact, some recent progress has been made to integrate plasmonic structures for refractive index sensing with electrochemistry.[104,169,170] There are also recent examples of plasmonic structures for perturbed intensity sensing for surface enhanced Raman spectroscopy used to monitor electrochemical reactions[171] or to study the mechanism of an electrocatalytic reaction.[172] Literature of plasmonic imaging provides other examples of electrochemical reactions of single nanoparticles,[173] plasmonics-supported and electrochemical monitoring of molecular interactions focused on fluorescence and confocal microscopy,[174,175] and plasmon-accelerated electrochemical reactions.[22,176] However, to the best of our knowledge, the integration of nanostructured metasurfaces for perturbed intensity sensing in SEIRAS has not been shown before in combination with electrochemistry.
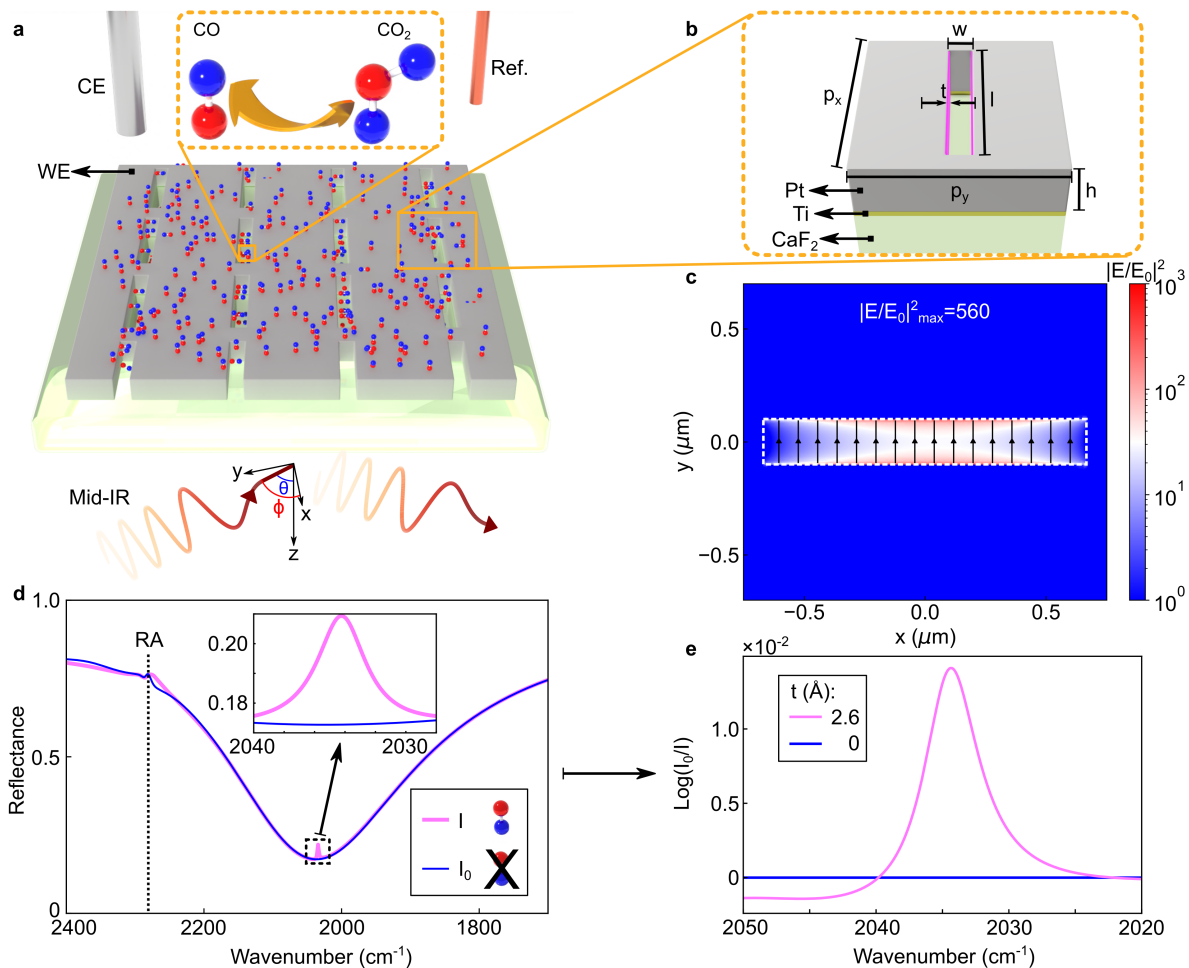
Figure 5.1. Numerical design of the catalytic metasurface. (a) Schematic for the Pt-based nano-slot metasurface for the in-situ integrated nanophotonic-electrochemical study of CO oxidation. As the potential between the working electrode (WE) and the reference electrode (Ref.) is swept the presence of adsorbed CO is monitored via the detection of the linear vibrational mode of CO at 2033 cm^{-1} with a FTIR spectrometer. The nano-slot metasurface enhances the electromagnetic near-fields of TE polarized light in an ATR configuration coming in at an azimuthal angle $\phi = 0°$ and polar angle $\theta = 72°$ w.r.t. the Pt film (*xy*-plane). (b) Sketch of the Pt on CaF$_2$ nano-slot unit cell. Two CO model layers were included parallel to the long edges of the slot (magenta) with dimensions $l \times h \times t$. A 1 nm thick Ti adhesion layer was used in the fabrication of the structures but is not considered in the numerical simulations due to its negligible effect on the resonance position. The geometrical parameters of the unit cell for (c), (d), (e) are $h = 30$ nm, $w = 200$ nm, $l = 1380$ nm, $p_y = 1400$ nm, $p_x = 1600$ nm. In (c) no CO model layer was included. (c) Electric near field intensity (taken at $h = 30$ nm) of the unit cell including arrows (black) showing the direction of the electric field inside the slot. The maximum near field intensity is 560. (d) The simulated reflectance spectrum of the metasurface with (pink) and without (blue) the CO model layer ($t = 5$ nm). The spectrum includes the Rayleigh anomaly (RA). (e) The differential absorbance with no CO (blue) compared to a 2.6 Å thick CO layer (pink) showing clearly visible absorption bands.

94

In this chapter, we experimentally demonstrate the in-situ detection of the CO vibrational mode at 2033 cm^{-1} emerging during the electrochemical conversion of CO into CO_2 using a platinum nano-slot metasurface on a CaF_2 substrate (Figure 5.1a). By coupling its resonance to the molecular vibrational mode and analyzing the perturbation of the intensity in reflection, the characteristic molecular signal traces were amplified. We perform SEIRAS in an ATR geometry to further improve the sensing performance while maintaining free accessibility of the electrode surface for reactants and products, and to minimize the contribution of the electrolyte to the IR spectrum.[102,103] We confirm the detection of adsorbed CO via the observation of the typical Stark shift and resolve a so far scarcely studied[177–179] effect due to the decrease of the CO coverage on the surface of platinum during the electrochemical oxidation. Furthermore, we show that a second peak emerges at 2086 cm^{-1}, which we attributed to the effect of the crystal orientation. Finally, we establish a methodology for designing similar nanophotonic-electrochemical platforms.

5.1 Results and Discussion

5.1.1 Description and Numerical Design of the Catalytic Metasurface

We started the implementation of our electrochemical sensing platform with the numerical design of the chosen nano-slot metasurface geometry. The structure consisted of a unit cell composed of a single slot in an otherwise connected platinum film submerged in water on CaF_2 (Figure 5.1b). The material of choice was platinum as it could fulfill all requirements, namely to function as a working electrode, support strong metasurface-driven resonances, and adsorb CO on its surface.[180] Moreover, Pt is a catalytic material for many reactions, making this platform very useful not only for the CO oxidation reaction but also for other reactions.

The decision on the inverse structure (i.e. the slots), was made to preserve a connected metallic film that could carry electrical current. As described in Section 2, the nano-slots feature nanorod-like resonances as predicted by Babinet's principle. Babinet's principle predicts that if a structure features a resonance under a certain polarization of the incident light its inverse structure will feature a similar resonance in reflection (transmission) under a 90-degree change in polarization as long as their geometrical parameters are the same.[52] Nano-slots can be tuned to enhance the electric and magnetic near-fields due to the excitation of a magnetic dipole aligned parallel to the long axis of the slot.[52] Consequently, a strong extended hot spot of the electric field is compressed inside the slot. Therefore, compared to resonant rod-type antennas, the inverse counterparts have

been shown to feature superior detection of molecular signal traces due to linearly instead of exponentially decaying electromagnetic near-fields and single hot spots being more extended.[52] The slots can only be excited with TE or *s* polarized light.[52]

Notably, we modeled adsorbed CO by including an artificially created material covering the inside walls parallel to the long axis of the slot. The permittivity of a material suffices to numerically model its interaction with light. Using the Lorentz oscillator model, the real and imaginary parts of the permittivity were as[181]

$$\varepsilon_r = 1 + \frac{\omega_p^2(\omega_0^2 - \omega^2)}{(\omega_0^2 - \omega^2)^2 + \gamma^2\omega^2} \tag{5.1}$$

$$\varepsilon_i = \frac{\gamma\omega_p^2\omega}{(\omega_0^2 - \omega^2)^2 + \gamma^2\omega^2}, \tag{5.2}$$

respectively, where ω_p is analogous to the plasma frequency in the Drude-Sommerfeld model, ω_0 is the frequency of the absorption band, ω is the frequency, and γ is the damping constant. We modified the baseline of ε_r to be around 1.33^2, which is the refractive index squared used for the surrounding medium (water) due to a negligible shift in the refractive index due to CO.[182] To model CO_{linear} at 2033 cm^{-1} the parameters used were $\omega_p^2 = 1 \times 10^{24}$ s^{-2}, $\omega_0 = 60.95 \times 10^{12}$ s^{-1} (corresponding to 2033 cm^{-1}), and $\gamma = 1 \times 10^{11}$ s^{-1} (Figure 5.2).
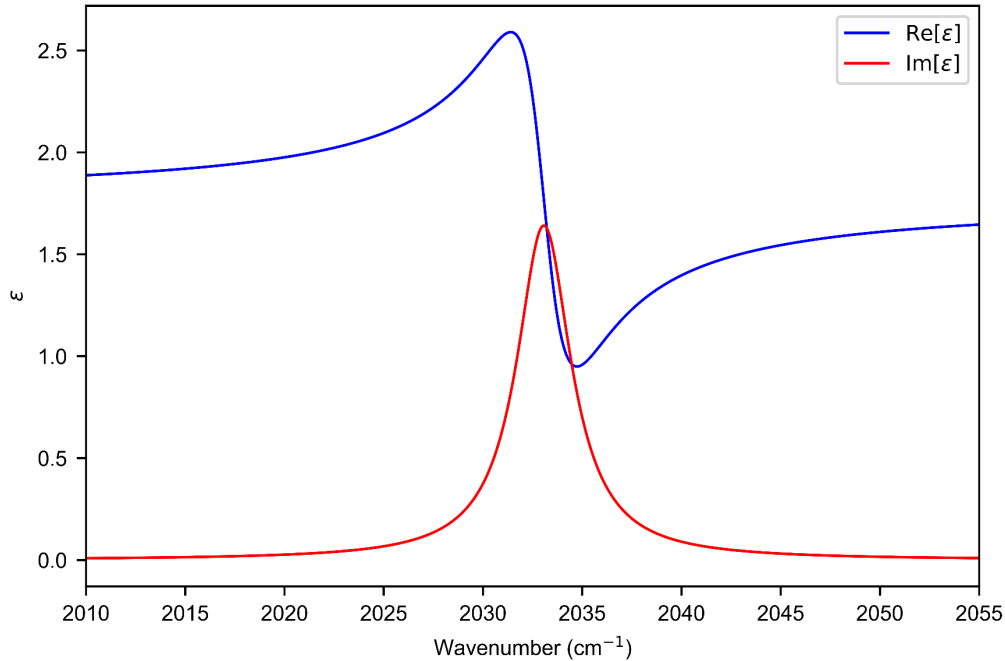

Figure 5.2. The real (blue) and imaginary (red) parts of the permittivity of the artificial material modeled to represent top-site adsorbed CO on platinum.

The choice of the parameters of the unit cell was guided by Huck et al.[52] and modified in accordance with fabrication constraints. Huck et al.[52] optimized a gold nano-slot metasurface in the NIR for normal incidence illumination in air for high-Q factors and electric near fields. The Q factor relates the initial energy stored in a resonator to the energy dissipated in one radian of the cycle of oscillation.[183]

Based on our simulations, the nano-slot metasurface achieved a resonance with a modulation in the absorbance of over 82% and a Q factor of 6.3. Furthermore, the metasurface numerically exhibited an electric near-field enhancement $|E/E_0|^2$ of 560. This value can be increased in future experiments by decreasing the width of the slots[52] but was limited here due to fabrication constraints. The maximum electric near-field enhancement occurred inside the slots close to the faces parallel to its long axis (Figure 5.1c), with its electric field pointing orthogonally to it. The parameters of the unit cell of the nano-slot metasurface are defined in Figure 5.1b, where p_x and p_y are the unit cell lengths in x and y. l, w, and h are respectively the length, width, and height of the slot, and t is the thickness of the molecular layer used to model adsorbed CO. The gap g between two slots in x is $g = p_x - l$. Huck et al.[52] found that the highest Q factor and electric near field enhancement occurs when w is small, $p_y = g = \lambda_{res}/2$, where λ_{res} is the central wavelength of the resonance. However, to satisfy the experimental conditions the nano-slot metasurface was simulated in water instead of air and for an angle of incidence $\theta = 72°$.

Under these conditions, tuning the resonance to 2033 cm^{-1} $\approx$ 4.92 µm led to the appearance of a Rayleigh anomaly such that $\lambda_{RA} > \lambda_{res}$, where λ_{RA} is the central wavelength of the RA. As discussed in Chapter 2, the RA is a phenomenon associated with light being diffracted parallel to the surface of a periodic structure.[147] When $\lambda_{RA} > \lambda_{res}$, the resonance lifetime and electric near-field enhancement are strongly reduced.[74] Consequently, a metasurface where $\lambda_{RA} > \lambda_{res}$ exhibits poor sensing performance. For this reason, g was reduced to 220 nm to push the resonance on the evanescent side of the RA (Figure 5.1d).

As discussed in Chapter 2, in coupled-resonator systems, the excitation efficiency of a resonator significantly depends on the ratio of its losses to external radiation γ_{ext}, i.e. light scattering, and intrinsic material absorption γ_{int}, which strongly depends on the system design and parameters chosen[42]. When $\gamma_{ext} \sim \gamma_{int}$, the system is critically coupled and the second oscillator will result in a dip in the absorption cross-section. SEIRAS performance can be maximized by utilizing a system that is close to the critical coupling condition.[42,44] The absorbance spectrum was fitted using temporal coupled-mode theory (see Section 2), showing that the nano-slot metasurface with the parameters given above is near the critical-coupling condition with $\gamma_{ext}/\gamma_{int} \approx 1.2$.
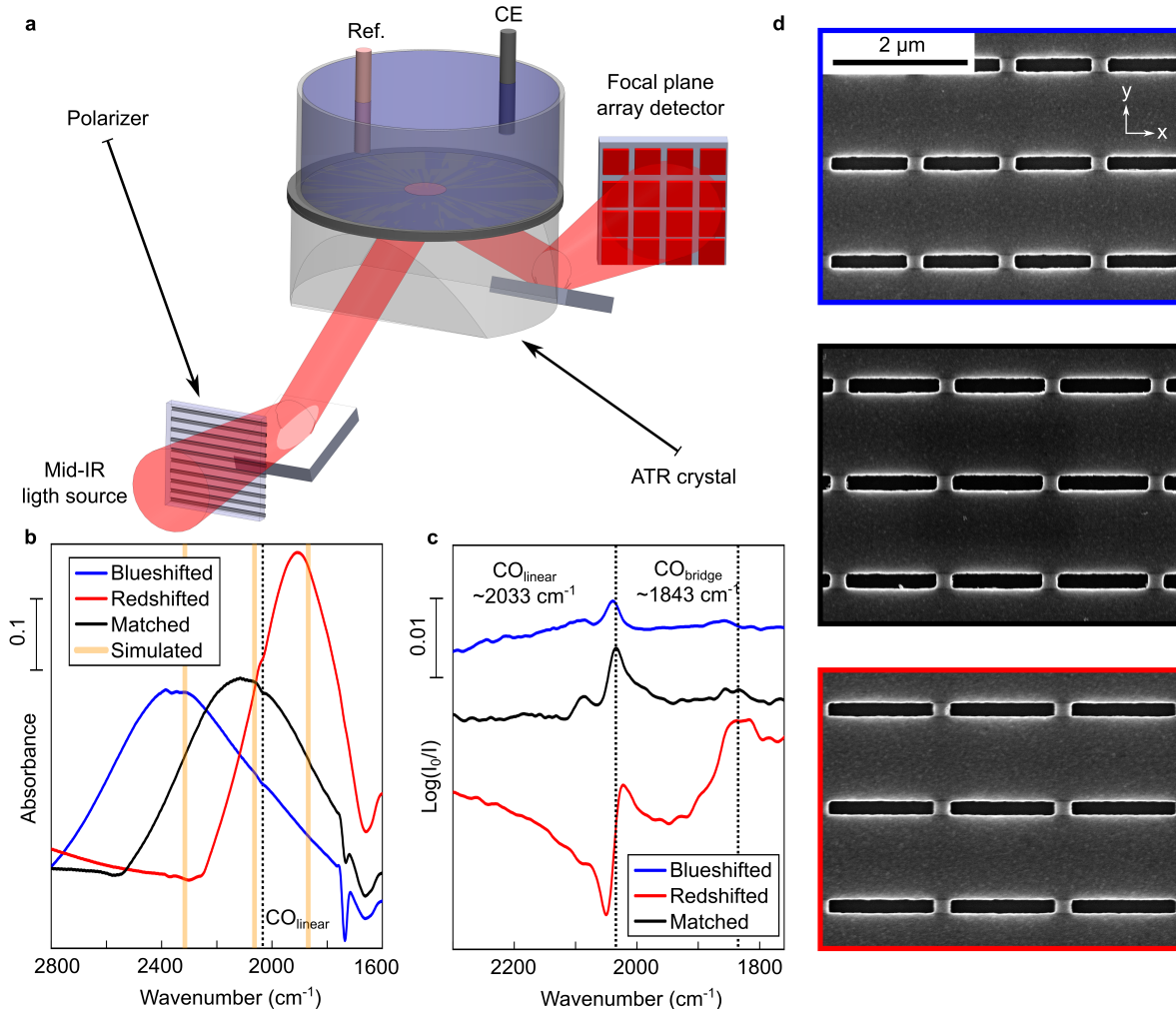
Figure 5.3. Testing the nanophotonic-electrochemical platform. (a) A schematic showing the experimental setup used to perform SEIRAS in an ATR geometry. A continuous mid-IR collimated linearly polarized light source illuminated the nano-slot metasurface from below at an angle of ca. 72°. A focal plane detector array was used to collect the signal. (b) Experimental absorbance spectra of three Pt nano-slot metasurfaces in CO-saturated 0.5M K_2CO_3 aqueous electrolyte with resonance positions around the ideal position for CO_{linear} with slot lengths l 1.33 µm (black, ideal) and two detuned resonance positions with slots length of 1.13 µm (blue) and 1.53 µm (red). The other parameters are h = 30 nm, w = 200 nm, p_y = 1440 nm, and $g = p_x - l$ = 220 nm. The resonance position of CO_{linear} is indicated by the black-dashed line. The numerically modeled resonance positions at 2312 cm^{-1}, 2066 cm^{-1}, and 1876 cm^{-1} (yellow) are shown for comparison. (c) The differential absorbance of the CO signal after baseline correction for the blueshifted, matched, and redshifted resonances. (d) Scanning electron microscopy images corresponding to the nano-slot metasurfaces used in (b) and (c).

Thus, when the resonance overlapped with the vibrational mode of adsorbed CO at 2033 cm^{-1}, the coupling between the two resonators led to a small peak in the reflectance

98

spectrum (Figure 5.1d). t was set to 5 nm as an example to visualize the modulation of the resonance. The differential absorbance, defined as $\log(I_0/I)$, where I and I_0 are the reflectance measured with and without a CO model molecular layer, respectively (Figure 5.1c), was used to extract the signal traces of adsorbed CO. To obtain a more realistic expectation for the differential absorbance resulting from adsorbed CO on the nano-slot metasurface, the CO layer was modeled with a thickness of 2.6 Å (Figure 5.1e) in agreement with the literature.[184]

5.1.2   Metasurface Characterization

First, the effect of the metasurface-driven resonance position on the coupling with CO_{linear} was studied in an ATR geometry using a focal plane array detector (Figure 5.3a). To test our nanophotonic-electrochemical platform, we first tuned the resonance position to match CO_{linear} in 0.5M K_2CO_3 saturated with carbon monoxide. Then, we detuned the resonance to the blue and red spectral regions by decreasing and increasing the slot length l by 200 nm from 1.33 µm, respectively (Figure 5.3b). There is good agreement between the numerically and experimentally obtained resonance positions, with a discrepancy of less than 40 cm^{-1}. As predicted by the simulations, a dip was observed in the resonance lineshape attributed to CO_{linear}. The Q factor of the experimentally measured metasurface-driven resonance matching CO_{linear} (Figure 5.3b) was 2.9, which was slightly lower than the simulated value. The smaller experimental Q factor was due to fabrication imperfections compared to the ideal numerical model.[151] Following these results, slots with a length of ca. 1.33 µm were found to match CO_{linear} on platinum. According to the literature,[156–160,185] CO_{linear} was expected to be spectrally located between 2020 cm^{-1} and 2080 cm^{-1}. Based on our experiments, CO_{linear} was located at 2033 cm^{-1}.

The differential absorbance highlights a more intense and well-defined CO_{linear} signal for the sample that had the best spectral overlap (Figure 5.3c). Two peaks were observed at 2033 and 2086 cm^{-1}. The CO signals had a Fano-type line shape due to the narrow discrete CO_{linear} interfering with the broad spectral line of the metasurface-driven resonance.[186] The redshifted sample yielded a highly asymmetric CO signal due to the strong off-resonance coupling between the resonance and CO_{linear}.[187] In addition, the redshifted sample presented a strong peak around 1843 cm^{-1}, which was attributed to a second configuration of adsorption, the CO bridge (CO_{bridge}).[156,157,159,185] The scanning electron microscopy images showed good quality in the fabrication of the nanostructures (Figure 5.3d). For the next part of this work, the electrochemical behavior of the sample with matching spectral overlap of its resonance with CO_{linear} is studied.
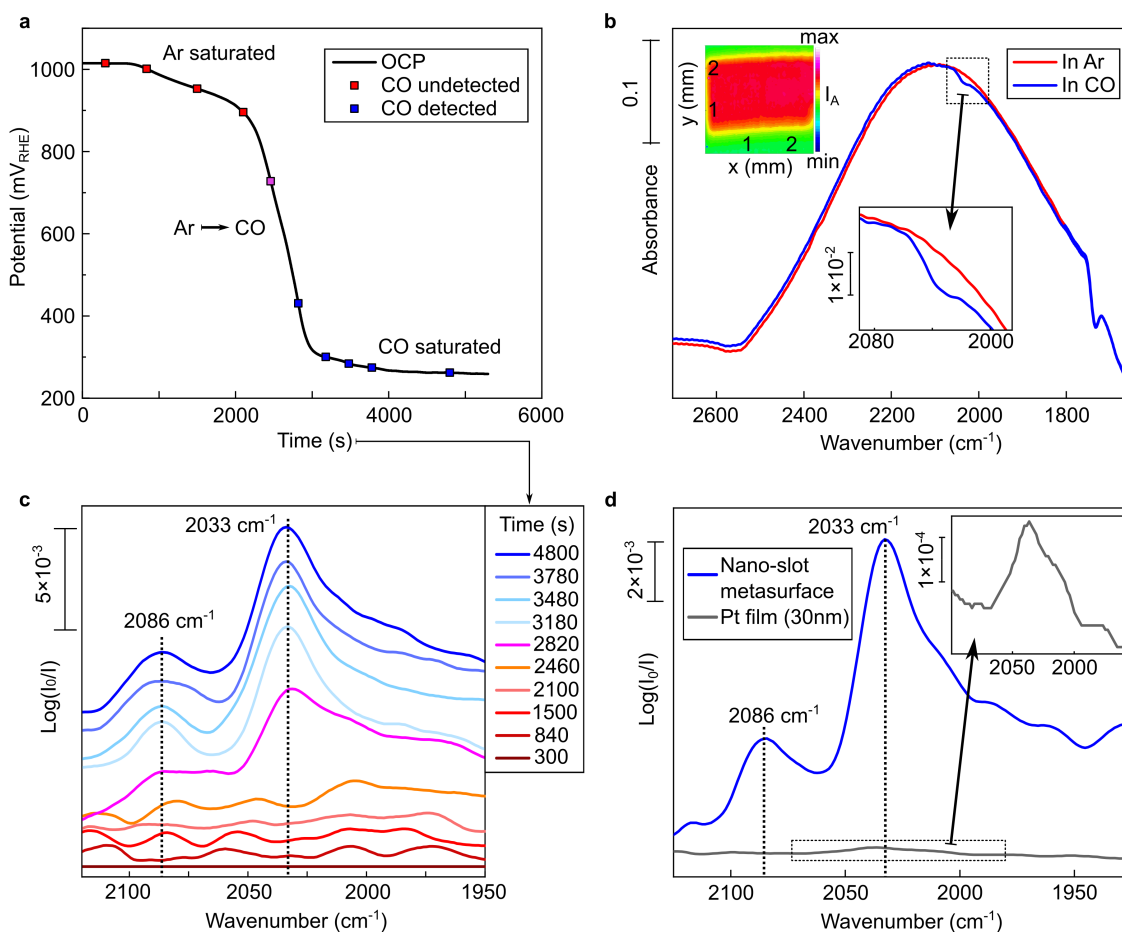
Figure 5.4. Electrochemical and spectroscopic response of the nanophotonic platform at the OCP during a gas transition from an Ar-saturated electrolyte to a CO-saturated one. (a) The evolution of the OCP of the platinum nano-slot metasurface during the transition from an argon-saturated ($Ar^{sat} \approx 1000$ mV$_{RHE}$) to a CO-saturated electrolyte ($CO^{sat} \approx 260$ mV$_{RHE}$). (b) FTIR spectra taken with *s* polarized light of the Pt nano-slot metasurface/electrolyte interface in Ar^{sat} and CO^{sat}. The heat map represents the integrated area below the resonance line between 2600 and 1800 cm^{-1} collected by an array of 64 by 64 detectors. (c) The evolution of the differential absorbance CO$_{linear}$ peaks during the CO bubbling process. (d) Comparison of CO$_{linear}$ signals obtained in CO^{sat} after 80 min of CO bubbling with a pure Pt layer (*p* polarized light) and with the nanophotonic-electrochemical platform (*s* polarized light).

5.1.3 CO Adsorption at the Open Circuit Potential

Here, we follow in situ the CO adsorption during the saturation of an electrolyte at open circuit potential and characterize the CO adsorption by performing SEIRAS concurrently

with electrochemical cyclic voltammetry. The transition from the argon-saturated (Ar^{sat}) to the CO-saturated (CO^{sat}) electrolyte is accompanied by a shift of the OCP due to a change of the equilibrium determining redox reaction (Figure 5.4a). At the equilibrium potential of the Ar-saturated electrolyte (ca. 1000 mV_{RHE}) CO is oxidized and the OCP drops towards negative values, where CO adsorbs on the Pt surface.

The SEIRAS measurements were taken in 0.5M K_2CO_3 with and without CO using *s* polarized light (Figure 5.4b). Looking at the differential absorbance (Figure 5.4c), a distortion of the baseline appeared at 2460 seconds (725 mV_{RHE}). Then, after approximately 2800 seconds (430 mV_{RHE}) two clearly distinguishable CO_{linear} peaks emerged. These peaks became more discernible with time as the coverage of adsorbed CO increased. As the intensity of the peaks stabilized, the maximum coverage of CO was reached.

The CO signal obtained with the nano-slot metasurface compared to that obtained with a pure platinum layer (30 nm) at the OCP was increased by an estimated factor of 27 (Figure 5.4d). Both samples were evaporated simultaneously. This ensured that both systems had the same material properties, such as surface roughness. For this reason, the 27-fold difference between the signals obtained with the two systems can be directly linked to the metasurfaces-driven enhancement provided by nanostructuring the surface of the working electrode.

For adsorbed CO to interact with incident light, the orientation of the transition dipole moment of the CO vibrational mode relative to the electric field component needed to be non-zero.[188] Consequently, only the (interior) side walls parallel to the long axis of the slots can be considered active, representing a ratio of active to total surface of 3.6% compared to a smooth platinum layer. This led to an experimentally determined local signal enhancement of above 700.

The second peak at 2086 cm^{-1} was only observed using the nano-slot metasurface. The most likely explanation could be that the higher resolution achieved with the nano-slot metasurface allowed for the deconvolution of this peak from the background, which was not possible in previous architectures based on a continuous Pt film. According to the literature, several possibilities exist. The first assumption is that CO could have adsorbed on different crystal orientations with different binding energies.[185,189] As reported by Cuesta et al.,[189] an adsorption on Pt(111) single crystals was found at around 2070 cm^{-1},[177,189,190] while CO adsorbed on Pt(100) electrodes was detected between 2027 cm^{-1} [191,192] and 2050 cm^{-1}.[189,193] These two values are in good agreement with the ones observed here (2086 cm^{-1} and 2033 cm^{-1}). Another possibility is the adsorption of CO on terraces (higher frequency band at 2086 cm^{-1}), steps, and defects (lower frequency band at 2033 cm^{-1}).[156,157,194]

5.1.4 CO oxidation on platinum

The behavior of the nano-slot metasurface was evaluated during the electrochemical oxidation of carbon monoxide using electrochemical cyclic voltammetry. The anodic scan in CO-saturated electrolyte presented an initial state with a low current (Figure 5.5a, black line). When an applied potential of around 550 mV_{RHE} was reached, the current density plateaued at around +25 $\mu A.cm^{-2}$, which was attributed to CO oxidation and can be written as[195,196]

$$H_2O + * \rightarrow OH_{ad} + H^+ + e^-, \qquad (5.3)$$

$$CO_{ad} + OH_{ad} \rightarrow CO_2 + H^+ + e^-, \qquad (5.4)$$
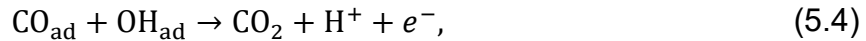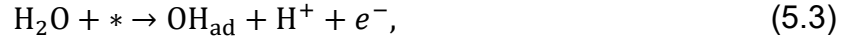
where * is a free adsorption site on platinum, and CO_{ad} and OH_{ad} correspond to adsorbed CO and OH on Pt, respectively. At approximately 1150 mV_{RHE}, the current density began to decrease. The origin of this decrease is still debated in the literature. One explanation attributes the decreasing current density to the competing adsorption of CO and OH on the Pt surface at higher potentials.[197] Another possibility is that the formation of a thin oxide or hydroxide Pt layer prevents the oxidation of CO. The latter assumption is supported by the reduction dip (from 860 to 620 mV_{RHE}) of platinum in the argon-saturated electrolyte (Figure 5.5a-b). The behavior of the cathodic scan was similar, except that the onset of CO oxidation was shifted to more negative potentials resulting in a hysteresis. Moreover, a shift in the onset of the hydrogen evolution reaction in Ar^{sat} and CO^{sat} electrolytes was observed, highlighting the poisoning behavior of adsorbed CO on the platinum surface.[198]

Similarly to our FTIR measurements in CO^{sat} electrolyte under OCP (Figure 5.4c), two CO_{linear} peaks were also found during the electrochemical potential sweeps (Figure 5.5c-d). There was a spectral shift during the anodic and cathodic scan (between 50 and 550 mV_{RHE}), which was attributed to either a higher π-back-donation from the metal to CO[179,199] and/or to the Stark shift. A Stark shift results from the interactions between the surface electric field and the dipole moment of the adsorbates.[199–201] During the anodic scan (Figure 5.5e), the most intense peak showed a blueshift of 53 $cm^{-1}.V^{-1}$ in agreement with the literature.[177–179,200,202] The second peak showed a blueshift of 33 $cm^{-1}.V^{-1}$. Between 650 and 750 mV_{RHE} a redshift was observed, which was not well documented in the literature.[178,194,199,203] The redshift was attributed to a decrease of the CO coverage due to its oxidation into CO_2, decreasing the dipole-dipole interactions.[194,204] The observation of the coverage effect was possible here due to the high resolution reached with the nano-slot metasurface. It was not resolved with a continuous platinum film. At higher anodic potentials, the CO_{linear} peaks disappeared due to CO oxidation.
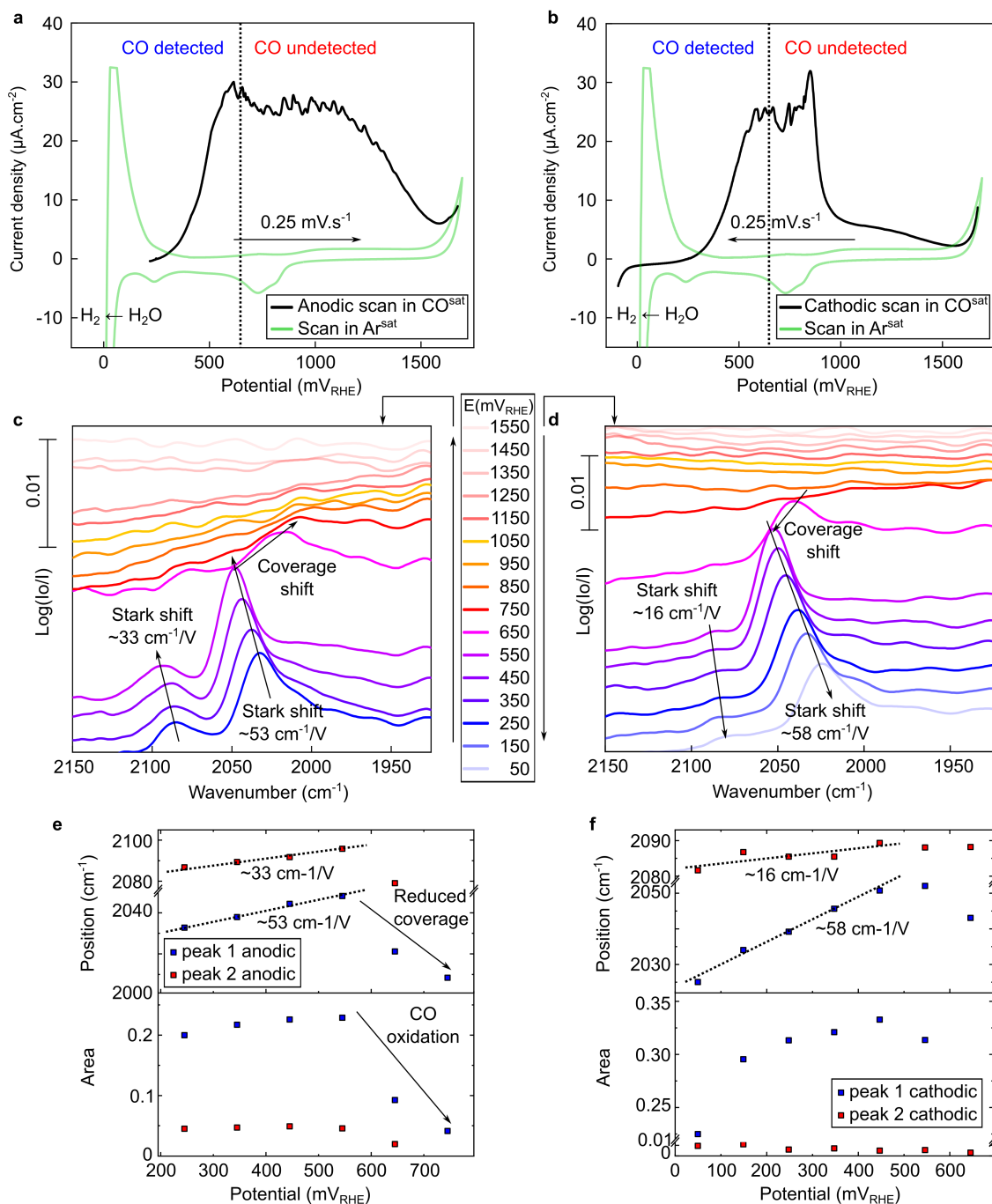
Figure 5.5. The behavior of the Pt nano-slot metasurface during cyclic voltammetry in 0.5M K_2CO_3 saturated with CO at 0.25 mV.s^{-1}. Evolution of the current density with the potential during the (a) anodic (from OCP to 1700 mV$_{RHE}$) and (b) cathodic (from 1700 mV$_{RHE}$ to -100 mV$_{RHE}$) scan in CO^{sat} electrolyte (black line). For comparison, the green line depicts CVs in an Ar^{sat} electrolyte. Evolution of SEIRAS spectra using *s* polarized light with the (c) anodic and (d) cathodic scans acquired every 100 mV. Evolution of the position and area of the CO$_{linear}$ peak during the (e) anodic and (f) cathodic scans.

103

Since CO only oxidizes at the Pt surface, the electrolyte remained saturated with CO, highlighting that there was no contribution of dissolved CO to the infrared signal. During the anodic scan, there was a slight increase in the area of the first peak (~2033 cm^{-1}), while the area of the second peak slightly decreased. This behavior could be explained by a surface migration of adsorbed CO to a more stable position.[158,178,179,191] Alternatively, the reconstruction or roughening of the Pt surface with electrical polarization[205,206] could have led to a modification of the surface microstructure and CO adsorption energy.[207] Looking at the spectra obtained during the cathodic scan (Figure 5.5f), the second peak (~2086 cm^{-1}) almost disappeared. This supports the assumption that the cause was the platinum surface modification at high-applied potentials. At high cathodic potentials (150 to 50 mV$_{RHE}$), a decrease of the CO peak was observed and attributed to the hydrogen evolution reaction,[202] indicating that the adsorption of hydrogen displaces adsorbed CO.

5.2   Conclusion

To the best of our knowledge, we have developed the first hybrid nanophotonic-electrochemical platform for SEIRAS based on a platinum nano-slot metasurface. The resonance of the metasurface was numerically modeled, giving a maximum electric near-field intensity enhancement of 560. The resonance was tuned to couple with and enhance the CO vibrational mode at 2033 cm^{-1}. The principle behind the sensing improvement due to the electric near-field enhancement was tested by fabricating on-resonance and detuned metasurfaces and carefully analyzing the resonance. The numerical simulations and SEIRAS experimental results were in good agreement. Two peaks were resolved for CO$_{linear}$, which could be attributed to the adsorption of CO on Pt(111) and Pt(100). CO$_{linear}$ was best observed with a spectrally overlapping resonance leading to an experimental signal improvement of more than 27 over a conventionally used platinum film. During the electrochemical oxidation of CO, a classic Stark effect was observed. Moreover, thanks to the high resolution provided by the nano-slot metasurface, a redshift of CO$_{linear}$ was observed, linked to a decrease in the coverage of adsorbed CO due to its oxidation. We anticipate our proof-of-concept nanophotonic-electrochemical platform for SEIRAS to guide new system designs and material combinations suitable to characterize different electrochemical interfaces, reaction products, and short-lived intermediates.

5.3 Experimental Section

5.3.1 Numerical Simulations

The simulations were performed in CST Studio Suite 2021 using the finite-element frequency-domain Maxwell solver. CaF_2 was simulated using a refractive index, $ñ$, of 1.4, the surrounding medium as water with $ñ \approx 1.33$ and platinum using the data given by Rakić et al.[129] The inside walls perpendicular to the electric field were covered with a model material to represent CO_{linear} at ~2033 cm^{-1}. The titanium adhesion layer was not simulated as including it did not lead to substantial spectral shifts in the resonance position. An impedance-matched open port with a perfectly matched layer introduced linearly polarized light at an angle of 72° across the CaF_2 layer toward the nano-slots. At 72°, the light was totally internally reflected at the CaF_2-Pt interface. Therefore, the boundary opposite to the open port was set as a perfect electric conductor. The unit cell was defined and then simulated as an infinite periodic array via Floquet boundaries. A field monitor was placed at the center of the slot in the xy-plane. The highest field enhancement was found slightly above the apex of the slots. The value of the highest field enhancement of the system was evaluated within the volume of the numerical model. To extract the Q factor and coupling ratio $\gamma_{ext}/\gamma_{int}$, the simulated resonance was fitted in reflectance (Figure 5.1d, blue curve) using temporal coupled-mode theory according to Hu et al.[16].

5.3.2 Metasurface Fabrication

CaF_2 was chosen as the substrate due to its transparent nature in the mid-IR spectral range, low solubility, and high chemical stability. The measurements shown in Figure 5.4 and Figure 5.5 used metasurface arrays with at least 2200 by 2700 unit cells, resulting in a pattern area of approximately 13.3 mm^2. This ensured that there were more than enough unit cells for the measured resonance to correspond to the mode of the infinite periodic array used for the numerical simulations. After sample cleaning (acetone bath in an ultrasonic cleaner followed by oxygen plasma cleaning) the substrate was spin-coated first with an adhesion promoter (Surpass 4000), then with a layer of negative tone photoresist (ma-N 2403) which was baked at 100 °C for 60s, and finally with a conducting layer (ESpacer 300Z). The metasurface patterns were created by defining the unit cell and reproducing it in the x and y-directions. Then, the patterns were written via electron-beam lithography (Raith Eline Plus) with an acceleration voltage of 30 kV and an aperture of 20 μm. The exposed resist was developed in ma-D 525 for 70 s at room temperature. The patterned surface was then coated with a titanium adhesion layer (1 nm at 0.4 Å.s^{-1}) and a platinum film (30 nm at 2 Å.s^{-1}) using electron-beam evaporation (PRO Line PVD 75, Lesker). Finally, an overnight lift-off in mr-REM 700 concluded the top-down

fabrication process. A pure 30 nm thick platinum film on 1 nm titanium on CaF_2 functioned as a reference for the in-situ SEIRAS measurements.

5.3.3   In-Situ SEIRAS and Electrochemical Measurements

SEIRAS was performed using a Vertex 80 coupled with an IMAC chamber from Bruker. Each sample was mounted on a VeeMax III (purged with N_2) from PIKE Technologies in an ATR geometry with a light polarizer, an electrochemical Jackfish cell, and a CaF_2 prism beveled at 72°. A classical three-electrode system was used with a saturated calomel electrode (E = 0.244 V_{SHE}), a platinum wire as the counter electrode, and the platinum film as the working electrode. The IMAC chamber was equipped with a focal plane array detector composed of 64 x 64 mercury cadmium telluride detectors (a total of 4096 detectors), which resulted in a heat map of the studied sample. Each detector collected its own spectrum. The active slot covered area was detected by integrating the spectra between 1600 to 2800 cm^{-1} (Figure 5.4b, inset). Finally, an average was determined using the spectra of the detectors that probed the resonance. A baseline correction was applied to the average as well as a Savitzky–Golay filter to smoothen the data.

For the characterization of the resonance, its position was determined using three samples composed of arrays with different nanostructure sizes. For each sample, the resonance was measured in K_2CO_3 (0.5M, pH 11.9) electrolyte saturated with Ar and then saturated with CO. Prior to the first characterization, a cyclic voltammogram (20 $mV.s^{-1}$) was recorded in order to confirm the cleanliness of the electrode surface. Then, an initial background was acquired using *p* polarized light and the Fano resonance was characterized using *s* polarized light. Each spectrum was recorded with a resolution of 4 cm^{-1} and the final heat map resulted from a collection of 32 scans. The enhancement of the nano-slot metasurface was obtained by comparing the spectra corresponding to CO_{linear} obtained on the metasurface with those obtained on a pure Pt film (30nm) without nanostructures.

The adsorption of CO during the transition from Ar^{sat} to CO^{sat} electrolyte (0.5M K_2CO_3) was studied using the nano-slot metasurface with the best overlapping resonance with CO_{linear}. Cleaning and background acquisition protocol were the same as described above. Carbon monoxide was slowly flown into the electrochemical cell and spectra were acquired regularly during the transition from Ar^{sat} to CO^{sat} at the OCP.

The oxidation of CO during potential sweeps was investigated after 2 hours of CO bubbling. A cyclic voltammogram, with a slow scan rate (0.25 $mV.s^{-1}$), from the OCP to +1700 mV_{RHE} and back to -100 mV_{RHE} was performed and a spectrum was acquired every 100 mV.

6. Multi-Band Metasurface-Driven Surface-Enhanced IR Absorption Spectroscopy for Improved Characterization of In-Situ Electrochemical Reactions

The results presented in this chapter are currently under peer review for publication and are published as a preprint in the pre-print archive arXiv in Ref.[208]

Duportal, M., Berger, L. M., Maier, S. A., Tittl, A., Krischer, K., Multi-band metasurface-driven surface-enhanced infrared absorption spectroscopy for improved characterization of in-situ electrochemical reactions. arXiv preprint arXiv:2307.10951 2023. https://doi.org/10.48550/arXiv.2307.10951

Note: M.D. and L.M.B. contributed equally to this work.

The study of intermediates occurring during electrochemical reactions remains a challenge due to low surface coverages and short lifetimes. In Chapter 5, we showed that a precisely nanostructured platinum metasurface as a nanophotonic-electrochemical platform based on ATR-SEIRAS can amplify a characteristic signal trace of CO_{linear} during CO oxidation.[55] However, the reported nanophotonic-electrochemical platform only featured one resonance and could therefore only spectrally target and enhance one molecular vibrational mode. Moreover, little attention has been paid to the involvement of bridge-site configurations of CO on Pt during the CO_2RR. The few studies that were conducted focused on acidic media.[209–212] A fundamental and systematic study of bridge-site configurations during the CO_2RR in alkaline media is still missing.
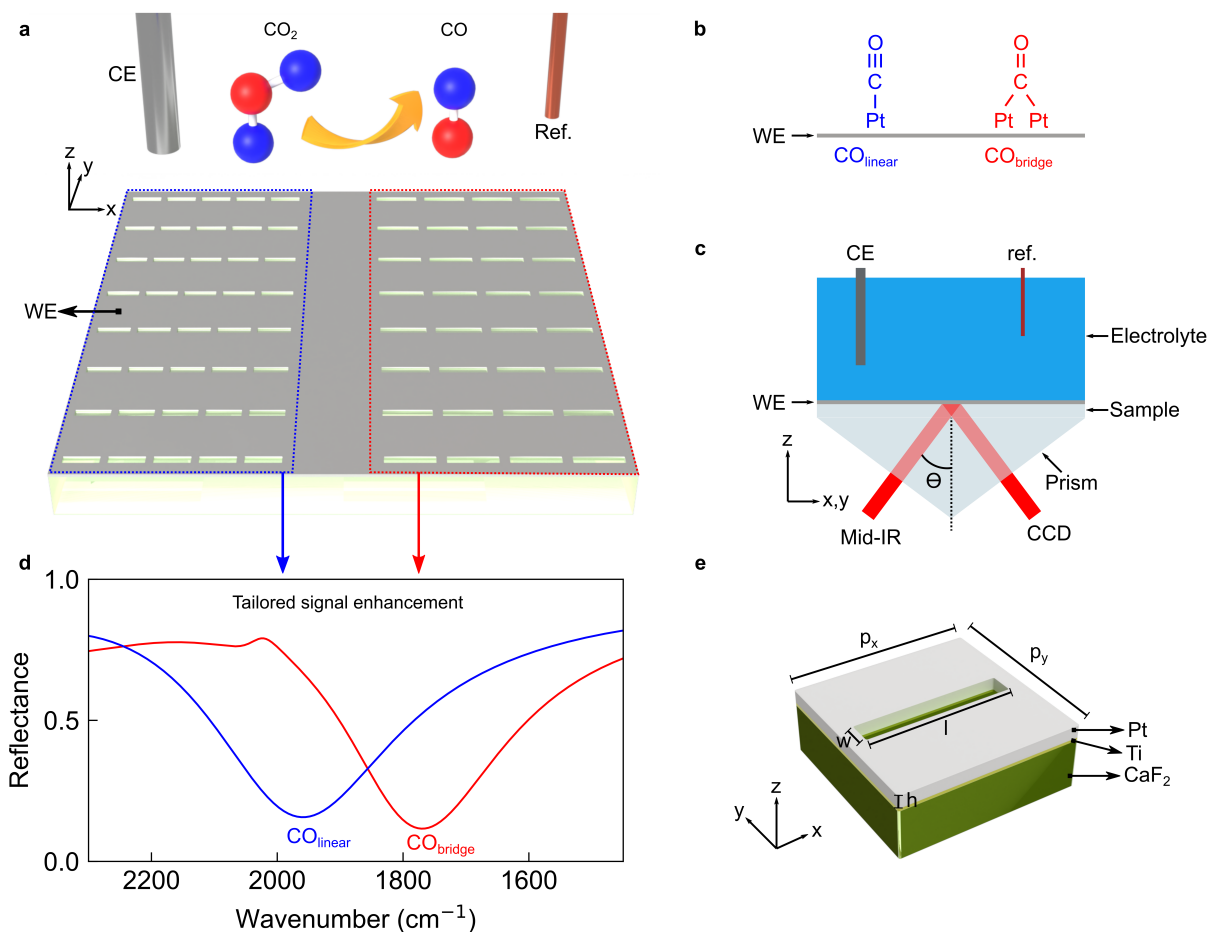
Figure 6.1. Concept and numerical design of the multi-band nanophotonic-electrochemical platform. (a) Schematic of the multi-band platinum-based nano-slot metasurface to study in-situ CO_2 reduction. (b) Schematic showing the chemical structure of the two adsorption configurations of CO on platinum. (c) Schematic illustrating the metasurface in an electrochemical chamber filled with electrolyte that was illuminated from below in an ATR geometry. (d) The resonances stemming from two metasurface arrays on Pt. The shared geometrical parameters were h = 30 nm, w = 180 nm, p_y = 1420 nm, $p_x - l$ = 230 nm with the slot length being swept from (blue) l = 1370 nm to (red) l = 1580. (e) Sketch of the unit cell. A 1 nm thick Ti adhesion layer was utilized in the structure's fabrication for improved adhesion of Pt on CaF_2.

In this chapter, we demonstrate multi-band metasurface-driven ATR-SEIRAS for the improved characterization of in-situ electrochemical reactions (Figure 6.1a). We used a platinum nano-slot metasurface featuring two arrays that spectrally targeted two characteristic molecular vibrations of the CO_2RR: on-top (CO_{linear}) and bridged bound (CO_{bridge}) CO molecules, respectively (Figure 6.1b). For each vibrational mode, a unique array featuring a spectrally targeted resonance locally enhanced the electric near fields and thereby the corresponding molecular signal traces. SEIRAS was performed in an

108

ATR geometry (Figure 6.1c) to maintain free accessibility of the electrode surface and minimize the contribution of the electrolyte to the IR spectrum.

6.1 Numerical Design of the Catalytic Multi-Band Nano-Slot Metasurface.

We start the implementation of our catalytic multi-band nano-slot metasurface by defining the fundamental unit cell for the numerical simulations consisting of a solitary slot within a continuous platinum film immersed in water on CaF_2. The parameters of the unit cell of the nano-slot metasurface are defined in Figure 6.1e, where p_x and p_y are the unit cell lengths in x and y. The geometrical parameters of the unit cell can be changed to tune the resonance strength and position of the metasurface. As the goal of our investigations was a multi-band signal enhancement, the unit cell parameters were separately tuned to two resonance frequencies matching the vibration frequencies of two different adsorption configurations of CO on platinum. Specifically, the goal was a straightforward approach to create two adjacent nanostructured arrays on platinum that would each enhance one of the two vibrational frequencies.

A common approach to achieving this is to scale all geometrical dimensions of the system at the same time, used for example in biosensing[7] and catalysis[16]. However, constraints in the fabrication with negative resists limited the unit cell length in y to a minimum of 1.4 µm due to proximity effects. Proximity effects arise due to the scattering of electrons in the resist and substrate due to exposure to an electron beam.[213] We found that the slots merged and the quality of the lift-off procedure decreased as the unit cell length in y was decreased below 1.4 µm. Therefore, we simplified the resonance tuning protocol, allowing only the slot length to change and taking into account a shift of approximately 80 cm^{-1} between simulation and experiment. By increasing the slot length from 1370 nm to 1580 nm while leaving all other parameters unchanged the metasurface-driven resonance was redshifted by ~150 cm^{-1} (Figure 6.1d), corresponding to the spectral separation of the vibrational modes.

The Rayleigh anomaly was tuned to the higher frequency side of the resonance to ensure optimal sensing performance. To improve the characterization of the resonances, the fitting model was adapted specifically for total internal reflection (see Experimental section). The Q factor and coupling ratio $\gamma_{ext}/\gamma_{int}$ were obtained by fitting the simulated resonance in reflection using temporal coupled-mode theory (see Experimental Section). Based on our simulations, the multi-band nano-slot metasurface achieved a modulation of approximately 84% and 88% in reflection, a Q factor of 4.3 and 5.0, and a ratio of external to intrinsic coupling of 2.6 and 2.1 for the higher and lower frequency resonances, respectively. Our system can be further optimized by maximizing the modulation in reflection or absorption to push it toward its critical coupling condition.
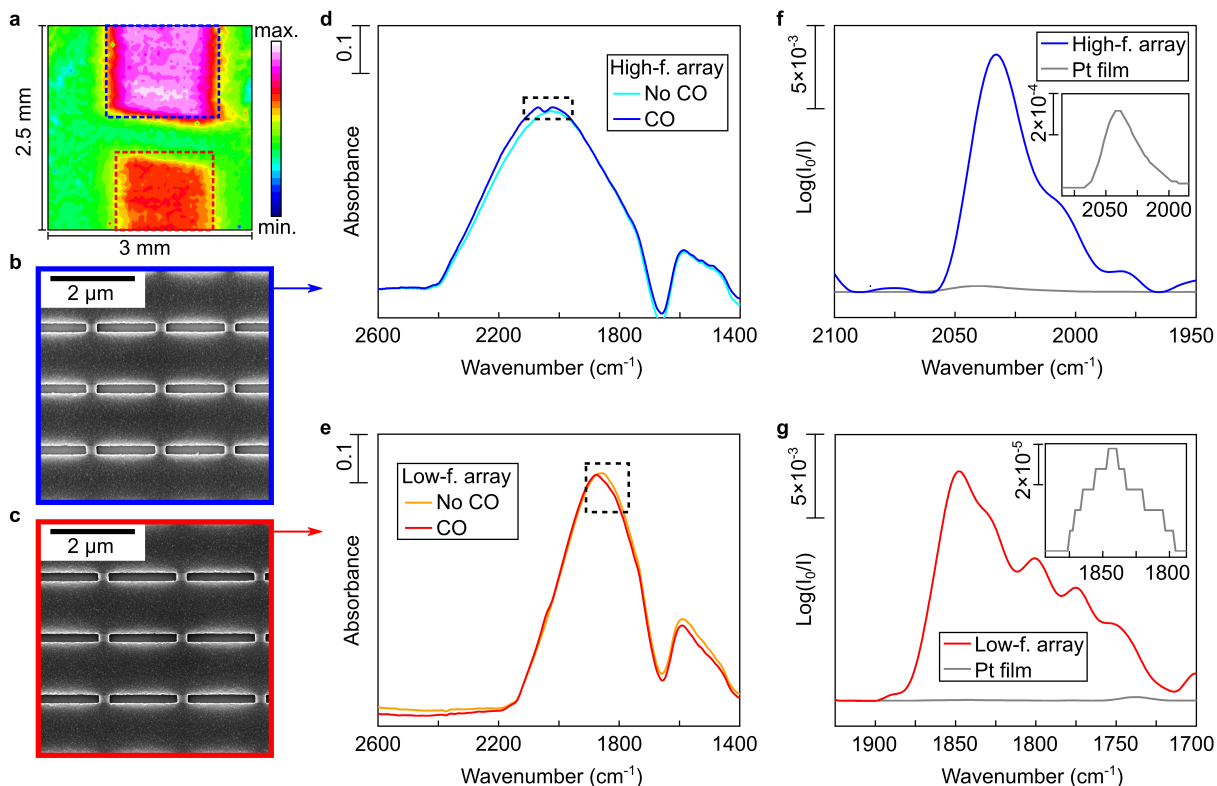
Figure 6.2. Characterization of the multi-band nano-slot metasurface. (a) Heat map of the metasurface obtained by integrating the SEIRAS signal from 1600 to 2800 cm^{-1}. (b-c) SEM pictures of the (b) high and (c) low-frequency arrays, indicated in (a) via blue and red-dashed boxes, respectively. (d-e) Resonances with and without CO for the (d) high and (e) low-frequency arrays in 0.5M K_2CO_3. (f-g) Comparison of the differential absorbance obtained with the (f) high and (g) low-frequency array with an unstructured Pt film (30 nm thick, inset) and with the multi-band nano-slot metasurface.

6.2   Multi-band Metasurface Characterization.

According to the literature, the vibrational modes of CO_{linear} and CO_{bridge} were expected to occur at ~2050 cm^{-1} [156–160] and ~1850 cm^{-1} [156,157,159,214], respectively. First, we characterized the optical properties of our multi-band metasurface in electrolyte saturated with Ar and CO using SEIRAS. An example of the heat map obtained by integrating the IR spectra collected by the focal plane array detector is provided in Figure 6.2a. The two pink-colored areas correspond to the two metasurface-arrays designed to enhance CO detection. The quality of the fabricated slots was verified by scanning electron microscopy images (Figure 6.2b-c). The signal received by the high-frequency array (Figure 6.2a, bottom array) was averaged, resulting in a resonance that was spectrally positioned at ~2030 cm^{-1} in Ar-saturated electrolyte (Figure 6.2d). On the other hand, the average

signal from the low-frequency array (Figure 6.2a, right array) produced a resonance located at ~1860 cm^{-1} (Figure 6.2e). In both cases, the system presented a near critically-coupled behavior between the metasurface-driven resonances and the vibrational modes of CO,[55] leading to a dip in the high and low-frequency resonances at 2046 cm^{-1} and 1848 cm^{-1}, respectively.

To extract the signal of CO_{linear} and CO_{bridge} more clearly, then, the reflectance spectra with, R, and without, R_0, adsorbed CO were converted into their differential absorbance, $-\ln\frac{R}{R_0}$, to separate the metasurface-driven resonance from the CO signals (Figure 6.2f-g). Furthermore, a comparison of the differential absorbance in the regions of CO_{linear} and CO_{bridge}, obtained on an unstructured Pt film (30 nm thick) and with our multi-band nano-slot metasurface, indicated that the high-frequency array exhibited a signal enhancement of 41. This signal enhancement is higher than the enhancement reported in our previous work,[55] attributed to an improved lift-off procedure. The signal enhancement provided by the low-frequency array cannot be reliably estimated, as the CO_{bridge} signal was not clearly distinguishable on the unstructured Pt film. The CO_{bridge} signal could only be observed here with the multi-band metasurface due to its high signal-enhancing properties.

6.3 Behavior in CO saturated electrolyte.

As a proof of concept, the behavior of the multi-band nano-slot metasurface in 0.5M K_2CO_3 saturated with CO was provided here by using electrochemical voltammetry. A cathodic scan was conducted with a rate of 0.25 mV.s^{-1} starting at 1650 mV$_{RHE}$, as shown in Figure 6.3a. As already observed in the literature,[55,195,196] the increase in the current around 950 mV$_{RHE}$ followed by a plateau corresponds to the oxidation of CO into CO_2, which was limited by CO diffusion from the bulk of the electrolyte to the Pt surface. Then, the following decrease in current at 350 mV$_{RHE}$ indicates the end of the region where CO was oxidized. Finally, the slight drop in current around 0 mV$_{RHE}$ was attributed to the hydrogen evolution reaction. SEIRAS spectra were acquired at intervals of 100 mV during a cathodic scan. The potential regions in which CO was or was not detected are shown as red and blue regions, respectively.

The evolution of the IR spectrum with the electrical polarization of the high (Figure 6.3b) and low-frequency (Figure 6.3c) arrays shows the successful detection of CO_{linear} and CO_{bridge}, respectively. The vibrational modes appeared as peaks in the differential absorbance spectra. Regarding the behavior of CO_{linear}, a spectral shift of approximately 63 cm^{-1}.V^{-1} was observed (Figure 6.3d) from 450 mV$_{RHE}$ to -50 mV$_{RHE}$, which is in line with the literature[55,177,179,200,215] and can be attributed to either a higher π-back-donation from the metal to CO[179,199] and/or to the Stark shift.[199–201] Additionally, a significant spectral redshift attributed to the decrease of the dipole-dipole interactions as the

111

coverage decreased[204,216] was resolved from 650 to 450 mV$_{RHE}$ (Figure 6.3d), thanks to the high resolution achieved with our platform.

Concerning the behavior of CO$_{bridge}$ on the low-frequency array, a distinct peak was resolved exhibiting a similar behavior as CO$_{linear}$. However, the observed Stark shift in this case was smaller, resulting in approximately 21 cm^{-1}.V^{-1}. This difference in Stark shift between CO$_{linear}$ and CO$_{bridge}$ was observed in the literature.[200,215] However, the origin of this difference is still controversial as other authors suggested that both configurations should provide the same Stark shift.[217,218] Our observations can be explained by the smaller IR cross-section of CO$_{bridge}$ compared to CO$_{linear}$.[217] When CO is adsorbed linearly on the platinum surface, it strongly binds to the Pt atoms,[219] which could explain the larger Stark shift. Furthermore, the electric field from the metal surface could have affected CO$_{linear}$ more significantly, leading to a larger change in its vibrational frequency. On the other hand, the configuration of CO$_{bridge}$ may have resulted in a weaker interaction with the metal surface.[219] In that case, the electric field from the metal surface could have had a smaller impact on this configuration, resulting in a smaller Stark shift.

At higher potentials, a redshift with decreasing coverage was observed next to a broadening of the peak from 550-750 mV$_{RHE}$, which needs further investigation. A Fano-type asymmetric peak was observed at the same position as CO$_{linear}$ due to the off-resonance coupling between the resonance of the low-frequency array and the vibrational mode of CO$_{linear}$.[220] Interestingly, the area of the CO$_{linear}$ peak slightly decreased from 650 mV$_{RHE}$ to -50 mV$_{RHE}$, while the area of the CO$_{bridge}$ peak showed a continuous increase (Figure 6.3e). The area and intensity of the CO peaks were related to the coverage of CO$_{linear}$ and CO$_{bridge}$, suggesting a transfer from CO$_{linear}$ to CO$_{bridge}$ as the cathodic potential increased. According to some authors,[215,219] the competition between CO and hydrogen adsorption on Pt in the cathodic region could have been responsible for this transition. Furthermore, the barrier for CO diffusion from a top site to a bridge site was theoretically predicted to be very small.[221] These findings can explain the increase in the area of the peak attributed to CO$_{bridge}$ to the detriment of the CO$_{linear}$ peak area, which decreased.

To conclude, our multi-band nano-slot metasurface selectively and simultaneously enhanced and detected with high accuracy the behavior of CO$_{linear}$ and CO$_{bridge}$. In the next section, the study focuses on the behavior of adsorbed CO during the CO$_2$ reduction reaction.
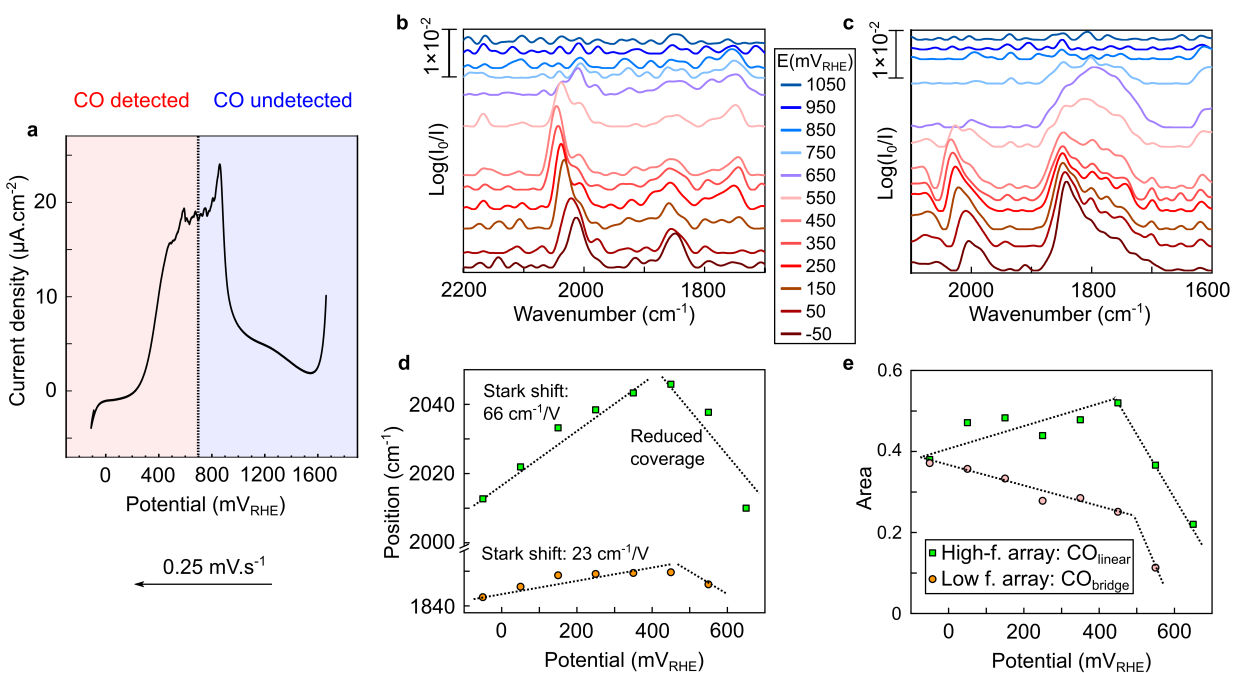
Figure 6.3. Cathodic polarization of the multi-band metasurface in 0.5M K_2CO_3 saturated with CO. (a) Evolution of the current density during the cathodic polarization at 0.25 mV.s^{-1}. (b-c) Evolution of the IR spectra with the potential acquired by the arrays optimized for (b) CO_{linear} and (c) CO_{bridge} detection. (d-e) Evolution of the (d) position and (e) area of peaks with the potential.

6.4   Reduction of CO_2.

The cathodic scan of the cyclic voltammetry of the multi-band metasurface in 0.5M K_2CO_3 saturated with CO_2 showed a dip around 400 mV_{RHE} (Figure 6.4a), which could be attributed to the chemisorption of hydrogen.[222–224] A second peak appeared around 250 mV_{RHE}, which was attributed to CO_2 reduction.[160] The drop in the current starting at 0 mV_{RHE} was due to the hydrogen evolution reaction. The positive current peak observed after reversing the scan direction stemmed from the hydrogen oxidation reaction.[200] Finally, a small oxidative peak was observed around 550 mV_{RHE} and was attributed to the oxidation of the previously formed CO.[197] Looking at the IR spectra of the high-frequency array optimized for CO_{linear} during the cathodic scan (Figure 6.4b), a peak was observed around 200 mV_{RHE}. This peak indicated the presence of adsorbed CO, which is directly correlated to the reduction peak observed in the voltammogram. Moreover, this peak became more pronounced and more defined with higher cathodic polarizations.
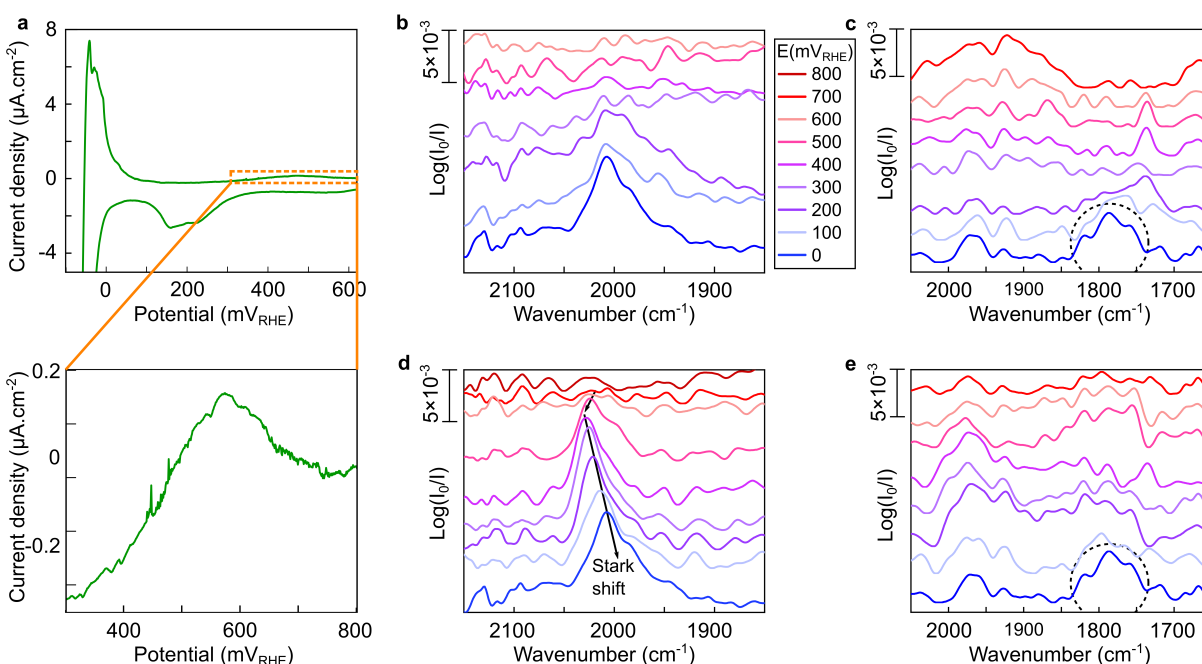
Figure 6.4. Cyclic voltammetry of the multi-band metasurface in 0.5M K_2CO_3 saturated with CO_2. (a) Evolution of the current density during the polarization at 0.25 mV.s^{-1}. A zoom-out of the current density is shown. (b-c) Evolution of IR spectra with the potential acquired on the (b) high-frequency array optimized for CO_{linear} and (c) low-frequency array optimized for CO_{bridge} detection during the cathodic scan. (d-e) Evolution of IR spectra with the potential acquired on the (d) high-frequency array optimized for CO_{linear} and (e) the low-frequency array optimized for CO_{bridge} detection during the anodic scan.

Moving to the low-frequency array optimized for CO_{bridge} detection, at the highest applied cathodic polarization (0 mV$_{RHE}$) a small peak became discernible at around 1785 cm^{-1} in the IR spectra (Figure 6.4c). This peak was hardly above the detection limit despite the high resolution achieved with our multi-band nanophotonic-electrochemical platform. It appeared at significantly higher cathodic potentials (200 mV difference) than the CO_{linear} peak obtained with the high-frequency array. Our findings suggest that CO_{bridge} was not significantly involved in the CO_2 reduction process on Pt. Some authors[157,225] have suggested that the favorable configuration of adsorption of CO on Pt is CO_{linear}. Moreover, the literature suggests that CO_{bridge} formation occurred once the CO coverage approached its maximum limit, where a transfer from CO_{linear} to CO_{bridge} takes place.[215,219]

During the anodic scan, the CO_{linear} peak maintained a constant amplitude (Figure 6.4d) but exhibited a classic Stark shift between 0 to 400 mV$_{RHE}$, followed by an intensity decrease and a small redshift attributed to a reduced coverage around 500 mV$_{RHE}$. Then, the peak disappeared, which can be directly correlated with the oxidation peak observed in the voltammogram (Figure 6.4a). In contrast, the peak attributed to CO_{bridge}

disappeared at 100 mV$_{RHE}$ (Figure 6.4e), supporting our conclusion that CO$_{bridge}$ was not significantly involved in the CO$_2$ reduction on platinum in an alkaline environment. The distortion of the baseline at around 2000 cm^{-1} was attributed to the strong off-resonance coupling between the metasurface-driven resonance of the low-frequency array and the vibrational mode of CO$_{linear}$.[220] Thanks to the high resolution and signal enhancing properties provided by our nanophotonic-electrochemical platform, Figure 6.4 suggests that CO$_{bridge}$ was not significantly involved in the reduction of CO$_2$ in alkaline electrolyte. This is noteworthy because CO$_{bridge}$ was detected in acidic electrolyte during the CO$_2$RR.[209–212] The difference in the CO adsorption behavior between alkaline and acidic media could be due to a modification of the competition with the hydrogen evolution reaction. In fact, in an alkaline environment, the Heyrovsky reaction is often considered the dominant pathway, which differs from the Volmer-Tafel mechanism observed in acidic media.[226–228] The Heyrovsky reaction involves the formation of hydroxide ions near the Pt surface, which could interact with adsorbed CO$_2$ and CO to favor the formation of CO$_{linear}$. These considerations are in agreement with our observation that CO$_{bridge}$ did not significantly participate in the CO$_2$RR in K$_2$CO$_3$, i.e., in an alkaline environment.

6.5 Conclusion

We have developed a multi-band nanophotonic-electrochemical platform enabling enhanced simultaneous in-situ characterization of two adsorption configurations of CO on Pt during the electrochemical reduction of CO$_2$. Our platform provided an enhancement over conventional systems by a factor of over 40. Crucially, our platform was able to detect CO$_{bridge}$, which could not be detected here with an unstructured Pt film. Using a straightforward and easily reproducible methodology, we numerical modeled, fabricated, and tested our platform. CO$_{linear}$ and CO$_{bridge}$ were characterized in CO-saturated electrolyte, highlighting a transition from top to bridge-site configurations at high cathodic potentials and demonstrating the high resolution provided by our platform. The vibrational modes of CO were confirmed via their typical Stark shift. Our final experimental tests focused on the characterization of the CO$_2$RR. Interestingly, we found that during the CO$_2$RR in an alkaline environment, CO$_{bridge}$ does not play a significant role, whereas CO$_{linear}$ was successfully detected. This finding could be attributed to the competition with the hydrogen evolution reaction in alkaline environments. We anticipate that our multi-band nanophotonic-electrochemical platform provides a new strategy to study electrochemical reactions with low coverage or transient features by providing a higher resolution than conventional systems for multiple IR-active vibrational modes.

6.6 Experimental Section

6.6.1 Numerical Simulations.

The numerical simulations in this study utilized CST Studio Suite (2021), which uses the finite-element frequency-domain Maxwell solver. For the simulation of CaF_2, a refractive index of 1.4 was used, while the surrounding medium was represented by water with a refractive index of 1.33. Platinum was modeled using its experimental complex refractive index data.[129] To introduce linearly polarized light at an angle of incidence of 72° into the system, an impedance-matched open port with a perfectly matched layer was employed. Since light experienced total internal reflection at this angle at the CaF_2-Pt interface, the boundary opposite to the open port was set as a perfect electric conductor. The unit cell was defined and simulated as an infinite periodic array using Floquet boundaries.

6.6.2 Analytical analysis of resonances.

The resonances were characterized in terms of their radiative γ_{rad} and intrinsic γ_{int} damping rates, from which their total Q factor could be determined as $Q_{tot} = \frac{v_0}{2(\gamma_{rad}+\gamma_{int})}$, where v_0 is the central wavenumber. We employed temporal coupled-mode theory[229] according to Ref.[230] describing a resonator with a single port that supports reflected waves and a single resonance coupling to the far field via the coupling constant $\kappa = \sqrt{2\gamma_{rad}}$. Additionally, an intrinsic loss channel introduced damping to the resonance at a rate γ_{int}. The reflectance spectra R were fitted by

$$R = 1 - \frac{4\gamma_{rad}\gamma_{int}}{(v - v_0)^2 + (\gamma_{rad} + \gamma_{int})^2},$$

where v is the wavenumber.

6.6.3 Multi-band Metasurface Fabrication.

The multi-band metasurface fabrication was similar to the protocol provided in Ref.[55] Instead of one array, two arrays were fabricated ~500 μm apart to fit within the window of the focal plane array of the FTIR spectrometer. The arrays were each approximately 3×2 mm in size, which had to be large as the FTIR spectrometer did not have and did not need a focusing microscope objective. We chose CaF_2 as the substrate due to its transparent properties within the mid-IR spectral range, as well as its high chemical stability and low solubility. Before the experiments, the substrate underwent a thorough

cleaning process, involving an acetone bath in an ultrasonic bath, followed by oxygen plasma treatment. Subsequently, the substrate was spin-coated with an adhesion promoter (Surpass 4000), followed by a layer of negative-tone photoresist (ma-N 2403). The photoresist was baked at 100 °C for 60 s, and a conducting layer (ESpacer 300Z) was deposited using spin-coating. The metasurface patterns were generated by defining a unit cell and replicating it in both the *x* and *y*-directions. Electron-beam lithography (Raith Eline Plus) was employed to write the patterns, utilizing an acceleration voltage of 30 kV and an aperture of 20 µm. The exposed resist was developed in ma-D 525 for 70 s at room temperature. Thereafter, a titanium adhesion layer (1 nm at 0.4 Å s^{-1}) and a platinum film (30 nm at 2 Å s^{-1}) were deposited on the patterned surface using electron-beam evaporation (PRO Line PVD 75, Lesker). Finally, the fabrication process was completed by an overnight lift-off in mr-REM 700. For the in-situ SEIRAS measurements, a pure 30 nm thick platinum film on a 1 nm titanium layer on CaF$_2$ was utilized as a reference.

6.6.4 Surface-Enhanced Infrared Absorption Spectroscopy Measurements.

SEIRAS was conducted using a Vertex 80 spectrometer equipped with an IMAC Focal Plane Array macro imaging accessory from Bruker. A specular reflection unit (VeeMax III from PIKE Technologies) paired with a CaF$_2$ prism and light polarizer introduced light at 72° w.r.t. an electrochemical jackfish cell, thereby enabling the attenuated total internal reflection geometry. A focal plane array detector (64 × 64 mercury-cadmium-telluride detectors) was used to characterize the optical properties of the multi-band nano-slot metasurface. By integrating the measured (absorbance) signal across the spectral range corresponding to the metasurface-driven resonances (1600-2800 cm^{-1}), a pixelated two-dimensional heat map of the sample was created to identify the pixels corresponding to the nanostructured arrays (Figure 6.2a). Then, the pixels corresponding to each array were averaged to construct the final spectra. The samples were cleaned via electrochemical cycling. Prior to each measurement, an initial background was acquired using *p* polarized light. The metasurface-driven resonances were measured in situ using *s* polarized light. Each spectrum was acquired at a resolution of 4 cm^{-1} and by averaging 10 scans. The data was treated by applying a baseline correction and Savitzky-Golay filter. The enhancement provided by the multiband metasurface was determined by comparing the area of the peaks associated with the vibrational modes of CO$_{linear}$ and CO$_{bridge}$ to the corresponding measurement performed on an unstructured Pt film (30 nm).

6.6.5 Electrochemical Measurements.

A classical three-electrode system was implemented by using the Pt multi-band metasurface as the working electrode, a Pt wire as the counter electrode, and a saturated

calomel electrode (E = 0.244 V_{SHE}) as the reference electrode. The electrolyte was a 0.5 mol.L^{-1} K_2CO_3 solution (pH 11.9), saturated with either Ar, CO, or CO_2. Before the first characterization, the cleanliness of the electrode surface was verified by performing a cyclic voltammogram at a scan rate of 20 mV s^{-1} in Ar-saturated electrolyte.

The behavior of the nano-slots was characterized in CO-saturated electrolyte. After bubbling CO for 2 hours, cyclic voltammetry was performed from +1650 mV_{RHE} to -85 mV_{RHE}, using a scan rate of 0.25 mV.s^{-1}.

Finally, we saturated the electrolyte with CO_2, which decreased the pH to approximately 8. After 2h of gas bubbling, cyclic voltammograms were measured with a slow scan rate of 0.25 mV s^{-1}, from the OCP to + 1425 mV_{RHE} and then back to +25 mV_{RHE}. SEIRAS spectra were acquired in intervals of 100 mV.

7.   Conclusion and Outlook

In this work, novel metasurface concepts and functionalities were investigated. We demonstrated the versatility of metasurfaces in two key areas, at the interface to electrochemistry and towards angular-robust sensing.

We explored novel concepts of BIC-driven metasurfaces, finding that displacement-mediated BIC-driven metasurfaces provided angular-robust operation, an important feature required for broadband sensing. In particular, we investigated positive and inverse, metal and all-dielectric superlattices and found that they produce displacement-mediated q-BIC resonances that can be described by a displacement asymmetry parameter α. Numerical models revealed that an inverse all-dielectric superlattice can produce a displacement-mediated q-BIC resonance under the same polarization as its positive counterpart. Furthermore, the numerical analysis revealed that Babinet's principle applies to the displacement-mediated q-BIC for metal superlattices. Numerical investigations of the angular dependence of the q-BIC resonance position successfully led to conclusions on the angular stability of the superlattice variations. The experimental realization of the superlattices confirmed that under near-normal incidence, a displacement-mediated q-BIC resonance emerged for $\alpha \neq 0$. The silicon positive, gold positive, and inverse superlattice metasurfaces were fabricated and tested under a reflective microscope objective and compared to two conventional platforms used for sensing: silicon-based tilted ellipses and gold nanohole metasurfaces. The performance of the metasurfaces was quantified by their relative change in their resonance parameters when the range of angles was increased by a switch in microscope objectives. This switch corresponds to an increase in the range of angles and a test of their angular robustness.

The strong performance of the fabricated superlattice metasurfaces compared to rivaling platforms was attributed to better angular robustness predicted by numerical angular dispersion plots. Despite the strong resonances of the silicon-tilted ellipses and gold nanohole metasurfaces at near-normal incidence, their resonance parameters deteriorated by 62% and 100%, respectively. The best performance was achieved with the positive gold superlattice, which performed 118%, 46%, and 59% better than the tilted ellipses, silicon superlattice, and gold inverse superlattice, respectively. Furthermore, it showed the advantageous characteristic of having a highly symmetric resonance lineshape. The numerical models showed a maximum local electric near-field enhancement of 378 for $\alpha = 0.3$. This value can be further increased by decreasing α.

Furthermore, we showed that metasurfaces can simultaneously function as a working electrode and optical sensor. First, we developed the first hybrid nanophotonic-electrochemical platform for SEIRAS based on a platinum nano-slot metasurface, targeting, at first, the detection of only one vibrational mode at 2033 cm^{-1} corresponding to adsorbed CO in top sites on Pt. The metasurface-driven resonance was numerically modeled, yielding a maximum electric near-field intensity enhancement of 560. The

resonance was tuned to couple with and enhance the CO vibrational mode at 2033 cm^{-1}. To validate the principle behind the sensing improvement, we fabricated both on-resonance and detuned metasurfaces and carefully analyzing the resonance. The numerical simulations and SEIRAS experimental results were in good agreement. Two peaks were resolved for CO_{linear}, attributable to adsorption of CO on Pt(111) and Pt(100). CO_{linear} was best observed with a spectrally overlapping resonance, leading to an experimental signal improvement of more than 27 compared to conventional platinum films. Additionally, during the electrochemical oxidation of CO, a classic Stark shift was observed. Leveraging the high resolution provided by the nano-slot metasurface, a redshift in CO_{linear} was observed and linked to a reduced coverage of adsorbed CO due to its oxidation.

Finally, we customized the single-band nanophotonic-electrochemical platform to simultaneously characterize multiple vibrational bands and studied the more significant electrochemical reduction of CO_2. Remarkably, this platform outperformed conventional systems by an impressive factor of over 40. Notably, it enabled the detection of the CO_{bridge} configuration, which remained undetected here with an unstructured Pt film. Using a straightforward and easily reproducible methodology, we numerical modeled, fabricated, and tested our platform. The CO_{linear} and CO_{bridge} configurations were characterized in CO-saturated electrolyte, revealing a transition from top to bridge-site configurations at high cathodic potentials and showcased the superior resolution of our platform. Moreover, the vibrational modes of CO were confirmed via their characteristic Stark shift. Finally, during the characterization of the CO_2RR in an alkaline environment, we found that the CO_{bridge} configuration did not play a significant role, whereas the CO_{linear} was successfully detected.

We anticipate that the promising results shown in this work will encourage future generations of researchers to continue exploring the interface between nanophotonics and emerging scientific domains and applications. In particular, we anticipate that our efforts towards angular-robust sensing will be useful for the wider research community working with hyper-spectral imaging, FTIR spectroscopy, and laser materials processing. Our results on the angular robustness of the superlattice predict that our metasurfaces can be adopted by researchers working on conformal optical devices, displays, and photonic devices using focused light. In particular, we anticipate that the positive gold superlattice will be used in biospectroscopy and sensing due to the externalized and high electric near-field enhancement and symmetric resonance profile. Moreover, we anticipate that both our single and multi-band nanophotonic-electrochemical platforms for SEIRAS will guide new system designs and material combinations to characterize new electrochemical reactions with low coverages, weak signals, and transient features, by providing a higher resolution than conventional systems.

Appendix

A. Publisher Permission ACS Publications: Nano Letters

B. Publisher Permission ACS Publications: ACS Photonics

Plasmonic Enhancement of Infrared Vibrational Signals: Nanoslits versus Nanorods

ACS Publications
Most Trusted. Most Cited. Most Read.

Author: Christian Huck, Jochen Vogt, Michael Sendner, et al

Publication: ACS Photonics

Publisher: American Chemical Society

Date: Oct 1, 2015

Copyright © 2015, American Chemical Society

PERMISSION/LICENSE IS GRANTED FOR YOUR ORDER AT NO CHARGE

This type of permission/license, instead of the standard Terms and Conditions, is sent to you because no fee is being charged for your order. Please note the following:

- Permission is granted for your request in both print and electronic formats, and translations.
- If figures and/or tables were requested, they may be adapted or used in part.
- Please print this page for your records and send a copy of it to your publisher/graduate school.
- Appropriate credit for the requested material should be given as follows: "Reprinted (adapted) with permission from {COMPLETE REFERENCE CITATION}. Copyright {YEAR} American Chemical Society." Insert appropriate information in place of the capitalized words.
- One-time permission is granted only for the use specified in your RightsLink request. No additional uses are granted (such as derivative works or other editions). For any uses, please submit a new request.

If credit is given to another source for the material you requested from RightsLink, permission must be obtained from that source.

BACK   CLOSE WINDOW

C. Publisher Permission ACS Publications: *J. Phys. Chem. C*

An In Situ Surface-Enhanced Infrared Absorption Spectroscopy Study of Electrochemical CO2 Reduction: Selectivity Dependence on Surface C-Bound and O-Bound Reaction Intermediates

Author: Yu Katayama, Francesco Nattino, Livia Giordano, et al

Publication: The Journal of Physical Chemistry C

Publisher: American Chemical Society

Date: Mar 1, 2019

Copyright © 2019, American Chemical Society

BACK

CLOSE WINDOW

D. Publisher Permission American Physical Society

APS American Physical Society
Reuse and Permissions License

17-Aug-2023

This license agreement between the American Physical Society ("APS") and Luca Maria Berger ("You") consists of your license details and the terms and conditions provided by the American Physical Society and SciPris.

Licensed Content Information

License Number:	RNP/23/AUG/069433
License date:	17-Aug-2023
DOI:	10.1103/PhysRevLett.121.193903
Title:	Asymmetric Metasurfaces with High-Q Resonances Governed by Bound States in the Continuum
Author:	Kirill Koshelev et al.
Publication:	Physical Review Letters
Publisher:	American Physical Society
Cost:	USD $ 0.00

Request Details

Does your reuse require significant modifications: No

Specify intended distribution locations:	Worldwide
Reuse Category:	Reuse in a thesis/dissertation
Requestor Type:	Academic Institution
Items for Reuse:	Figures/Tables
Number of Figure/Tables:	1
Figure/Tables Details:	Figure 4
Format for Reuse:	Print and Electronic
Total number of print copies:	More Than 10000

Information about New Publication:

University/Publisher:	LMU Munich
Title of dissertation/thesis:	Multifunctional Metasurfaces for Angular-Robust Operation and Electrochemistry
Author(s):	Luca Maria Berger
Expected completion date:	Oct. 2023

License Requestor Information

Name:	Luca Maria Berger
Affiliation:	Individual
Email Id:	luca.m.berger@gmail.com
Country:	Germany

American Physical Society
Reuse and Permissions License
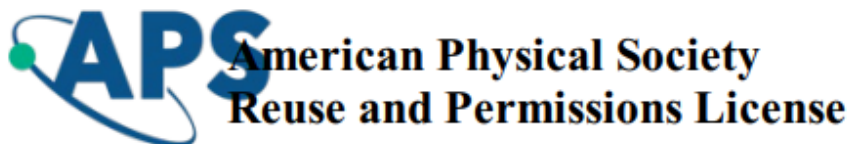
TERMS AND CONDITIONS

The American Physical Society (APS) is pleased to grant the Requestor of this license a non-exclusive, non-transferable permission, limited to Print and Electronic format, provided all criteria outlined below are followed.

1. You must also obtain permission from at least one of the lead authors for each separate work, if you haven't done so already. The author's name and affiliation can be found on the first page of the published Article.

2. For electronic format permissions, Requestor agrees to provide a hyperlink from the reprinted APS material using the source material's DOI on the web page where the work appears. The hyperlink should use the standard DOI resolution URL, http://dx.doi.org/{DOI}. The hyperlink may be embedded in the copyright credit line.

3. For print format permissions, Requestor agrees to print the required copyright credit line on the first page where the material appears: "Reprinted (abstract/excerpt/figure) with permission from [(FULL REFERENCE CITATION) as follows: Author's Names, APS Journal Title, Volume Number, Page Number and Year of Publication.] Copyright (YEAR) by the American Physical Society."

4. Permission granted in this license is for a one-time use and does not include permission for any future editions, updates, databases, formats or other matters. Permission must be sought for any additional use.

5. Use of the material does not and must not imply any endorsement by APS.

6. APS does not imply, purport or intend to grant permission to reuse materials to which it does not hold copyright. It is the requestor's sole responsibility to ensure the licensed material is original to APS and does not contain the copyright of another entity, and that the copyright notice of the figure, photograph, cover or table does not indicate it was reprinted by APS with permission from another source.

7. The permission granted herein is personal to the Requestor for the use specified and is not transferable or assignable without express written permission of APS. This license may not be amended except in writing by APS.

8. You may not alter, edit or modify the material in any manner.

9. You may translate the materials only when translation rights have been granted.

10. APS is not responsible for any errors or omissions due to translation.

11. You may not use the material for promotional, sales, advertising or marketing purposes.

12. The foregoing license shall not take effect unless and until APS or its agent, Aptara, receives payment in full in accordance with Aptara Billing and Payment Terms and Conditions, which are incorporated herein by reference.

13. Should the terms of this license be violated at any time, APS or Aptara may revoke the license with no refund to you and seek relief to the fullest extent of the laws of the USA. Official written notice will be made using the contact information provided with the permission request. Failure to receive such notice will not nullify revocation of the permission.

14. APS reserves all rights not specifically granted herein.

15. This document, including the Aptara Billing and Payment Terms and Conditions, shall be the entire agreement between the parties relating to the subject matter hereof.

E. Publisher Permission Springer Nature

SPRINGER NATURE

Bound states in the continuum
Author: Chia Wei Hsu et al
Publication: Nature Reviews Materials
Publisher: Springer Nature
Date: Jul 19, 2016

Copyright © 2016, Macmillan Publishers Limited

Order Completed

Thank you for your order.

This Agreement between Ludwig-Maximilians-Universität München -- Luca Maria Berger ("You") and Springer Nature ("Springer Nature") consists of your license details and the terms and conditions provided by Springer Nature and Copyright Clearance Center.

Your confirmation email will contain your order number for future reference.

License Number	5630170042141		Printable Details
License date	Sep 15, 2023		

Licensed Content

Licensed Content Publisher	Springer Nature
Licensed Content Publication	Nature Reviews Materials
Licensed Content Title	Bound states in the continuum
Licensed Content Author	Chia Wei Hsu et al
Licensed Content Date	Jul 19, 2016

Order Details

Type of Use	Thesis/Dissertation
Requestor type	academic/university or research institute
Format	print and electronic
Portion	figures/tables/illustrations
Number of figures/tables/illustrations	1
Would you like a high resolution image with your order?	no
Will you be translating?	no
Circulation/distribution	50000 or greater
Author of this Springer Nature content	no

About Your Work

Title	Multifunctional Metasurfaces for Angular-Robust Operation and Electrochemistry
Institution name	Ludwig Maximilian University Munich
Expected presentation date	Oct 2023

Additional Data

Portions	Figure 1

Requestor Location

Requestor Location	Ludwig-Maximilians-Universität München Westermühlstr. 33 München, 80469 Germany Attn: Ludwig-Maximilians-Universität München

Tax Details

Price

Total	0.00 EUR

Total: 0.00 EUR

CLOSE WINDOW | ORDER MORE

F. Publisher Permissions Royal Society of Chemistry

Role of oxygen-bound reaction intermediates in selective electrochemical CO_2 reduction

To request permission to reproduce material from this article, please go to the Copyright Clearance Center request page.

If you are **an author contributing to an RSC publication, you do not need to request permission** provided correct acknowledgement is given.

If you are **the author of this article, you do not need to request permission to reproduce figures and diagrams** provided correct acknowledgement is given. If you want to reproduce the whole article in a third-party publication (excluding your thesis/dissertation for which permission is not required) please go to the Copyright Clearance Center request page.

Read more about how to correctly acknowledge RSC content.

Bibliography

[1] Lord Rayleigh, *The London, Edinburgh, and Dublin Philosophical Magazine and Journal of Science* **1899**, *47*, 375.

[2] G. Mie, *Annalen der Physik* **1908**, *330*, 377.

[3] E. Hutchings Jr, In *Engineering and Science*, California Institute of Technology, Pasadena, CA, **1960**.

[4] Y. Shi, Y. Zhang, Y. Wan, Y. Yu, Y. Zhang, X. Hu, X. Xiao, H. Xu, L. Zhang, B. Pan, *Photon. Res., PRJ* **2022**, *10*, A106.

[5] J. Ortega-Arroyo, P. Kukura, *Physical Chemistry Chemical Physics* **2012**, *14*, 15625.

[6] A. C. Arsenault, D. P. Puzzo, I. Manners, G. A. Ozin, *Nature Photon* **2007**, *1*, 468.

[7] A. Tittl, A. Leitis, M. Liu, F. Yesilkoy, D.-Y. Choi, D. N. Neshev, Y. S. Kivshar, H. Altug, *Science* **2018**, *360*, 1105.

[8] J.-J. Xu, W.-C. Zhang, Y.-W. Guo, X.-Y. Chen, Y.-N. Zhang, *Drug Delivery* **2022**, *29*, 664.

[9] W. Wang, Y. Zhou, L. Yang, X. Yang, Y. Yao, Y. Meng, B. Tang, *Advanced Functional Materials* **2022**, *32*, 2204744.

[10] K. B. Beć, J. Grabska, C. W. Huck, In *Comprehensive Analytical Chemistry* (Ed.: Cozzolino, D.), Elsevier, **2022**, pp. 1–43.

[11] B. H. Stuart, *Infrared Spectroscopy: Fundamentals and Applications*, John Wiley & Sons, **2004**.

[12] D. Dregely, F. Neubrech, H. Duan, R. Vogelgesang, H. Giessen, *Nat Commun* **2013**, *4*, 2237.

[13] D. Rodrigo, A. Tittl, N. Ait-Bouziad, A. John-Herpin, O. Limaj, C. Kelly, D. Yoo, N. J. Wittenberg, S.-H. Oh, H. A. Lashuel, H. Altug, *Nat Commun* **2018**, *9*, 2160.

[14] C. Huck, F. Neubrech, J. Vogt, A. Toma, D. Gerbert, J. Katzmann, T. Härtling, A. Pucci, *ACS Nano* **2014**, *8*, 4908.

[15] F. Neubrech, C. Huck, K. Weber, A. Pucci, H. Giessen, *Chem. Rev.* **2017**, *117*, 5110.

[16] H. Hu, T. Weber, O. Bienek, A. Wester, L. Hüttenhofer, I. D. Sharp, S. A. Maier, A. Tittl, E. Cortés, *ACS Nano* **2022**, *16*, 13057.

[17] S. A. Maier, *Plasmonics: Fundamentals and Applications*, Springer US, New York, NY, **2007**.

[18] K. Koshelev, Y. Kivshar, *ACS Photonics* **2021**, *8*, 102.

[19] C.-W. Qiu, T. Zhang, G. Hu, Y. Kivshar, *Nano Lett.* **2021**, *21*, 5461.

[20] L. M. Berger, M. Barkey, S. A. Maier, A. Tittl, *Advanced Optical Materials n/a*, 2301269.

[21] J. Valentine, S. Zhang, T. Zentgraf, E. Ulin-Avila, D. A. Genov, G. Bartal, X. Zhang, *Nature* **2008**, *455*, 376.

[22] E. Cortés, F. J. Wendisch, L. Sortino, A. Mancini, S. Ezendam, S. Saris, L. de S. Menezes, A. Tittl, H. Ren, S. A. Maier, *Chem. Rev.* **2022**, *122*, 15082.

[23] W. T. Chen, A. Y. Zhu, F. Capasso, *Nat Rev Mater* **2020**, *5*, 604.

[24] F. Zangeneh-Nejad, D. L. Sounas, A. Alù, R. Fleury, *Nat Rev Mater* **2021**, *6*, 207.

[25] J. von Neuman, E. Wigner, *Physikalische Zeitschrift* **1929**, *30*, 467.

[26] F. H. Stillinger, D. R. Herrick, *Phys. Rev. A* **1975**, *11*, 446.

[27] B. Zhen, C. W. Hsu, L. Lu, A. D. Stone, M. Soljačić, *Phys. Rev. Lett.* **2014**, *113*, 257401.

[28] T. Y. Poh, N. A. B. M. Ali, M. Mac Aogáin, M. H. Kathawala, M. I. Setyawati, K. W. Ng, S. H. Chotirmall, *Particle and Fibre Toxicology* **2018**, *15*, 46.

[29] S. I. Azzam, A. V. Kildishev, *Advanced Optical Materials* **2021**, *9*, 2001469.

[30] M. V. Rybin, K. L. Koshelev, Z. F. Sadrieva, K. B. Samusev, A. A. Bogdanov, M. F. Limonov, Y. S. Kivshar, *Phys. Rev. Lett.* **2017**, *119*, 243901.

[31] M. Odit, K. Koshelev, S. Gladyshev, K. Ladutenko, Y. Kivshar, A. Bogdanov, *Advanced Materials* **2021**, *33*, 2003804.

[32] H. Xu, Y. Shi, *Laser & Photonics Reviews* **2020**, *14*, 1900430.

[33] Z. F. Sadrieva, M. A. Belyakov, M. A. Balezin, P. V. Kapitanova, E. A. Nenasheva, A. F. Sadreev, A. A. Bogdanov, *Phys. Rev. A* **2019**, *99*, 053804.

[34] J. Wang, J. Kühne, T. Karamanos, C. Rockstuhl, S. A. Maier, A. Tittl, *Advanced Functional Materials* **2021**, *31*, 2104652.

[35] L. Kühner, L. Sortino, R. Berté, J. Wang, H. Ren, S. A. Maier, Y. Kivshar, A. Tittl, *Nat Commun* **2022**, *13*, 4992.

[36] M.-S. Hwang, K.-Y. Jeong, J.-P. So, K.-H. Kim, H.-G. Park, *Commun Phys* **2022**, *5*, 1.

[37] Y. Liang, K. Koshelev, F. Zhang, H. Lin, S. Lin, J. Wu, B. Jia, Y. Kivshar, *Nano Lett.* **2020**, *20*, 6351.

[38] T. Shi, Z.-L. Deng, Q.-A. Tu, Y. Cao, X. Li, *PhotoniX* **2021**, *2*, 7.

[39] Z. Liao, Q. Ma, L. Wang, Z. Yang, M. Li, F. Deng, W. Hong, *Opt. Express, OE* **2022**, *30*, 24676.

[40] J. Liu, C. Chen, X. Li, J. Li, D. Dong, Y. Liu, Y. Fu, *Opt. Express, OE* **2023**, *31*, 4347.

[41] A. S. Kupriiannov, K. L. Domina, V. V. Khardikov, A. B. Evlyukhin, V. R. Tuz, *Opt. Lett., OL* **2020**, *45*, 1527.

[42] R. Adato, A. Artar, S. Erramilli, H. Altug, *Nano Lett.* **2013**, *13*, 2584.

[43] Y. Liang, H. Lin, S. Lin, J. Wu, W. Li, F. Meng, Y. Yang, X. Huang, B. Jia, Y. Kivshar, *Nano Lett.* **2021**, *21*, 8917.

[44] A. Aigner, A. Tittl, J. Wang, T. Weber, Y. Kivshar, S. A. Maier, H. Ren, *Science Advances* **2022**, *8*.

[45] A. Leitis, A. Tittl, M. Liu, B. H. Lee, M. B. Gu, Y. S. Kivshar, H. Altug, *Science Advances* **2019**, *5*, eaaw2871.

[46] D. R. Abujetas, Á. Barreda, F. Moreno, J. J. Sáenz, A. Litman, J.-M. Geffrin, J. A. Sánchez-Gil, *Sci Rep* **2019**, *9*, 16048.

[47] A. D. Falco, Y. Zhao, A. Alú, *Applied Physics Letters* **2011**, *99*, 163110.

[48] X. Zhang, Q. Li, F. Liu, M. Qiu, S. Sun, Q. He, L. Zhou, *Light Sci Appl* **2020**, *9*, 76.

[49] M. Qiu, M. Jia, S. Ma, S. Sun, Q. He, L. Zhou, *Phys. Rev. Appl.* **2018**, *9*, 054050.

[50] I. E. L. Stephens, K. Chan, A. Bagger, S. W. Boettcher, J. Bonin, E. Boutin, A. K. Buckley, R. Buonsanti, E. R. Cave, X. Chang, S. W. Chee, A. H. M. da Silva, P. de Luna, O. Einsle, B. Endrődi, M. Escudero-Escribano, J. V. F. de Araujo, M. C. Figueiredo, C. Hahn, K. U. Hansen, S. Haussener, S. Hunegnaw, Z. Huo, Y. J. Hwang, C. Janáky, B. S. Jayathilake, F. Jiao, Z. P. Jovanov, P. Karimi, M. T. M. Koper, K. P. Kuhl, W. H. Lee, Z. Liang, X. Liu, S. Ma, M. Ma, H.-S. Oh, M. Robert, B. R. Cuenya, J. Rossmeisl, C. Roy, M. P. Ryan, E. H. Sargent, P. Sebastián-Pascual, B. Seger, L. Steier, P. Strasser, A. S. Varela, R. E. Vos, X. Wang, B. Xu, H. Yadegari, Y. Zhou, *J. Phys. Energy* **2022**, *4*, 042003.

[51] O. S. Bushuyev, P. De Luna, C. T. Dinh, L. Tao, G. Saur, J. Van De Lagemaat, S. O. Kelley, E. H. Sargent, *Joule* **2018**, *2*, 825.

[52] C. Huck, J. Vogt, M. Sendner, D. Hengstler, F. Neubrech, A. Pucci, *ACS Photonics* **2015**, *2*, 1489.

[53] C. F. Bohren, D. R. Huffman, *Absorption and Scattering of Light by Small Particles*, John Wiley & Sons, **2008**.

[54] V. Giannini, A. I. Fernández-Domínguez, S. C. Heck, S. A. Maier, *Chem. Rev.* **2011**, *111*, 3888.

[55] L. M. Berger, M. Duportal, L. de S. Menezes, E. Cortés, S. A. Maier, A. Tittl, K. Krischer, *Advanced Functional Materials* **2023**, *33*, 2300411.

[56] D. W. Oxtoby, H. P. Gillis, L. J. Butler, *Principles of Modern Chemistry*, Cengage Learning, **2015**.

[57] S. Nitopi, E. Bertheussen, S. B. Scott, X. Liu, A. K. Engstfeld, S. Horch, B. Seger, I. E. L. Stephens, K. Chan, C. Hahn, J. K. Nørskov, T. F. Jaramillo, I. Chorkendorff, *Chem. Rev.* **2019**, *119*, 7610.

[58] F. L. McCrackin, E. Passaglia, R. R. Stromberg, H. L. Steinberg, *J Res Natl Bur Stand A Phys Chem* **1963**, *67A*, 363.

[59] A. Sommerfeld, *Z. Physik* **1928**, *47*, 1.

[60] P. Drude, *Annalen der Physik* **1900**, *306*, 566.

[61] S. J. Youn, T. H. Rho, B. I. Min, K. S. Kim, *physica status solidi (b)* **2007**, *244*, 1354.

[62] U. Fano, *Phys. Rev.* **1961**, *124*, 1866.

[63] V. Savinov, N. Papasimakis, D. P. Tsai, N. I. Zheludev, *Commun Phys* **2019**, *2*, 1.

[64] J. D. Jackson, *Classical Electrodynamics*, John Wiley & Sons, **2021**.

[65] Absorption and Scattering of Light by Small Particles, 1st ed., John Wiley & Sons, Ltd, **1998**.

[66] M. Meier, A. Wokaun, *Opt. Lett., OL* **1983**, *8*, 581.

[67] H. Kuwata, H. Tamaru, K. Esumi, K. Miyano, *Applied Physics Letters* **2003**, *83*, 4625.

[68] F. Bloch, *Z. Physik* **1929**, *52*, 555.

[69] N. W. Ashcroft, N. D. Mermin, *Solid State Physics*, Holt, Rinehart and Winston, **1976**.

[70] Lord Rayleigh, *The London, Edinburgh, and Dublin Philosophical Magazine and Journal of Science* **1907**, *14*, 60.

[71] R. W. Wood, *The London, Edinburgh, and Dublin Philosophical Magazine and Journal of Science* **1902**, *3*, 396.

[72] K. T. Carron, W. Fluhr, M. Meier, A. Wokaun, H. W. Lehmann, *J. Opt. Soc. Am. B, JOSAB* **1986**, *3*, 430.

[73] B. Auguié, W. L. Barnes, *Phys. Rev. Lett.* **2008**, *101*, 143902.

[74] R. Adato, A. A. Yanik, C.-H. Wu, G. Shvets, H. Altug, *Opt. Express* **2010**, *18*, 4526.

[75] F. J. García de Abajo, *Rev. Mod. Phys.* **2007**, *79*, 1267.

[76] F. Le, D. W. Brandl, Y. A. Urzhumov, H. Wang, J. Kundu, N. J. Halas, J. Aizpurua, P. Nordlander, *ACS Nano* **2008**, *2*, 707.

[77] G. Goubau, *Journal of Applied Physics* **2004**, *21*, 1119.

[78] K. Ladutenko, U. Pal, A. Rivera, O. Peña-Rodríguez, *Computer Physics Communications* **2017**, *214*, 225.

[79] J. v. Neumann, E. Wigner, *Phys. Z.* **1929**, *30*, 465.

[80] C. M. Linton, P. McIver, *Wave Motion* **2007**, *45*, 16.

[81] T. Lepetit, B. Kanté, *Phys. Rev. B* **2014**, *90*, 241103.

[82] D. C. Marinica, A. G. Borisov, S. V. Shabanov, *Phys. Rev. Lett.* **2008**, *100*, 183902.

[83] C. W. Hsu, B. Zhen, J. Lee, S.-L. Chua, S. G. Johnson, J. D. Joannopoulos, M. Soljačić, *Nature* **2013**, *499*, 188.

[84] C. W. Hsu, B. Zhen, A. D. Stone, J. D. Joannopoulos, M. Soljačić, *Nat Rev Mater* **2016**, *1*, 1.

[85] Z. Dong, Z. Mahfoud, R. Paniagua-Domínguez, H. Wang, A. I. Fernández-Domínguez, S. Gorelik, S. T. Ha, F. Tjiptoharsono, A. I. Kuznetsov, M. Bosman, J. K. W. Yang, *Light Sci Appl* **2022**, *11*, 20.

[86] K. L. Koshelev, Z. F. Sadrieva, A. A. Shcherbakov, Yu. S. Kivshar, A. A. Bogdanov, *Phys. Usp.* **2023**, *66*, 494.

[87] K. Koshelev, S. Lepeshov, M. Liu, A. Bogdanov, Y. Kivshar, *Phys. Rev. Lett.* **2018**, *121*, 193903.

[88] D. R. Abujetas, J. Olmos-Trigo, J. A. Sánchez-Gil, *Advanced Optical Materials* **2022**, *10*, 2200301.

[89] M. V. Rybin, K. L. Koshelev, Z. F. Sadrieva, K. B. Samusev, A. A. Bogdanov, M. F. Limonov, Y. S. Kivshar, *Phys. Rev. Lett.* **2017**, *119*, 243901.

[90] K. Koshelev, S. Kruk, E. Melik-Gaykazyan, J.-H. Choi, A. Bogdanov, H.-G. Park, Y. Kivshar, *Science* **2020**, *367*, 288.

[91] M. I. Molina, A. E. Miroshnichenko, Y. S. Kivshar, *Phys. Rev. Lett.* **2012**, *108*, 070401.

[92] N. A. Gallo, M. I. Molina, *J. Phys. A: Math. Theor.* **2014**, *48*, 045302.

[93] S. Fan, W. Suh, J. D. Joannopoulos, *J. Opt. Soc. Am. A, JOSAA* **2003**, *20*, 569.

[94] W. Suh, Z. Wang, S. Fan, *IEEE Journal of Quantum Electronics* **2004**, *40*, 1511.

[95] E. Noether, *Nachrichten von der Gesellschaft der Wissenschaften zu Göttingen, Mathematisch-Physikalische Klasse* **1918**, *1918*, 235.

[96] X. Gao, B. Zhen, M. Soljačić, H. Chen, C. W. Hsu, *ACS Photonics* **2019**, *6*, 2996.

[97] A. C. Overvig, S. C. Malek, M. J. Carter, S. Shrestha, N. Yu, *Phys. Rev. B* **2020**, *102*, 035434.

[98] L. Kühner, F. J. Wendisch, A. A. Antonov, J. Bürger, L. Hüttenhofer, L. de S. Menezes, S. A. Maier, M. V. Gorkunov, Y. Kivshar, A. Tittl, *Unlocking the out-of-plane dimension for photonic bound states in the continuum to achieve maximum optical chirality*, arXiv, **2022**.

[99] R. Berté, T. Weber, L. de Souza Menezes, L. Kühner, A. Aigner, M. Barkey, F. J. Wendisch, Y. Kivshar, A. Tittl, S. A. Maier, *Nano Lett.* **2023**, *23*, 2651.

[100] B. Xi, H. Xu, S. Xiao, L. Zhou, *Phys. Rev. B* **2011**, *83*, 165115.

[101] S. A. Khan, S. B. Khan, L. U. Khan, A. Farooq, K. Akhtar, A. M. Asiri, In *Handbook of Materials Characterization* (Ed.: Sharma, S. K.), Springer International Publishing, Cham, **2018**, pp. 317–344.

[102] X. Yang, Z. Sun, T. Low, H. Hu, X. Guo, F. J. García de Abajo, P. Avouris, Q. Dai, *Adv. Mater.* **2018**, *30*, 1704896.

[103] F. Neubrech, C. Huck, K. Weber, A. Pucci, H. Giessen, *Chem. Rev.* **2017**, *117*, 5110.

[104] J. Jiang, X. Wang, S. Li, F. Ding, N. Li, S. Meng, R. Li, J. Qi, Q. Liu, G. L. Liu, *Nanophotonics* **2018**, *7*, 1517.

[105] A. J. Bard, Ed., In *Encyclopedia of Electrochemistry: Online*, Wiley, **2007**.

[106] P. A. Christensen, A. Hamnett, In *Comprehensive Chemical Kinetics*, Elsevier, **1989**, pp. 1–77.

[107] A. J. Wain, M. A. O'Connell, *Advances in Physics: X* **2017**, *2*, 188.

[108] T. G. Habteyes, S. Dhuey, E. Wood, D. Gargas, S. Cabrini, P. J. Schuck, A. P. Alivisatos, S. R. Leone, *ACS Nano* **2012**, *6*, 5702.

[109] M. Osawa, K.-I. Ataka, K. Yoshii, Y. Nishikawa, *Appl Spectrosc* **1993**, *47*, 1497.

[110] W. Nernst, *Zeitschrift für Physikalische Chemie* **1889**, *4U*, 129.

[111] M. Faraday, *Philosophical Transactions of the Royal Society of London* **1834**, *124*, 77.

[112] A. M. Appel, J. E. Bercaw, A. B. Bocarsly, H. Dobbek, D. L. DuBois, M. Dupuis, J. G. Ferry, E. Fujita, R. Hille, P. J. A. Kenis, C. A. Kerfeld, R. H. Morris, C. H. F. Peden, A. R. Portis, S. W. Ragsdale, T. B. Rauchfuss, J. N. H. Reek, L. C. Seefeldt, R. K. Thauer, G. L. Waldrop, *Chem. Rev.* **2013**, *113*, 6621.

[113] S. Rönsch, J. Schneider, S. Matthischke, M. Schlüter, M. Götz, J. Lefebvre, P. Prabhakaran, S. Bajohr, *Fuel* **2016**, *166*, 276.

[114] J. Yang, W. Ma, D. Chen, A. Holmen, B. H. Davis, *Applied Catalysis A: General* **2014**, *470*, 250.

[115] S. G. Jadhav, P. D. Vaidya, B. M. Bhanage, J. B. Joshi, *Chemical Engineering Research and Design* **2014**, *92*, 2557.

[116] I. Chorkendorff, J. W. Niemantsverdriet, *Concepts of Modern Catalysis and Kinetics*, John Wiley & Sons, **2017**.

[117] P. Saha, S. Amanullah, A. Dey, *Acc. Chem. Res.* **2022**, *55*, 134.

[118] Y. Katayama, F. Nattino, L. Giordano, J. Hwang, R. R. Rao, O. Andreussi, N. Marzari, Y. Shao-Horn, *J. Phys. Chem. C* **2019**, *123*, 5951.

[119] J. Lim, H. Lim, B. Kim, S. M. Kim, J.-B. Lee, K. R. Cho, H. Choi, S. Sultan, W. Choi, W. Kim, Y. Kwon, *Electrochimica Acta* **2021**, *395*, 139190.

[120] X. Lu, W. Tu, Y. Zhou, Z. Zou, *Advanced Energy Materials* **2023**, *13*, 2300628.

[121] S. Zong, A. Chen, M. Wiśniewski, L. Macheli, L. L. Jewell, D. Hildebrandt, X. Liu, *Carbon Capture Science & Technology* **2023**, *8*, 100133.

[122] X. Zhi, A. Vasileff, Y. Zheng, Y. Jiao, S.-Z. Qiao, *Energy & Environmental Science* **2021**, *14*, 3912.

[123] E. R. Corson, R. Kas, R. Kostecki, J. J. Urban, W. A. Smith, B. D. McCloskey, R. Kortlever, *J. Am. Chem. Soc.* **2020**, *142*, 11750.

[124] G. Blyholder, *J. Phys. Chem.* **1964**, *68*, 2772.

[125] Y. Ikezawa, H. Saito, H. Matsubayashi, G. Toda, *Journal of Electroanalytical Chemistry and Interfacial Electrochemistry* **1988**, *252*, 395.

[126] O. C. Zienkiewicz, R. L. Taylor, J. Z. Zhu, Eds., In *The Finite Element Method: its Basis and Fundamentals (Seventh Edition)*, Butterworth-Heinemann, Oxford, **2013**.

[127] U. S. Inan, R. A. Marshall, *Numerical Electromagnetics: The FDTD Method*, Cambridge University Press, **2011**.

[128] S. Babar, J. H. Weaver, *Appl. Opt., AO* **2015**, *54*, 477.

[129] A. D. Rakić, A. B. Djurišić, J. M. Elazar, M. L. Majewski, *Appl. Opt.* **1998**, *37*, 5271.

[130] S. Franssila, L. Sainiemi, In *Encyclopedia of Microfluidics and Nanofluidics* (Ed.: Li, D.), Springer US, Boston, MA, **2008**, pp. 1772–1781.

[131] J. Faist, F. Capasso, D. L. Sivco, C. Sirtori, A. L. Hutchinson, A. Y. Cho, *Science* **1994**, *264*, 553.

[132] R. F. Kazarinov, R. A. Suris, *Sov. Phys. Semicond.* **1971**, *5*, 707.

[133] A. A. Michelson, E. W. Morley, *American Journal of Science* **1887**, *s3-34*, 333.

[134] K. Khare, M. Butola, S. Rajora, *Fourier Optics and Computational Imaging*, Springer International Publishing, Cham, **2023**.

[135] Y. Hu, J. Huo, B. Cheng, *Sensors* **2023**, *23*, 143.

[136] C. Dong, L. T. Richardson, T. Solouki, K. K. Murray, *J. Am. Soc. Mass Spectrom.* **2022**, *33*, 463.

[137] J. Kilgus, G. Langer, K. Duswald, R. Zimmerleiter, I. Zorin, T. Berer, M. Brandstetter, *Opt. Express, OE* **2018**, *26*, 30644.

[138] C. R. Burch, *Proc. Phys. Soc.* **1947**, *59*, 41.

[139] A. M. Hanninen, E. O. Potma, *APL Photonics* **2019**, *4*, 080801.

[140] T. Sannomiya, O. Scholder, K. Jefimovs, C. Hafner, A. B. Dahlin, *Small* **2011**, *7*, 1653.

[141] G. Palermo, M. Rippa, Y. Conti, A. Vestri, R. Castagna, G. Fusco, E. Suffredini, J. Zhou, J. Zyss, A. De Luca, L. Petti, *ACS Appl. Mater. Interfaces* **2021**, *13*, 43715.

[142] H. Jia, Z. Li, B. Wang, G. Xing, Y. L. Wong, H. Ren, M. Li, K.-Y. Wong, D. Lei, L.-W. Wong, J. Zhao, W. Zhang, S. Sang, A. Jian, X. Zhang, *ACS Photonics* **2022**, *9*, 652.

[143] A. P. Anthur, H. Zhang, R. Paniagua-Dominguez, D. A. Kalashnikov, S. T. Ha, T. W. W. Maß, A. I. Kuznetsov, L. Krivitsky, *Nano Lett.* **2020**, *20*, 8745.

[144] Q. Leng, H. Su, J. Liu, L. Zhou, K. Qin, Q. Wang, J. Fu, S. Wu, X. Zhang, *Nanophotonics* **2021**, *10*, 1871.

[145] P. Xie, Z. Liang, T. Jia, D. Li, Y. Chen, P. Chang, H. Zhang, W. Wang, *Phys. Rev. B* **2021**, *104*, 125446.

[146] M. Gao, Y. He, Y. Chen, T.-M. Shih, W. Yang, H. Chen, Z. Yang, Z. Wang, *Nanophotonics* **2020**, *9*, 815.

[147] H. Gao, J. M. McMahon, M. H. Lee, J. Henzie, S. K. Gray, G. C. Schatz, T. W. Odom, *Opt. Express* **2009**, *17*, 2334.

[148] A. Sayanskiy, A. S. Kupriianov, S. Xu, P. Kapitanova, V. Dmitriev, V. V. Khardikov, V. R. Tuz, *Phys. Rev. B* **2019**, *99*, 085306.

[149] A. Mackay, *Electronics Letters* **1989**, *24*, 1624.

[150] T. W. W. Maß, T. Taubner, *ACS Photonics* **2015**, *2*, 1498.

[151] J. Kühne, J. Wang, T. Weber, L. Kühner, S. A. Maier, A. Tittl, *Nanophotonics* **2021**, *10*, 4305.

[152] M. F. Lagadec, A. Grimaud, *Nat. Mater.* **2020**, *19*, 1140.

[153] I. Sullivan, A. Goryachev, I. A. Digdaya, X. Li, H. A. Atwater, D. A. Vermaas, C. Xiang, *Nat Catal* **2021**, *4*, 952.

[154] S. Zhao, R. Jin, R. Jin, *ACS Energy Lett.* **2018**, *3*, 452.

[155] A. Wuttig, M. Yaguchi, K. Motobayashi, M. Osawa, Y. Surendranath, *Proc Natl Acad Sci USA* **2016**, *113*, E4585.

[156] M. J. Hossain, M. M. Rahman, Md. Jafar Sharif, *Nanoscale Adv.* **2020**, *2*, 1245.

[157] C. D. Silva, G. Cabello, W. A. Christinelli, E. C. Pereira, A. Cuesta, *Journal of Electroanalytical Chemistry* **2017**, *800*, 25.

[158] I. J. McPherson, P. A. Ash, L. Jones, A. Varambhia, R. M. J. Jacobs, K. A. Vincent, *J. Phys. Chem. C* **2017**, *121*, 17176.

[159] A. Susarrey-Arce, R. M. Tiggelaar, J. G. E. Gardeniers, A. van Houselt, L. Lefferts, *J. Phys. Chem. C* **2015**, *119*, 24887.

[160] T. Smolinka, M. Heinen, Y. X. Chen, Z. Jusys, W. Lehnert, R. J. Behm, *Electrochimica Acta* **2005**, *50*, 5189.

[161] G. G. Hammes, *Spectroscopy for the Biological Sciences*, John Wiley & Sons, **2005**.

[162] J. A. Ribeiro, M. G. F. Sales, C. M. Pereira, *TrAC Trends in Analytical Chemistry* **2022**, *157*, 116766.

[163] S. Vijay, T. V. Hogg, J. Ehlers, H. H. Kristoffersen, Y. Katayama, Y. Shao Horn, I. Chorkendorff, K. Chan, B. Seger, *J. Phys. Chem. C* **2021**, *125*, 17684.

[164] M. Dunwell, Q. Lu, J. M. Heyes, J. Rosen, J. G. Chen, Y. Yan, F. Jiao, B. Xu, *J. Am. Chem. Soc.* **2017**, *139*, 3774.

[165] D. Wang, F. Shi, J. Jose, Y. Hu, C. Zhang, A. Zhu, R. Grzeschik, S. Schlücker, W. Xie, *J. Am. Chem. Soc.* **2022**, *144*, 5003.

[166] S. A. Hosseini Farahabadi, M. Entezami, H. Abouali, H. Amarloo, M. Poudineh, S. Safavi-Naeini, *Sci Rep* **2022**, *12*, 17747.

[167] T. Li, D. Shang, S. Gao, B. Wang, H. Kong, G. Yang, W. Shu, P. Xu, G. Wei, *Biosensors* **2022**, *12*, 314.

[168] J. Wang, S. A. Maier, A. Tittl, *Advanced Optical Materials* **2022**, *10*, 2102366.

[169] N. Li, Y. Lu, S. Li, Q. Zhang, J. Wu, J. Jiang, G. L. Liu, Q. Liu, *Biosensors and Bioelectronics* **2017**, *93*, 241.

[170] K. Nakamoto, R. Kurita, O. Niwa, *Anal. Chem.* **2012**, *84*, 3187.

[171] X. Wang, S.-C. Huang, S. Hu, S. Yan, B. Ren, *Nat Rev Phys* **2020**, *2*, 253.

[172] D. Wright, Q. Lin, D. Berta, T. Földes, A. Wagner, J. Griffiths, C. Readman, E. Rosta, E. Reisner, J. J. Baumberg, *Nat Catal* **2021**, *4*, 157.

[173] Y. Fang, H. Wang, H. Yu, X. Liu, W. Wang, H.-Y. Chen, N. J. Tao, *Acc. Chem. Res.* **2016**, *49*, 2614.

[174] X. R. Cheng, G. Q. Wallace, F. Lagugné-Labarthet, K. Kerman, *ACS Appl. Mater. Interfaces* **2015**, *7*, 4081.

[175] S.-S. Wang, X.-P. Zhao, F.-F. Liu, M. R. Younis, X.-H. Xia, C. Wang, *Anal. Chem.* **2019**, *91*, 4413.

[176] A. Stefancu, L. Nan, L. Zhu, V. Chiș, I. Bald, M. Liu, N. Leopold, S. A. Maier, E. Cortes, *Advanced Optical Materials* **2022**, *10*, 2200397.

[177] I. Villegas, M. J. Weaver, *The Journal of Chemical Physics* **1994**, *101*, 1648.

[178] S. Watanabe, J. Inukai, M. Ito, *Surface Science* **1993**, *293*, 1.

[179] M. Nakamura, H. Ogasawara, J. Inukai, M. Ito, *Surface Science* **1993**, *283*, 248.

[180] Y. Katayama, L. Giordano, R. R. Rao, J. Hwang, H. Muroyama, T. Matsui, K. Eguchi, Y. Shao-Horn, *J. Phys. Chem. C* **2018**, *122*, 12341.

[181] L. Novotny, B. Hecht, *Principles of Nano-Optics*, Cambridge University Press, **2012**.

[182] A. H. Harvey, S. G. Kaplan, J. H. Burnett, *Int J Thermophys* **2005**, *26*, 1495.

[183] I. Hickman, *Analog Electronics: Analog Circuitry Explained*, Newnes, **2013**.

[184] J. Lan, J. Hutter, M. Iannuzzi, *J. Phys. Chem. C* **2018**, *122*, 24068.

[185] M. J. S. Farias, C. Busó-Rogero, A. A. Tanaka, E. Herrero, J. M. Feliu, *Langmuir* **2020**, *36*, 704.

[186] B. Luk'yanchuk, N. I. Zheludev, S. A. Maier, N. J. Halas, P. Nordlander, H. Giessen, C. T. Chong, *Nature Mater* **2010**, *9*, 707.

[187] S. Fan, *Appl. Phys. Lett.* **2002**, *80*, 908.

[188] R. H. A. Ras, R. A. Schoonheydt, C. T. Johnston, *J. Phys. Chem. A* **2007**, *111*, 8787.

[189] A. Cuesta, A. Couto, A. Rincón, M. C. Pérez, A. López-Cudero, C. Gutiérrez, *Journal of Electroanalytical Chemistry* **2006**, *586*, 184.

[190] A. López-Cudero, A. Cuesta, C. Gutiérrez, *Journal of Electroanalytical Chemistry* **2005**, *579*, 1.

[191] S.-G. Sun, Z.-Y. Zhou, *Phys. Chem. Chem. Phys.* **2001**, *3*, 3277.

[192] A. Rodes, E. Pastor, T. Iwasita, *Journal of Electroanalytical Chemistry* **1994**, *377*, 215.

[193] A. López-Cudero, Á. Cuesta, C. Gutiérrez, *Journal of Electroanalytical Chemistry* **2006**, *586*, 204.

[194] S.-C. Chang, M. J. Weaver, *Surface Science* **1990**, *230*, 222.

[195] B. B. Blizanac, C. A. Lucas, M. E. Gallagher, M. Arenz, P. N. Ross, N. M. Marković, *J. Phys. Chem. B* **2004**, *108*, 625.

[196] N. Mayet, K. Servat, K. B. Kokoh, T. W. Napporn, *Electrocatalysis* **2021**, *12*, 26.

[197] J. S. Spendelow, J. D. Goodpaster, P. J. A. Kenis, A. Wieckowski, *J. Phys. Chem. B* **2006**, *110*, 9545.

[198] A. S. Varela, C. Schlaup, Z. P. Jovanov, P. Malacrida, S. Horch, I. E. L. Stephens, I. Chorkendorff, *J. Phys. Chem. C* **2013**, *117*, 20500.

[199] G. Samjeské, K. Komatsu, M. Osawa, *J. Phys. Chem. C* **2009**, *113*, 10222.

[200] Y. Katayama, L. Giordano, R. R. Rao, J. Hwang, H. Muroyama, T. Matsui, K. Eguchi, Y. Shao-Horn, *J. Phys. Chem. C* **2018**, *122*, 12341.

[201] V. Stamenkovic, K. C. Chou, G. A. Somorjai, P. N. Ross, N. M. Markovic, *J. Phys. Chem. B* **2005**, *109*, 678.

[202] M. Dunwell, J. Wang, Y. Yan, B. Xu, *Phys. Chem. Chem. Phys.* **2017**, *19*, 971.

[203] M. Dunwell, Y. Yan, B. Xu, *ACS Catal.* **2017**, *7*, 5410.

[204] P. Deshlahra, J. Conway, E. E. Wolf, W. F. Schneider, *Langmuir* **2012**, *28*, 8408.

[205] L. Jacobse, M. J. Rost, M. T. M. Koper, *ACS Cent. Sci.* **2019**, *5*, 1920.

[206] X. Deng, F. Galli, M. T. M. Koper, *ACS Appl. Energy Mater.* **2020**, *3*, 597.

[207] B. Hammer, O. H. Nielsen, J. K. Nrskov, *Catalysis Letters* **1997**, *46*, 31.

[208] M. Duportal, L. M. Berger, S. A. Maier, A. Tittl, K. Krischer, *Multi-band metasurface-driven surface-enhanced infrared absorption spectroscopy for improved characterization of in-situ electrochemical reactions*, arXiv, **2023**.

[209] T. Iwasita, F. C. Nart, B. Lopez, W. Vielstich, *Electrochimica Acta* **1992**, *37*, 2361.

[210] A. Rodes, E. Pastor, T. Iwasita, *Journal of Electroanalytical Chemistry* **1994**, *377*, 215.

[211] M. C. Arévalo, C. Gomis-Bas, F. Hahn, B. Beden, A. Arévalo, A. J. Arvia, *Electrochimica Acta* **1994**, *39*, 793.

[212] S.-G. Sun, Z.-Y. Zhou, *Physical Chemistry Chemical Physics* **2001**, *3*, 3277.

[213] K. Kato, Y. Liu, S. Murakami, Y. Morita, T. Mori, *Nanotechnology* **2021**, *32*, 485301.

[214] M. J. S. Farias, C. Busó-Rogero, A. A. Tanaka, E. Herrero, J. M. Feliu, *Langmuir* **2020**, *36*, 704.

[215] M. Dunwell, *Phys. Chem. Chem. Phys.* **2017**, *19*.

[216] S.-C. Chang, M. J. Weaver, *Surface Science* **1990**, *230*, 222.

[217] D. K. Lambert, *Electrochimica Acta* **1996**, *41*, 623.

[218] S. Ringe, E. L. Clark, J. Resasco, A. Walton, B. Seger, A. T. Bell, K. Chan, *Energy Environ. Sci.* **2019**, *12*, 3001.

[219] H. Wang, R. G. Tobin, D. K. Lambert, *The Journal of Chemical Physics* **1994**, *101*, 4277.

[220] S. Fan, *Appl. Phys. Lett.* **2002**, *80*, 908.

[221] A. Alavi, P. Hu, T. Deutsch, P. L. Silvestrelli, J. Hutter, *Phys. Rev. Lett.* **1998**, *80*, 3650.

[222] P. Rheinländer, S. Henning, J. Herranz, H. A. Gasteiger, *ECS Trans.* **2013**, *50*, 2163.

[223] J. Giner, *Electrochimica Acta* **1963**, *8*, 857.

[224] G. A. Kamat, J. A. Zamora Zeledón, G. T. K. K. Gunasooriya, S. M. Dull, J. T. Perryman, J. K. Nørskov, M. B. Stevens, T. F. Jaramillo, *Commun Chem* **2022**, *5*, 20.

[225] S. Watanabe, J. Inukai, M. Ito, *Surface Science* **1993**, *293*, 1.

[226] W. Sheng, H. A. Gasteiger, Y. Shao-Horn, *J. Electrochem. Soc.* **2010**, *157*, B1529.

[227] Y. Taji, A. Zagalskaya, I. Evazzade, S. Watzele, K.-T. Song, S. Xue, C. Schott, B. Garlyyev, V. Alexandrov, E. Gubanova, A. S. Bandarenka, *Nano Materials Science* **2022**.

[228] J. K. Nørskov, T. Bligaard, A. Logadottir, J. R. Kitchin, J. G. Chen, S. Pandelov, U. Stimming, *Journal of The Electrochemical Society* **2005**, *152*, J23.

[229] H. A. Haus, *Waves and Fields in Optoelectronics*, Prentice-Hall, **1984**.

[230] J. Wang, T. Weber, A. Aigner, S. A. Maier, A. Tittl, *Laser & Photonics Reviews* **2023**, *n/a*, 2300294.

Acknowledgements

First, I want to express my gratitude to the supervisor of my dissertation, Prof. Dr. Stefan Maier. Working under his tutelage was invaluable and genuinely enriching. I deeply appreciate the trust and support he placed in my research, along with the many opportunities he offered me. An opportunity I particularly enjoyed was attending the Meta conference in Paris in July 2023. Moreover, his experience in structuring his group and building and setting up laboratories provided me with state-of-the-art nanofabrication and testing equipment and allowed me the ease of focusing on my research.

Next, I want to thank the second referee of my dissertation, Prof. Dr. Joachim Rädler, and the other participants of my doctoral committee, Prof. Dr. Jan von Delft, PD Dr. Theobald Lohmüller, Prof. Dr. Jochen Weller, and Prof. Dr. Ralf Jungmann.

Furthermore, I want to express immense gratitude for the invaluable help, guidance, and mentorship offered by Dr. Andreas Tittl. The weekly discussions with him helped me develop my projects, assess ideas, and place the next steps. His critical and useful feedback made me a better and more efficient person and I will carry his advice with me. Moreover, I am grateful for his initiative in making life in the group more exciting, with weekly after-work meetings and fun discussions during lunchtime.

I want to thank the members of the Hynano group Alex, Alwin, Andrea, Andreas, Anil, Chenhao, Christoph, Connor, Dmytro, Ermanno, Fedja, Haiyang, Ibrahim, Jonas, Juan, Julian, Lin, Luca, Lucca, Ludwig, Luis, Markus, Matias, Michael, Merve, Paul, Rui, Seryio, Simone, Thomas P. & W., Thorsten, and Wenzheng for the great time! For the strong administrative work, I want to thank Denise Wedemeyer, Martina Edenhofer, Reinhold Rath, and Namvar Jahanmehr, who kept the institute running smoothly.

Finally, I would like to extend my heartfelt gratitude to my friends and family for their unwavering support throughout my challenging journey toward earning my Ph.D. I profoundly thank my parents, Brigitta and Ingolf, my sister, Sarah, and my grandparents, Rosa and Christian, for their immense support and the occasional distractions that were indispensable. Then, I would like to thank Harry for being himself and being consistently available for extensive discussions. Without their presence, this achievement would not have been possible. Finally, I want to give a special acknowledgment to my incredible girlfriend, Kailey, who stood by my side and whose support gave me immense strength and perseverance.